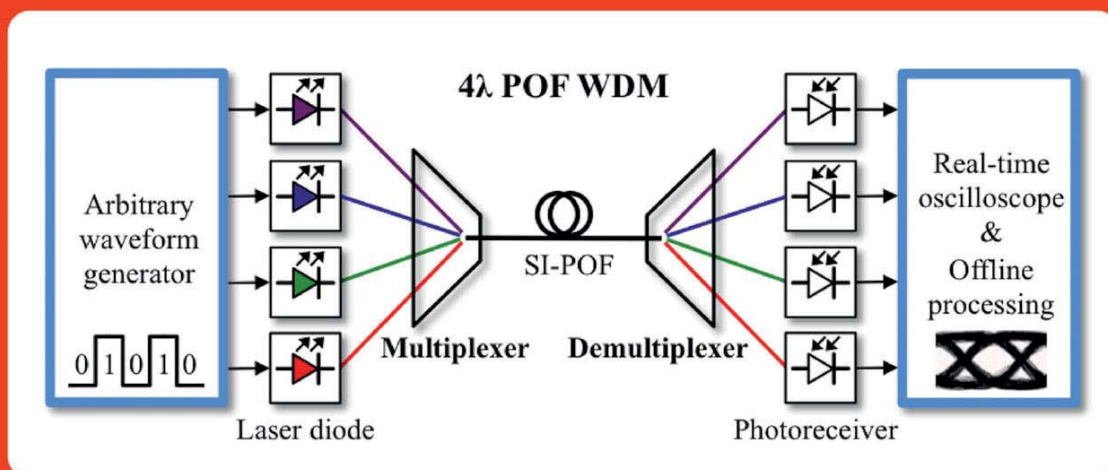


U.H.P. Fischer-Hirchert (Hrsg.)

Wavelength Division Multiplexing for Short-Range Communication Over 1 mm Step-Index Polymer Optical Fiber



Mladen Jončić





Wavelength Division Multiplexing for Short-Range Communication Over 1 mm Step-Index Polymer Optical Fiber





Wavelength Division Multiplexing for Short-Range Communication Over 1 mm Step-Index Polymer Optical Fiber

Von der Fakultät für Elektrotechnik, Informationstechnik, Physik
der Technischen Universität Carolo-Wilhelmina zu Braunschweig

zur Erlangung des Grades eines Doktors
der Ingenieurwissenschaften (Dr.-Ing.)

genehmigte
Dissertation

von
Dipl.-Ing. Mladen Jončić
aus Niš

Eingereicht am: 12.10.2015

Mündliche Prüfung am: 12.01.2016

1. Referent: Prof. Dr.-Ing. habil. Wolfgang Kowalsky

2. Referent: Prof. Dr. rer. nat. et Ing. habil. Ulrich Fischer-Hirchert

2016



Bibliografische Information der Deutschen Nationalbibliothek

Die Deutsche Nationalbibliothek verzeichnet diese Publikation in der Deutschen Nationalbibliografie; detaillierte bibliografische Daten sind im Internet über <http://dnb.d-nb.de> abrufbar.

1. Aufl. - Göttingen: Cuvillier, 2016

Zugl.: Dissertation an der Technischen Universität Braunschweig,
Fakultät für Elektrotechnik, Informationstechnik, Physik

© CUVILLIER VERLAG, Göttingen 2016

Nonnenstieg 8, 37075 Göttingen

Telefon: 0551-54724-0

Telefax: 0551-54724-21

www.cuvillier.de

Alle Rechte vorbehalten. Ohne ausdrückliche Genehmigung des Verlages ist es nicht gestattet, das Buch oder Teile daraus auf fotomechanischem Weg (Fotokopie, Mikrokopie) zu vervielfältigen.

1. Auflage, 2016

Gedruckt auf umweltfreundlichem, säurefreiem Papier aus nachhaltiger Forstwirtschaft.

ISBN 978-3-7369-9204-7

eISBN 978-3-7369-8204-8



To my wife Jordana



Acknowledgements

This Ph.D. thesis was realized as a collaborative project between the Institut für Hochfrequenztechnik (IHF) der Technischen Universität Braunschweig and the Photonic Communications Lab of the Harz University of Applied Sciences. The thesis is based on my research activities carried out at the Photonic Communications Lab during my time as a research assistant (Nov. 2010 – Feb. 2014), and thereafter as a holder of a scholarship from the Saxony-Anhalt Graduate Funding Program (Graduiertenförderung des Landes Sachsen-Anhalt) (since Mar. 2014).

First and foremost, I would like to express my deepest gratitude to my supervisors Prof. Dr. habil. Wolfgang Kowalsky and Prof. Dr. habil. Ulrich Fischer-Hirschert for their invaluable guidance and constant support throughout my project. I am especially thankful to Prof. Dr. habil. Ulrich Fischer-Hirschert for getting me interested in the optical communications, involving me to work with the polymer fibers and for believing in me. I also express my sincerest appreciation to my assistant supervisor Dr.-Ing. Reinhard Caspary for his commitment, invaluable comments and fruitful discussions that greatly helped me improve this work.

I owe many thanks to my colleagues Dr.-Ing. Matthias Haupt, Sebastian Höll and André Zufelde from the project VIP HOPE of the German Federal Ministry of Education and Research (BMBF) for their constructive cooperation. I am particularly indebted to Dr.-Ing. Matthias Haupt for the numerous technical discussions and for always being very supportive. I also thank him for providing the simulation results for a concave diffraction grating-based demultiplexer. I would further like to express my profound thanks to Dr.-Ing. Roman Kruglov from the Polymer Optical Fiber Application Center (POF-AC). The measurements with the DMT modulation would not have been possible without his expertise in digital signal processing. I extend my gratitude to Jens-Uwe Just for his practical assistance in the technical matters when the help was needed in the lab. My acknowledgement is also on behalf of Olaf Flechtner and his team from the mechanical workshop of the IHF for the production of mechanical components for my project. Furthermore, I am grateful to Julia Stallmann, Holger Strutz, Sabrina Hoppstock and Peter Kußmann from the Photonic Communications Lab, and to Christian Reinboth and Hans-Martin Schulze from the HarzOptics GmbH for supporting me in a number of ways. I would also like to take the opportunity to sincerely thank the administrative staff of both universities for their support, in particular Thomas Lohr. To all the others who helped me overcome diverse challenges during my project, I hereby express my thanks and appreciation.



A very warm thank you to the families Skauradschun and Lontzek from Wernigerode for being so kind and friendly to me, and for generously helping me during the first months in Germany.

For their wholehearted support and encouragement throughout the years a huge thank you to my parents Božana and Rajko Jončić, brother Stevan, parents-in-law Suzana and Miroslav Spasić, sister-in-law Miroslava, and many relatives and friends back in Serbia.

Words cannot express how grateful I am to my beloved wife Jordana for her unconditional support and continuous encouragement that gave me the strength and motivation throughout this journey. Her love and belief in me were in the end what made this dissertation possible.

Goslar, August 2015

Mladen Jončić

Abstract

In short-range communication 1 mm PMMA SI-POF established itself as a reasonable alternative to the traditional data communication media such as glass fibers, copper cables and wireless systems. Due to multiple advantages such as a large core diameter, tolerance to fiber facet damages and low installation costs, the SI-POF is typically used for network systems in homes, vehicles and industrial automation.

The commercial systems with SI-POF use a single channel for data transmission. However, the data carrying capacity of SI-POF is impaired by strong inter-modal dispersion and high optical attenuation. Over the last few years various concepts to overcome the bandwidth limitation of SI-POF have been successfully demonstrated, including optimization of the optoelectronic components and implementation of the digital signal processing techniques. Complying with any of the hitherto developments, utilization of several optical carriers for parallel transmission of data channels over a single fiber, known as WDM, represents another alternative to increase the capacity of SI-POF link.

This thesis investigates the application of WDM in short-range optical communication over SI-POF. The focus of research is on:

- Demultiplexing techniques for SI-POF;
- High-speed WDM transmission over SI-POF;
- Channel allocation for POF WDM systems.

For WDM an optical demultiplexer is a key component. The thesis concentrates on the demultiplexing techniques employing thin-film interference filters and a concave diffraction grating.

An interference filter-based SI-POF demultiplexer was realized using a precisely adjustable opto-mechanical setup, which allowed maximization of the optical throughput in the individual channels. Intermediate setups with two and three channels were first established. In addition, a serial and a two-stage configuration of a target setup with four channels were realized. It was shown that the latter configuration outperformed the former one in terms of IL and IL uniformity. Furthermore, the demultiplexer with two-stage configuration provided low IL (< 5.7 dB) and high channel isolation (> 30 dB). It outperformed other interference filter-based SI-POF demultiplexers reported so far, and was well suited for implementation in high-speed POF WDM transmission experiments.

Within the BMBF project VIP HOPE a demultiplexer with a ruled concave diffraction grating was produced. It is the first demultiplexer with a concave grating ever reported for SI-POF. Since the demultiplexer became available in the late project phase, its demultiplexing



properties could not be examined during the project duration. In the thesis a subsequent theoretical and experimental analysis of the demultiplexer was carried out. Two methods for characterization of transmission properties of the demultiplexer were proposed and investigated. A diffraction angle-dependent spectral response over a broad wavelength range and a diffraction angle-dependent transmittance at five lasing wavelengths were measured by scanning the curved focal surface of the demultiplexer with an output SI-POF. The results confirmed the wavelength separating function of the demultiplexer. However, a poor grating quality due to unstable parameters of the ruling process led to high IL (> 20 dB) and low channel isolation (< 15 dB). That prevented the use of the demultiplexer for POF WDM transmission experiments.

To demonstrate experimentally the feasibility and potential of a high-speed POF WDM concept, a four-channel data transmission setup was realized. A four-legged multiplexing POF bundle was developed to combine the signals from four visible laser diodes onto SI-POF link. For the separation of wavelength channels the interference filter-based demultiplexer with two-stage configuration was used. It was shown that POF WDM with lower channel rates and simple transmission technique (NRZ+FFE) could provide aggregate bit rates comparable to those achieved with the single-wavelength systems that used more advanced transmission techniques (DMT or NRZ/PAM+DFE) but required more signal processing. In addition, the record 14.77 Gb/s and 8.26 Gb/s data rates employing the offline-processed DMT modulation were demonstrated over 50 m and 100 m SI-POF, respectively, at the $\text{BER}=10^{-3}$. Compared to the fastest single-wavelength systems, two times higher transmission capacities were achieved.

Finally, the channel allocation for today's and future POF WDM systems was investigated. It was shown that the extension of ITU-T G.694.2 *Coarse* WDM grid into the visible spectrum, with 15 channels and 20 nm channel spacing, is best suited to support WDM applications over SI-POF.



Table of contents

1	Introduction	1
2	Fundamentals of WDM for short-range communication over POF	7
2.1	Transmission properties of 1 mm PMMA SI-POF	7
2.2	Demultiplexing for 1 mm PMMA SI-POF	9
2.2.1	Demultiplexing employing thin-film interference filters	10
2.2.2	Demultiplexing based on a concave diffraction grating.....	12
2.3	POF coupling losses	17
2.4	Data transmission techniques for increasing the channel capacity	20
2.4.1	Non-return-to-zero modulation and feed-forward equalization	20
2.4.2	Discrete multitone modulation	22
2.5	Spectral channels for POF WDM.....	23
2.5.1	WDM standardization by ITU-T.....	24
3	POF demultiplexer employing thin-film interference filters.....	29
3.1	Basic concept of a demultiplexer employing thin-film interference filters	29
3.2	Experimental setup	31
3.3	Measurement results for a two-channel demultiplexer	33
3.4	Operating principle and measurement results for a three-channel demultiplexer.....	35
3.5	Operating principle and measurement results for a four-channel demultiplexer	36
3.6	Discussion	40
4	POF demultiplexer based on a concave diffraction grating	43
4.1	Theoretical calculations on the designed grating	43
4.2	Theoretical considerations on the designed demultiplexer	45
4.2.1	Detection in the second diffraction order	46
4.2.2	Detection in the third diffraction order	48
4.3	Description of demultiplexer samples.....	49
4.4	Measurement methods.....	52
4.4.1	Simplified measurement method.....	52
4.4.2	Initially developed measurement method	55



4.5	Experimental setup and measurement results	63
4.6	Discussion	72
4.6.1	Discussion on wavelength separating performances.....	72
4.6.2	Discussion on transmission performances	75
4.6.3	Recommendations	78
5	Four-channel POF WDM transmission experiments	79
5.1	WDM transmission employing NRZ modulation	80
5.1.1	Experimental setup.....	81
5.1.2	Measurement results and discussion	82
5.2	WDM transmission employing NRZ modulation and FFE equalization	85
5.2.1	Experimental setup.....	85
5.2.2	Measurement results and discussion	88
5.3	WDM transmission employing DMT modulation	92
5.3.1	Experimental setup.....	92
5.3.2	Measurement results and discussion	94
5.4	Discussion	101
6	Spectral grids in the visible spectrum for POF WDM applications	103
6.1	Requirements for spectral grid in the visible spectrum.....	103
6.1.1	Channel distribution with respect to the spectral attenuation of SI-POF	103
6.1.2	Performances of different demultiplexing techniques	104
6.1.3	Availability of laser diodes in the visible spectrum	105
6.2	Establishing and evaluating grids in the visible spectrum	106
6.2.1	Extension of ITU-T G.694.1 DWDM grid into the visible spectrum	106
6.2.2	Extension of ITU-T G.694.2 CWDM grid into the visible spectrum	107
6.2.3	Newly defined frequency and wavelength grids	109
6.3	Discussion	114
7	Summary and outlook.....	115
	References	121
	List of abbreviations.....	129
	List of publications.....	131

1 Introduction

Having its origin in the 1960's as well as the silica glass fiber, the polymer optical fiber (POF) stayed long in the shadow of the huge development and success of glass fiber communications. However, the advances in POF technology and the growing need for high-speed short-range communication networks make POF nowadays gain more and more in importance. The key advantage of POF is a large core diameter. It makes POF tolerant to the fiber facet damages and relaxes the alignment tolerances, thus also reducing the installation costs. Furthermore, POF is pliable, durable, and inexpensive, offers small weight and short bend radius, allows easy installation, simple termination and quick troubleshooting, and also provides the immunity to electromagnetic interference. Due to its diverse advantages, in short-range applications POF established itself as a reasonable alternative to the traditional data communication media such as glass fibers, copper cables and wireless systems (see Table 1.1).

Table 1.1: Comparison of different transmission media. Characteristics between very bad (--) and particularly good (++) [Fischer11].

Transmission medium	Data rate	Distance	Safety	Cost	Handling	Installation	Total
Twisted pair cable	+	0	0	++	-	0	2+
Coaxial cable	0	0	0	+	0	0	1+
Glass fiber	++	++	++	--	--	-	1+
Polymer fiber	0	-	++	+	+	+	4+
Wireless	--	-	--	++	++	++	1+
Powerline	-	-	--	+	+	++	0

Today, POF is produced with different core materials, core diameters and index profiles. A comprehensive overview on various POFs is given in [Ziemann08]. Two major POF types are made of polymethyl methacrylate (PMMA) and perfluorinated (PF) materials. The parameters of the common PMMA and PF POFs are specified in the IEC Standard 60793-2-40, which defines eight different POF classes [IEC09].

The PMMA POF is produced with both step-index (SI) and graded-index (GI) profile, whereas the PF POF offers only GI profile. The GI profile of the core ensures high modal bandwidth exceeding $1.5 \text{ GHz} \times 100 \text{ m}$ for the PMMA POF and $300 \text{ MHz} \times 1 \text{ km}$ for the PF POF. However, the implementation of the PMMA GI-POF is confined to 500-680 nm wavelength range due to the high optical attenuation at other wavelengths ($> 400 \text{ dB/km}$). The



PF GI-POF is best suited for use in the infrared region, e.g. in the first (850 nm) and the second (1300 nm) optical window, where of-the-shelf components developed for multimode glass fibers are available. In contrast, the PMMA SI-POF suffers from intermodal dispersion limiting the bandwidth-length product to around $50 \text{ MHz} \times 100 \text{ m}$ (see subchapter 2.1), but also provides several attenuation windows in the visible spectrum (400-700 nm). Due to its advantages over the other POF types such as technological maturity, ease and cost of production and high numerical aperture (NA), the standard 1 mm PMMA SI-POF (POF class A4a.2 according to IEC 60793-2-40) is the best known and by far the most widely employed type of POF. This is also the fiber the thesis concentrates on. Throughout the work the terms SI-POF and POF will be equally used to address this fiber type.

Three major application sectors of SI-POF data communication technology are industrial automation, automotive industry and in-house/office networks. Over more than 25 years SI-POF has been employed in industrial automation applications. The bus systems such as Profibus (1.5 Mb/s, 60 m) and INTERBUS (2 Mb/s, 70 m), and industrial Fast Ethernet (100 Mb/s, 50 m) are the typical application scenarios.

In vehicles SI-POF displaces copper in the network structure of a passenger cabin for multimedia data services. The infotainment communication system known as Media Oriented System Transport (MOST) connects different multimedia components in the SI-POF-based ring topology [Grzempa08], as illustrated in Fig. 1.1. First introduced in the BMW 7 Series 2001, the MOST technology is nowadays used by almost all major car manufacturers in the world. In 2011 there were more than 50 different car types on the market employing SI-POF (BMW, Mercedes-Benz, Ford, Hyundai, etc.) [Bunge12]. The current (third) version of the MOST system (MOST150) supports the data transfer at 150 Mb/s over link lengths of about

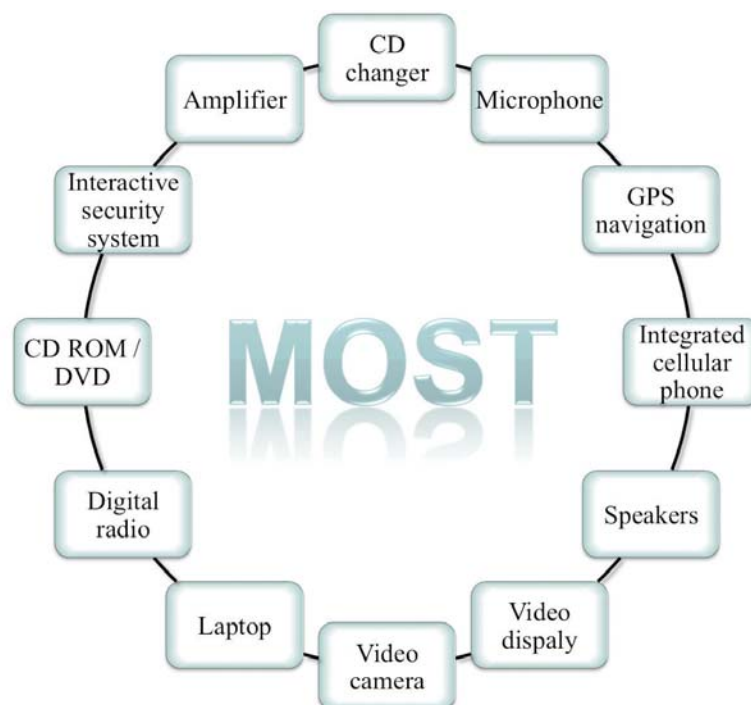


Fig. 1.1: SI-POF-based ring topology of a MOST system in a car.

10 m. Not only multimedia, but also security-critical and safety applications benefit from SI-POF (e.g. Byteflight bus system, 10 Mb/s).

Another sector where SI-POF displaces traditional communication media are short-range networks in houses and offices. As an in-house extension of a broadband access network (e.g. VDSL, HFC, FTTB), the typical application of POF technology is the delivery of triple-play services (combination of broadcasting, telecommunication and internet) to the end user, as illustrated in Fig. 1.2. The Fast Ethernet transceivers (100 Mb/s) and since 2013 also the Gigabit Ethernet transceivers (1 Gb/s) are available on the market enabling the transmission of broadband services over 50 m SI-POF. The Gigabit solutions from KD-POF employing the multilevel signaling and from Teleconnect based on the multicarrier modulation are accompanied by the technical standards ETSI TS 105 175-1-2 [ETSI15] and ITU-T G.9960, Annex F [ITU11], respectively.

The commercial communication systems with SI-POF use a single channel for data transmission. However, the transmission performances of SI-POF are impaired by strong inter-modal dispersion and high optical attenuation. Stimulated by the growing bandwidth demands (e.g. 10 Gb/s to 40 Gb/s to 100 Gb/s Ethernet speed), various concepts to overcome the low-pass characteristic of SI-POF have been successfully demonstrated over the last few years. The simplest solutions utilized passive equalization implemented as an analog high-pass filter that increased the electrical -3 dB bandwidth of a channel [Vinogradov08]. A similar approach but with an adaptive analogue equalizer was presented in [Sundermeyer09]. Other solutions concentrated on the development and optimization of the fast transceiver components including a red vertical-cavity surface-emitting laser [Johnson12], a large-area photodetector [Loquai14], or even a fully integrated photoreceiver with adjustable equalizer [Atef12]. A major focus was also placed on the digital signal processing techniques, which were mostly implemented offline due to the lack of commercial components. Both the non-

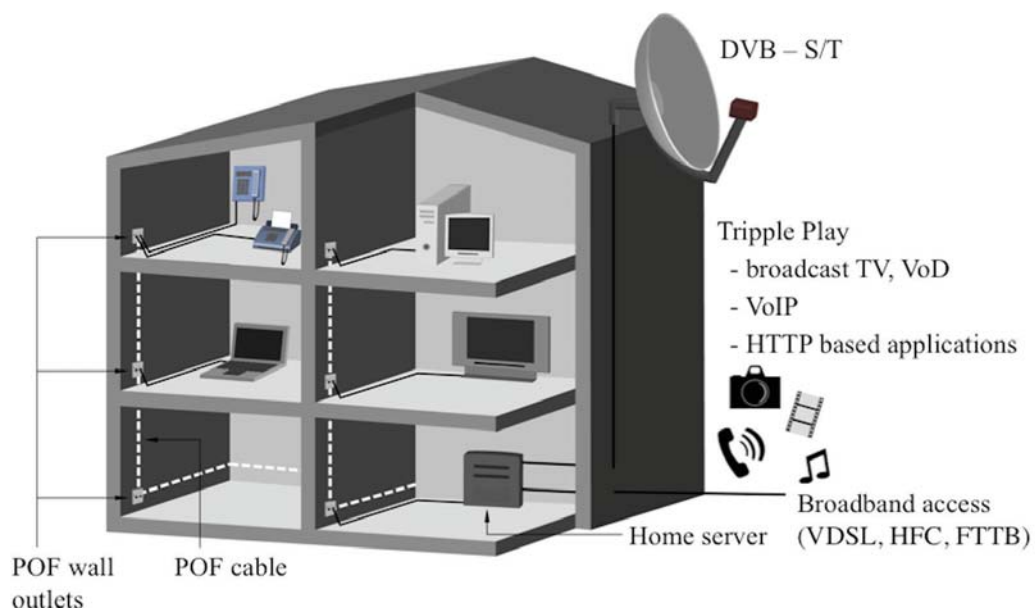


Fig. 1.2: In-house communication scenario with Ethernet over POF.

return-to-zero (NRZ) and the spectrally efficient multilevel signaling were combined with the digital receiver equalization to increase the data rates over SI-POF [Loquai13], [Breyer10]. The sophisticated spectrally efficient multicarrier modulation formats were also successfully implemented to combat the highly dispersive SI-POF channel [Lee09a], [Vinogradov11]. A record capacity of approx. 6.3 Gb/s was achieved over 50 m SI-POF at the bit error rate (BER) of 10^{-3} employing the offline-processed discrete multitone (DMT) modulation and a commercial 650 nm laser diode [Vinogradov11]. In the same publication, a record capacity of approx. 4.2 Gb/s was demonstrated over 100 m SI-POF at the BER= 10^{-3} , allowing for error-free transmission after implementing forward-error correction (FEC). An early prototype of OSRAM 515 nm laser diode was thereby employed to transmit NRZ signal, which was equalized at the receiver using the offline implementation of a decision-feedback equalizer (DFE).

Complying with any of the hitherto developments, utilization of several optical carriers for parallel transmission of data channels over a single fiber represents another alternative to increase the transmission capacity of SI-POF. The technique is well known as wavelength division multiplexing (WDM). In glass fiber communications WDM has been firmly established for more than two decades and represents the key technology in modern high-capacity optical networks with the distances ranging from several thousand down to ~ 10 km [Mukherjee06], [Kartalopoulos02], [Thiele07]. The principle of WDM is shown in Fig. 1.3. Since different wavelengths λ_1 – λ_N do not interfere with each other in a linear medium, they can be used to simultaneously carry the data signals over a single fiber. Thereby, the capacity of a fiber i.e. of an optical communication system increases almost proportionally with the number of wavelength channels.

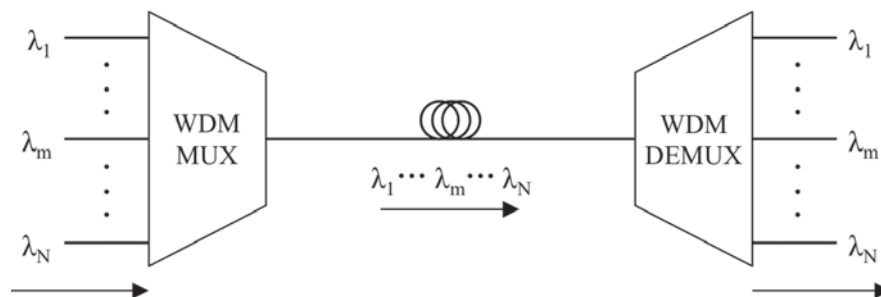


Fig. 1.3: Principle of WDM: MUX – multiplexer; DEMUX – demultiplexer.

Two components are essential for WDM, a wavelength multiplexer and demultiplexer. The multiplexer combines the signals at different wavelengths, coming from different transmitters, onto a single fiber. On the opposite side of the optical link the demultiplexer performs an inverse function, separating the wavelength channels to be detected by separate receivers. Because of e.g. interchannel crosstalk, the demultiplexer is more often considered in fiber optics. Therefore, this thesis concentrates on the demultiplexing function without loss of generality for the multiplexing operation.

The existing WDM components developed for single-mode glass fibers in the infrared region, such as Mach-Zehnder interferometers, arrayed waveguide gratings or fiber Bragg gratings, cannot be reused for a highly multimode SI-POF. On the other hand, the operating principles of demultiplexers based on thin-film interference filters and on a diffraction grating can be applied for POF. In spite of some other demultiplexing solutions (e.g. employing dispersion prisms), these two demultiplexing techniques have been recognized as the most promising for SI-POF. However, because of the difference in the operating wavelength range, fiber diameter, NA, etc. compared to the glass fibers, such demultiplexers must be newly designed for SI-POF communication. The subchapters 2.2.1 and 2.2.2 give an overview of the state of the art thin-film interference filter- and diffraction grating-based SI-POF demultiplexers respectively. The first aim of this thesis is to further investigate experimentally these two demultiplexing techniques for SI-POF.

The most frequently mentioned motivation for POF WDM is to increase the transmission capacity of SI-POF link compared to the single-wavelength systems. So far, only a few attempts have been made to investigate that possibility, primarily because of the lack of functional low-loss multiplexing and demultiplexing components. In the early attempts, the light emitting diode (LED)-based POF systems exploiting WDM technology could not provide sufficient capacity [Junger02], [Appelt02], [Bartkiv03]. Only recently, supported by the advance in the visible laser diode technology, the record-breaking POF WDM transmission experiments, including the work of the author, were performed [Kruglov12a], [Kruglov14], [Jončić14b], [Jončić14c]. Accordingly, the second aim of this thesis is to demonstrate experimentally high-speed POF WDM data transmission offering capacity increase compared to the single-channel systems. The third aim of the thesis is to investigate possible channel allocation for today's and future POF WDM systems.

The rest of the thesis is organized in the following manner. Chapter 2 gives the fundamentals of WDM for short-range communication over SI-POF that are used throughout the thesis. The next two chapters consider two different demultiplexing techniques. Chapter 3 focuses on the experimental realization of SI-POF demultiplexer employing thin-film interference filters. In a step-by-step approach, intermediate solutions with two and three channels are first established. In addition, two different configurations of a target demultiplexer setup with four channels are realized and mutually compared. Chapter 4 addresses a theoretical and experimental analysis of the previously produced SI-POF demultiplexer based on a concave diffraction grating. Two methods for characterization of transmission properties of the demultiplexer are proposed and investigated. The measurement results are interpreted in relation to the theoretical calculations and optical simulations, and are used to qualify the manufacturing process. Chapter 5 presents four-channel POF WDM transmission experiments using the demultiplexer introduced in chapter 3 to separate the wavelength channels. Several optimization steps with intermediate results are shown before a target experimental setup and data transmission results are presented, demonstrating the feasibility and potential of a high-speed POF WDM concept. Chapter 6 investigates spectral grids for the visible spectrum WDM applications over SI-POF. Criteria for evaluating the applicability of a grid for the



intended application are defined prior to establishing and analyzing different WDM channel allocations. Finally, chapter 7 summarizes the contributions of this work and outlines the possibilities for the follow-up research.

2 Fundamentals of WDM for short-range communication over POF

This chapter introduces the fundamentals of POF WDM relevant for this thesis. First, the transmission characteristics of SI-POF are considered in terms of optical attenuation and electrical bandwidth. Next, the demultiplexing techniques based on thin-film interference filters and a concave diffraction grating are described. Two data transmission techniques for increasing the channel capacity are then discussed. Finally, an overview of the existing WDM-related standards for glass fiber communication is given.

2.1 Transmission properties of 1 mm PMMA SI-POF

The 1 mm PMMA SI-POF is the best known and by far the most widely employed type of POF. It is made of 980 μm diameter PMMA core surrounded by a thin cladding (10 μm) made of fluorinated polymer. The typical spectral attenuation of SI-POF is shown in Fig. 2.1. The fiber supports operation in the visible spectrum from 400 nm to 700 nm. The lower wavelength bound is determined by the degradation of the PMMA compound with prolonged exposure to the ultraviolet (UV) wavelengths [Lekishvili02]. The attenuation value of around 400-450 dB/km, that still allows operation over shorter link lengths (< 20 m), sets the upper wavelength bound.

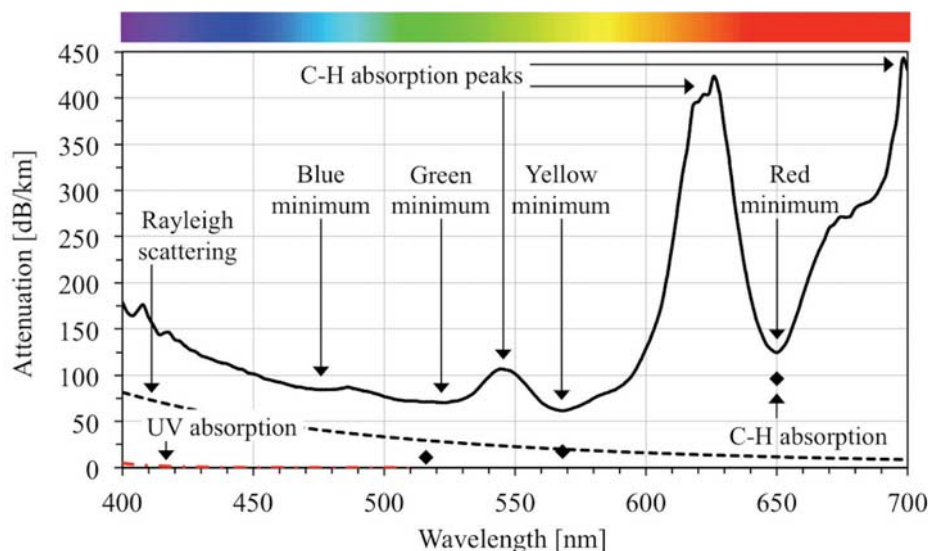


Fig. 2.1: Typical spectral attenuation of 1 mm PMMA SI-POF [Bunge11] with contributions of intrinsic loss mechanisms and with attenuation minima and maxima.

Two intrinsic loss mechanisms contribute to the raise of attenuation at shorter and particularly UV wavelengths. The electronic transitions due to the absorption of light in the polymer compound cause absorption peaks in the UV region. However, their absorption tails extend through the visible spectrum affecting the POF attenuation [Zubia01]. The dependence of the attenuation coefficient of electronic transitions α_e [dB/km] on the wavelength for PMMA is given by [Koike14]:

$$\alpha_e = 1.58 \cdot 10^{-12} \exp\left(\frac{1.15 \cdot 10^4}{\lambda}\right). \quad (2.1)$$

The second loss mechanism is the Rayleigh scattering. It is caused by the structural irregularities in the polymer compound that are much smaller than the wavelength of light (order of one tenth of wavelength or less). The effect of scattering becomes more pronounced as the wavelength decreases since the scattering attenuation coefficient α_s [dB/km] is inversely proportional to the fourth power of the wavelength [Kaino97]:

$$\alpha_s = 13 \cdot \left(\frac{633}{\lambda}\right)^4. \quad (2.2)$$

In the infrared region the attenuation significantly increases due to the intrinsic absorption losses caused by vibrations of the molecular C-H bonds (total of eight per MMA monomer). The higher overtones of the C-H bond vibrations also extend in the visible spectrum. The 7th overtone at 549 nm, and particularly the 6th and the 5th overtone at 627 nm and 736 nm respectively, cause pronounced absorption peaks and wide absorption bands, predominantly determining the level of attenuation in the red spectral range [Emslie88], [Groh88].

The contributions of the intrinsic loss mechanisms to the overall attenuation of SI-POF are also shown in Fig. 2.1. The attenuation contributions due to the vibrations of C-H bonds at 516 nm, 568 nm and 650 nm are taken from [Kaino97]. The sum of individual intrinsic loss mechanisms corresponds to the theoretical loss limit and equals approx. 40 dB/km, 37 dB/km and 107 dB/km at the respective wavelengths. In practice is this limit never achieved due to the extrinsic loss processes (absorption due to impurities in the fiber core, scattering loss due to waveguide structural imperfections, etc.) [Zubia01].

The wavelength regions where the fiber exhibits low attenuation are called attenuation windows. The SI-POF has four attenuation windows. Those are blue, green, yellow and red windows, with the absolute attenuation minimum of approx. 62 dB/km at around 568 nm (yellow window). The parameters of the attenuation windows are listed in Table 2.1.

Table 2.1: Attenuation windows of SI-POF (based on the attenuation curve from Fig. 2.1).

Attenuation window	blue	green	yellow	red
Attenuation minimum [dB/km]	85	70	62	125
Wavelength of the attenuation minimum [nm]	476	522	568	650
Approximate 3 dB width of the window [nm]	19	24	8	4

The mean refractive index of SI-POF core material in the visible spectrum is $n_{core}=1.492$, whereas the refractive index of cladding is $n_{clad}=1.412$. Due to the big difference in refractive indices of core and cladding, the numerical aperture (NA)

$$NA = \sqrt{n_{core}^2 - n_{clad}^2} \quad (2.3)$$

has the value of 0.482 (usually rounded to 0.5). The corresponding maximum acceptance angle of the fiber is 30° . The large core radius $a_{core}=490 \mu\text{m}$ combined with the high NA results in the normalized frequency V

$$V = 2\pi \frac{a_{core}}{\lambda} \cdot NA \quad (2.4)$$

of 2698 at 550 nm, which is far above the limit $V=2.405$ below which a fiber is single-moded. The number of modes N_{mod} propagating through SI-POF can be approximated as

$$N_{mod} \approx V^2/2, \quad (2.5)$$

corresponding to 3.64 million modes at 550 nm. Due to the significant path difference between lower and higher order modes, propagating respectively at smaller and larger angles relative to the optical axis, the strong intermodal dispersion is inherent to SI-POF. In the time domain it is manifested as pulse broadening, thus introducing the inter-symbol interference (ISI). In the frequency domain the intermodal dispersion results in a low pass frequency response, constraining the bandwidth-length product of SI-POF to around $50 \text{ MHz} \times 100 \text{ m}$ [Ziemann08].

2.2 Demultiplexing for 1 mm PMMA SI-POF

The WDM is one possibility to increase the data carrying capacity of SI-POF. The key component for WDM is a wavelength demultiplexer. Different approaches for realization of the demultiplexer for SI-POF have been investigated, including demultiplexing based on a dispersion prism, thin-film interference filters, and a diffraction grating (plane or concave).

The prism-based two-channel demultiplexer operating with LEDs at 530 nm and 650 nm was reported in [Zhang05]. The insertion loss (IL) and the crosstalk were around 17-20 dB and -20 dB respectively. Another solution employing the dispersion prism was shown in [Lutz05]. The three-channel demultiplexer operated with LEDs at 470 nm, 520 nm and 650 nm. It provided the IL of 12-20 dB, whereas the crosstalk took values between -4.6 dB and -34.8 dB. High IL and considerable crosstalk were caused by unoptimized optical components, broad LED spectra and high alignment sensitivity of both setups.

The two other demultiplexing techniques have been recognized as the most promising for SI-POF and have been the most investigated so far. This thesis focuses on the demultiplexers employing interference filters and a diffraction grating, in particular the concave one.

2.2.1 Demultiplexing employing thin-film interference filters

The technology based on thin-film interference filters is mature and one of the most commonly applied technologies for realization of WDM demultiplexers in single-mode glass fiber communication. The demultiplexers for *Coarse* WDM applications cascade the interference filters to provide up to 16 flat-top channels between 1271 and 1611 nm, with 20 nm minimum channel spacing [Thiele07]. The typical parameters of commercial 4-, 8-, and 16-channel demultiplexers with IL less than 1.6 dB, 2.7 dB and 3.7 dB respectively, can be found in [Lightel15]. The thin-film filter-based demultiplexers for *Dense* WDM applications are commercially available with up to 40 channels in 1550 nm region and less than 8 dB IL. Instead of simply cascading the filters, those devices usually employ a modular configuration described in [Dutta03]. The same reference provides a typical transfer function of the 40-channel demultiplexer with 3-6 dB IL and 100 GHz (0.8 nm) channel spacing.

In the visible spectrum, and thus within the application range of SI-POF, a vast variety of thin-film interference filters is available from various manufacturers. Even though not particularly intended for POF applications, the visible interference filters represent an attractive solution for POF demultiplexers, where wavelength selectivity, low IL and high isolation are required.

An interference filter, typically designed for 0° angle of incidence (AOI), utilizes the principle of constructive and destructive interference to selectively transmit certain wavelengths and reject (diminish in intensity and reflect) the others [Macleod10]. Its basic structure comprises multiple thin dielectric layers with alternating high and low refractive indices, which are successively deposited on a single glass substrate. The desired spectral response is obtained by a careful selection of the number of dielectric layers, their thickness and refractive indices. The filter is typically characterized with high passband transmittance ($> 90\%$), steep transition slopes (> 3 dB/nm) and deep blocking (> 30 dB) in rejection bands (see Fig. 2.3).

A dichroic mirror is a special type of interference filter intended for the spatial separation or combination of light at different wavelengths. It is designed to operate at 45° AOI, such that a certain spectral range is transmitted, whereas the rejected wavelength range is reflected at 90° angle with respect to the incident optical axis. A commercial visible spectrum dichroic mirror has a transition slope between the transmission and reflection band of typically 30-40 nm (see Fig. 2.3 and Table 3.1). This is significantly less steep compared to the standard interference filters designed for the normal incidence. Unlike an interference filter, e.g. a longpass mirror must be not only highly transmissive above the cutoff wavelength, but also highly reflective below it. Therefore, producing steeper slopes would require increased complexity of the coating, and accordingly, a significant rise in production costs.

The interference filters show significant angular dependence of their transmission characteristic [Herbert06]. To be applicable for SI-POF, the highly divergent beam from the fiber must be transformed into a bundle of parallel rays prior to the incidence. The principle of separation of two collimated wavelength channels using a dichroic mirror is shown in Fig. 2.2. To increase the channel isolation, an additional bandpass filtering in each of the

output channels should be implemented prior to the focusing of light. As an example, a selection of the dichroic mirror and interference filters for demultiplexing two wavelength channels centered around $\lambda_1=450$ nm and $\lambda_2=525$ nm is shown in Fig. 2.3.

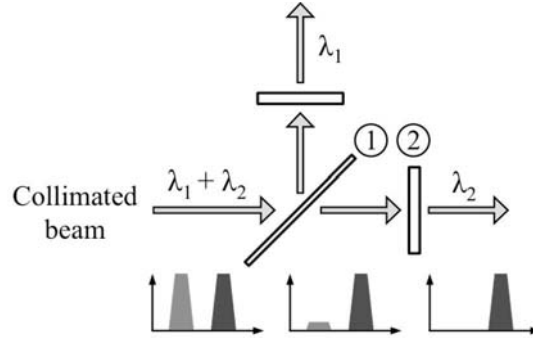


Fig. 2.2: Principle of separation of two collimated wavelength channels employing thin-film interference filters: 1 – dichroic mirror (45° AOI); 2 – interference filter (0° AOI).

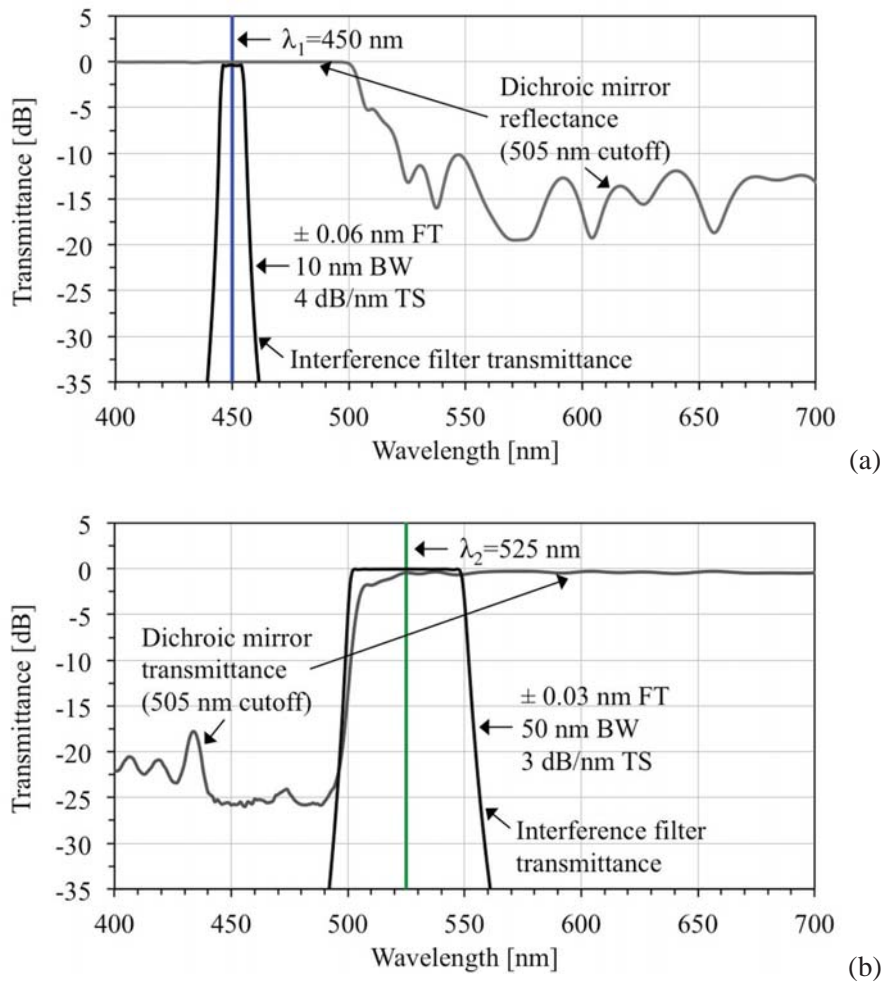


Fig. 2.3: Selection of the dichroic mirror and interference filters for demultiplexing two wavelength channels centered around (a) $\lambda_1=450$ nm and (b) $\lambda_2=525$ nm (the curves obtained from datasheets of the commercially available filters from Table 3.1 and Table 3.2): FT – flat top; BW – 3 dB passband bandwidth; TS – transition slope.

There were several attempts to realize an SI-POF demultiplexer with interference filters. The three-channel demultiplexer for the blue, green and red wavelength regions, shown in [Bartkiv03], offered the IL of 7-10 dB. Another three-channel solution with wide channel passbands in the violet, green and red spectral regions was reported in [Kruglov12]. The device provided the IL of 6-7 dB and high channel isolation. By far the best three-channel demultiplexer was reported in [Junger02]. It had wide (> 50 nm) channel passbands in the violet/blue, green and red spectral regions, the IL as low as 2.5 dB (at 570 nm), and high isolation between the channels (> 30 dB). At 450 nm, 520 nm and around 650 nm (lasing wavelengths used for SI-POF communication and in this thesis) the IL was 5 dB, 3 dB and 3 dB respectively. The demultiplexer offered small dimensions by employing a plastic housing with slits for lenses and dichroic mirrors. Furthermore, it allowed easy connection of the input and the output fibers to the housing.

In the patent [Tschekalinskij10], the same authors as in [Junger02] proposed the design of a four-channel demultiplexer by cascading the dichroic mirrors. To the best of author's knowledge, no information about practical realization of the setup has ever been published. The only four-channel demultiplexer reported so far was shown in [Appelt02]. It was based on a two-stage configuration and operated with LEDs at 470 nm, 520 nm, 590 nm and 650 nm. The IL of the setup was estimated to be 4-5 dB, but no transfer function was provided by the author. Since no additional filtering was implemented in the output ports, the demultiplexer experienced very high crosstalk. Therefore, it could not be used as a stand-alone component, but rather in combination with an electronic crosstalk compensation.

When properly designed, an interference filter-based demultiplexer is capable of providing low IL and high isolation. That makes it suitable for realizing and investigating POF WDM communication systems. In the thesis this demultiplexing approach for SI-POF is further investigated. The goal is to increase the channel count compared to [Bartkiv03], [Kruglov12a] and [Junger02], and realize a four-channel demultiplexer with improved performances compared to [Appelt02].

2.2.2 Demultiplexing based on a concave diffraction grating

Like the interference filters, the commercial plane reflective diffraction gratings can also be effectively used for realization of a demultiplexer for SI-POF. Besides the grating, an additional collimating/focusing lens is required, thus reducing the number of optical components to two. The three-channel demultiplexer based on a plane diffraction grating was shown in [Pinzon13]. The setup was optimized for 405 nm, 532 nm and 655 nm, having the IL of 3.6-5.8 dB and good channel isolation (> 20 dB). In [Pinzon14] the same authors reported the improved three-channel demultiplexer for 405 nm, 515 nm and 650 nm with the IL of 4.5 dB, 3.5 dB and 4.1 dB respectively, and isolation better than 30 dB. The SI-POF demultiplexer with the highest channel count ever reported was shown in [Kruglov14]. A plane grating was used to separate six wavelength channels with the IL of 7.5-10 dB and high isolation between the channels.

Besides the components performing the separation of different wavelengths, the dispersion prism-, interference filter- and plane diffraction grating-based demultiplexers require additional optical components for collimation and focusing of light. This not only introduces additional attenuation and aberrations caused by the lenses employed, but also leads to a complex and bulky design requiring precise alignment between the components.

In contrast, a demultiplexer based on a concave diffraction grating reduces the number of optical interfaces between its input and outputs due to the capability of the concave grating to combine the imaging and the wavelength-separating function. The concavity of the mirror is responsible for reflection and focusing of light, whereas the grating stamped on the mirror spatially disperses the incident spectrum into its monochromatic components. A principle sketch of the POF demultiplexer employing a concave diffraction grating is shown in Fig. 2.4. The Rowland circle is a circle tangent to the grating center with the radius r equal to one-half of the grating surface radius R . When the end face of the input fiber is located on the Rowland circle, the fiber images will also be focused on the Rowland circle [Palmer05], [Bartkiv05], [Haupt10]. This is where the output fibers or a detector array should be located.

The concave grating-based SI-POF demultiplexer, including the optimization of grating parameters, was theoretically investigated for both ruled [Haupt10] and holographic [Bartkiv05], [Bartkiv10] gratings. In [Ziemann11] the theoretical loss limit of a demultiplexer with an optimized concave grating was estimated to be below 3 dB, thus demonstrating its potential to provide both low IL and increased channel count compared to the previously discussed demultiplexing techniques.

Within the BMBF project VIP HOPE (“Research and Development of Key Components for High-Speed Communication via Polymer Optical Fibers”, Nov. 2010 – Feb. 2014) the optimization of the parameters of the POF demultiplexer employing a concave diffraction

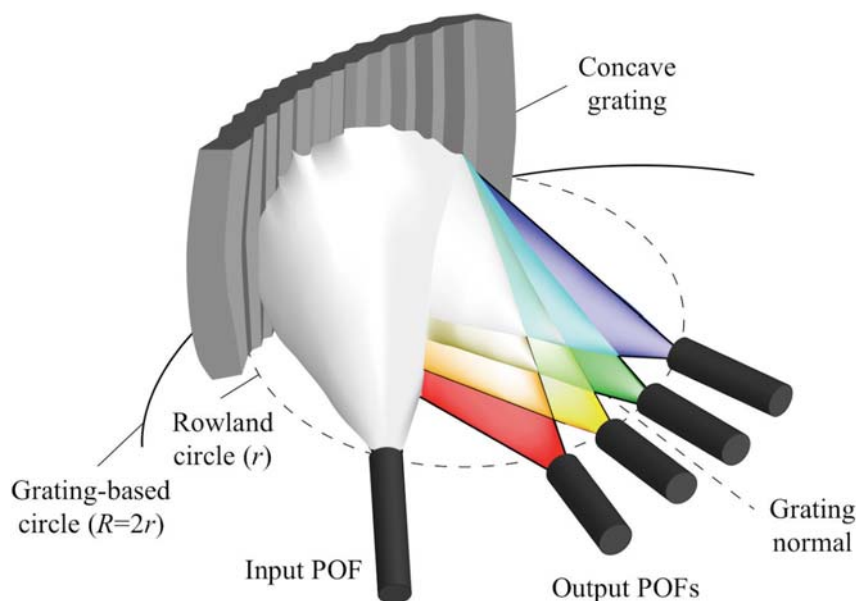


Fig. 2.4: Principle of operation of the POF demultiplexer based on a concave diffraction grating [Höll13].

grating was performed by means of an optical simulation software, and four demultiplexer samples were produced [HOPE14a]. These are the first concave grating-based demultiplexers ever reported for SI-POF. Since the samples became available in the late project phase, their demultiplexing properties were not properly examined during the project duration [Höll14]. In this thesis a subsequent theoretical and experimental analysis of this demultiplexer is carried out.

The basic concept of the VIP HOPE project demultiplexer with a ruled concave grating is introduced in Fig. 2.5. A design where the light guided by the input fiber does not change the medium and keeps propagating through PMMA prior and after the diffraction was implemented. As a consequence, the light leaving the input fiber was confined to a tighter cone ($NA=0.34$) compared to the transition from PMMA to air ($NA=0.5$). That enabled better focusing of light propagating in higher order modes.

To comply with the requirement for cost-effectiveness of POF components and to enable easy mass-production, the injection molding was targeted as a production technology [Höll13]. However, to verify the validity of the optical simulations and the functionality of the demultiplexer, all four samples were machined as a preform with a smooth concave surface on the back of the demultiplexer body. The sawtooth grooves were subsequently mechanically ruled on a PMMA substrate with a diamond tool mounted on a ruling engine. The machining of the samples and the ruling of the gratings were performed by a specialized company. To form a highly reflective surface, a thin aluminium coating was deposited onto the grating through a vacuum metalizing process.

The concave gratings are typically formed on spherical substrates which allow easy production. In contrast, toroidal substrates require a more demanding manufacturing process, but help to correct the astigmatism, which is a dominant type of aberration in the demultiplexing system from Fig. 2.4 [Palmer05]. To reduce the astigmatism, and thus improve the coupling efficiency into the output fibers, the PMMA blanks were of toroidal

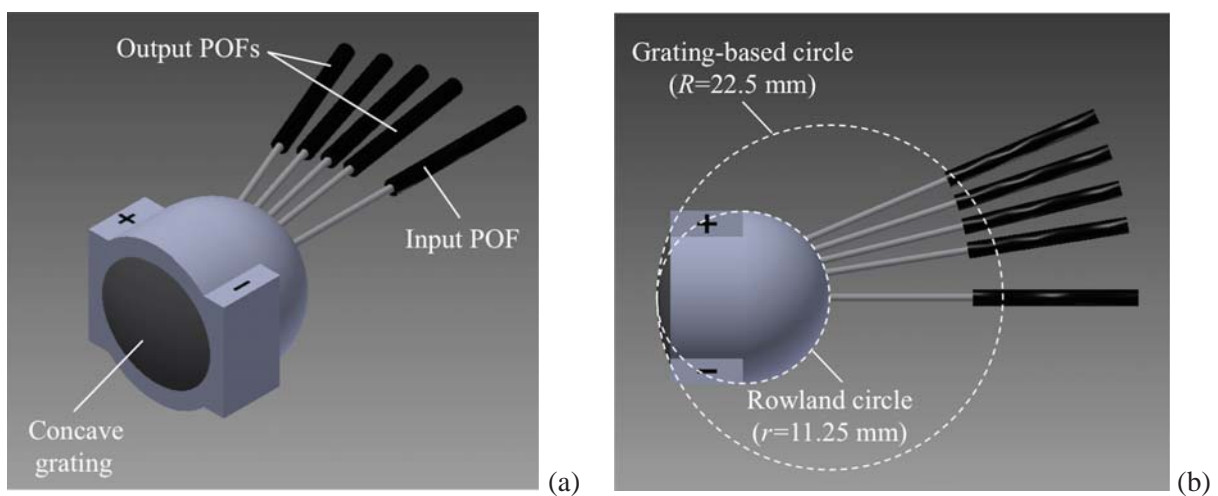


Fig. 2.5: Basic concept of the VIP HOPE project demultiplexer with a concave grating ruled on a PMMA substrate: (a) back view revealing the concave grating; (b) top view with indicated Rowland and grating-based circle.

shape. Toroidal substrates are defined by two radii. In the dispersion (also called meridional or horizontal) plane this is the tangential radius. It corresponds to the diameter of the Rowland circle and equals 22.5 mm for this particular grating. The sagittal radius refers to the radius of curvature in the vertical (sagittal) plane. By setting the sagittal radius to 20.3 mm, the astigmatism was minimized for a certain wavelength in the green wavelength region. From this it followed that the amount of astigmatism for the boundary wavelengths of the intended operating wavelength range (400-700 nm) was approximately equal (see Fig. 4.4). To minimize the coma, the angle of incidence with respect to the grating normal was set to 0° [Haupt12].

In order to meet the complex requirements of the manufacturing process, the groove density was reduced from initially planned 800 grooves/mm to an acceptable value of 400 grooves/mm, corresponding to 2.5 µm spacing between the adjacent grooves. Due to small separation between the wavelengths on the focal curve caused by lower groove density, the first diffraction order was not suitable for detection. That implied that a higher diffraction order (e.g. second or third) had to be utilized. It was estimated that the second order offered enough separation between four preselected lasing wavelengths (405 nm, 450 nm, 520 nm and a red wavelength around 650 nm) [HOPE14a].

To guide most of the optical energy in the higher diffraction order, a blazed grating had to be employed. Such a grating is capable of maximizing the grating efficiency for a given diffraction order, with the efficiency reaching its absolute maximum at a certain wavelength called the blaze wavelength. In order to achieve the best efficiency over the whole operating wavelength range from 400 nm to 700 nm, the grating was designed to blaze at 507.22 nm in the second diffraction order. The value of the corresponding blaze angle was 11.97°. The optimization of all demultiplexer parameters was performed with a ray tracing simulation software. The physical parameters of the grating ruled on a toroidal PMMA substrate are summarized in Table 2.2.

Table 2.2: Parameters of the optimized diffraction grating ruled on a toroidal PMMA substrate.

Tangential radius [mm]	22.5
Sagittal radius [mm]	20.3
Angle of incidence [°]	0
Groove density [grooves/mm]	400
Groove spacing [µm]	2.5
Second order blaze wavelength [nm]	507.22
Blaze angle [°]	11.97

The basic grating equation that applies for both plane and concave gratings is of a form [Overbeck56]:

$$d(\sin \theta_i + \sin \theta_m) = m\lambda, \quad (2.6)$$



where d is the groove spacing, θ_i is the angle between the incident light and the normal to the grating surface, θ_m is the angle between the diffracted light and the normal to the grating surface, m is the order of diffraction, and λ is the wavelength of light in the medium surrounding the grating, typically air. The diffraction by a blazed reflection grating is illustrated in Fig. 2.6, where θ_b denotes the blaze angle.

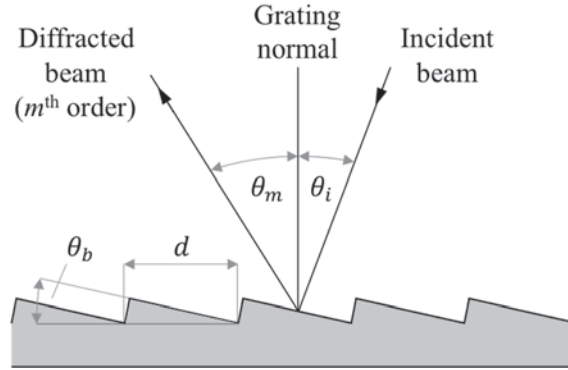


Fig. 2.6: Diffraction by a blazed reflection grating.

Because of the large diameter of the output fibers, for the POF demultiplexer with a grating surrounded by air it would be sufficient to consider the vacuum wavelengths in Equation 2.6, without performing any wavelength conversion [Bartkiv10]. However, when the light enters SI-POF, its wavelength changes according to:

$$\lambda_{PMMA} = \frac{\lambda}{n_{PMMA}(\lambda)}, \quad (2.7)$$

where λ_{PMMA} is the wavelength of light in PMMA having the wavelength dependent index of refraction $n_{PMMA}(\lambda)$, and λ is the wavelength of light in vacuum.

In the developed demultiplexing system the light guided by the input fiber does not change the medium and keeps propagating through PMMA prior and after the diffraction. To point out that the light incident on the grating has significantly shorter wavelength than in the vacuum (or air), the grating equation can be written in the following form:

$$d(\sin \theta_i + \sin \theta_m) = m \frac{\lambda}{n_{PMMA}(\lambda)}. \quad (2.8)$$

For a grating with a groove spacing d it is essential to know at which angles $\theta_m(\lambda)$ are the wavelengths of the polychromatic light incident at an angle θ_i diffracted in a given diffraction order m . Rewriting the grating equation in a convenient form yields:

$$\theta_m(\lambda) = \arcsin \left(\frac{m}{d} \frac{\lambda}{n_{PMMA}(\lambda)} - \sin \theta_i \right). \quad (2.9)$$

The parameter defining how wide is the wavelength interval in a given diffraction order which does not overlap with the adjacent orders is called the free spectral range $\Delta\lambda_m$. If λ_1 is

the shortest and λ_2 the longest wavelength in this wavelength interval, and $n_{1\text{ PMMA}}$ and $n_{2\text{ PMMA}}$ are the corresponding refractive indices, from the definition follows:

$$m \frac{\lambda_2}{n_{2\text{ PMMA}}} = (m + 1) \frac{\lambda_1}{n_{1\text{ PMMA}}} , \quad (2.10)$$

with $\Delta\lambda_m = \lambda_2 - \lambda_1$.

A measure of how much the diffraction angle changes per unit change of wavelength in a given order is called the angular dispersion \mathcal{D} . It is typically expressed in rad/nm or °/nm. For a constant angle of incidence, the angular dispersion can be obtained by differentiating the grating equation (Equation 2.6) with respect to the wavelength:

$$\mathcal{D} = \frac{\partial\theta_m}{\partial\lambda} = \frac{m}{d \cos\theta_m} = \frac{mG}{\cos\theta_m} , \quad (2.11)$$

where G is the groove density, and θ_m is obtained from Equation 2.9.

The linear dispersion \mathcal{L} of a grating system, typically expressed in mm/nm, is defined as the product of the angular dispersion \mathcal{D} and the effective focal length $f'(\theta_m)$ of the optical system. Having that the focal curve in the dispersion plane coincides with the Rowland circle, the effective focal length of the grating system from Fig. 2.4 equals $f'(\theta_m) = 2r \cos\theta_m$, where r is the radius of the Rowland circle. Now, the expression for linear dispersion can be written as:

$$\mathcal{L} = f'(\theta_m) \frac{\partial\theta_m}{\partial\lambda} = 2r \cos\theta_m \frac{mG}{\cos\theta_m n_{\text{PMMA}}(\lambda)} = \frac{2rmG}{n_{\text{PMMA}}(\lambda)} . \quad (2.12)$$

The reciprocal linear dispersion \mathcal{P} , expressed in nm/mm, is the quantity that was used in this thesis. It is defined as a reciprocal of the linear dispersion, and represents a measure of change in wavelength (in nm) per unit change of location (in mm) on the focal curve.

2.3 POF coupling losses

When analyzing the IL of a demultiplexer, a coupling loss between the input i.e. the image of the input POF and the output POF plays an important role. In the thesis this loss is analyzed as a direct coupling loss of a fiber-to-fiber connection. Both the intrinsic and the extrinsic loss mechanisms contribute to an overall connection loss. The former one is caused by differences between the connecting fibers. These refer to the fiber geometry mismatch (difference in core diameter, in core-cladding concentricity, etc.), difference in NA, and refractive index profile mismatch. It should be noted that the losses occur only if the launching fiber has a larger core diameter, higher NA or larger profile parameter respectively, than the receiving fiber. For SI-POF used as both the input and the output fiber the influence of those mismatches can be neglected.

Another source of the intrinsic coupling loss is the Fresnel reflection at the fiber-air interface. Considering two transition interfaces (launching fiber-air and air-receiving fiber), the loss due to the Fresnel reflection L_{Fres} can be expressed as:

$$L_{Fres} = -10 \log(1 - R_c)^2, \quad (2.13)$$

where R_c is the reflection coefficient of the fiber-air interface. Having that the reflection coefficient for large incidence angles is approximately equal to that of normal incidence [Werzinger13], it holds that:

$$R_c \approx \left(\frac{n_{PMMA} - 1}{n_{PMMA} + 1} \right)^2. \quad (2.14)$$

Taking $n_{PMMA}=1.492$ as the mean refractive index of PMMA within the visible spectrum, the resulting Fresnel loss at two interfaces is 0.35 dB. An abrupt change in refractive index can be reduced by employing an index matching gel or adhesive.

The extrinsic coupling loss can be caused by poor fiber end face preparation and by misalignment between the fibers. The misalignment can be:

- Lateral (axes of two fibers are parallel with an offset between them);
- Longitudinal (axes of two fibers overlap but their end faces are separated);
- Angular (axes of two fibers are not parallel).

In the following, the coupling loss between two identical multimode step-index fibers due to misalignments is considered. Thereby, a uniform mode distribution in the launching fiber is assumed. The loss due to lateral misalignment L_{Lat} is proportional to a common area of the fiber end faces and can be expressed as [Keiser00]:

$$L_{Lat} = -10 \log \frac{2}{\pi} \left(\arccos l - l\sqrt{1 - l^2} \right), \quad (2.15)$$

with l being of a form

$$l = \frac{d}{2a_{core}}, \quad (2.16)$$

where d represents the lateral misalignment. According to [Ziemann08], the theoretical coupling loss due to longitudinal misalignment L_{Long} is:

$$L_{Long} = 10 \log \left(1 + \frac{s}{2a_{core}} \sin \theta_{max} \right), \quad (2.17)$$

where s is the longitudinal separation, and θ_{max} is the maximum acceptance angle of a fiber. The coupling loss due to angular misalignment L_{Ang} can be obtained as [Opielka83]:

$$L_{Ang} = -10 \log \frac{2}{\pi} \left(\arctan \sqrt{k^2 - 1} - \sqrt{k^2 - 1}/k^2 \right), \quad (2.18)$$

with k being of a form

$$k = \frac{\sin \theta_{max}}{\sin \beta/2}, \quad (2.19)$$

where β is the angular misalignment.

Fig 2.7 gives the loss due to lateral, longitudinal and angular misalignment of two SI-POFs ($a_{core}=490 \mu\text{m}$, $\theta_{max}=30^\circ$). The horizontal axes in the graphs are limited by the maximum misalignment values considered later on in the thesis (see subchapter 4.4). As can be noticed, the POF-to-POF connection is less sensitive to longitudinal than to lateral misalignment. For example, $240 \mu\text{m}$ longitudinal and $84 \mu\text{m}$ lateral offset introduce the same coupling loss of 0.5 dB. An angular misalignment of 4.9° would also cause 0.5 dB loss.

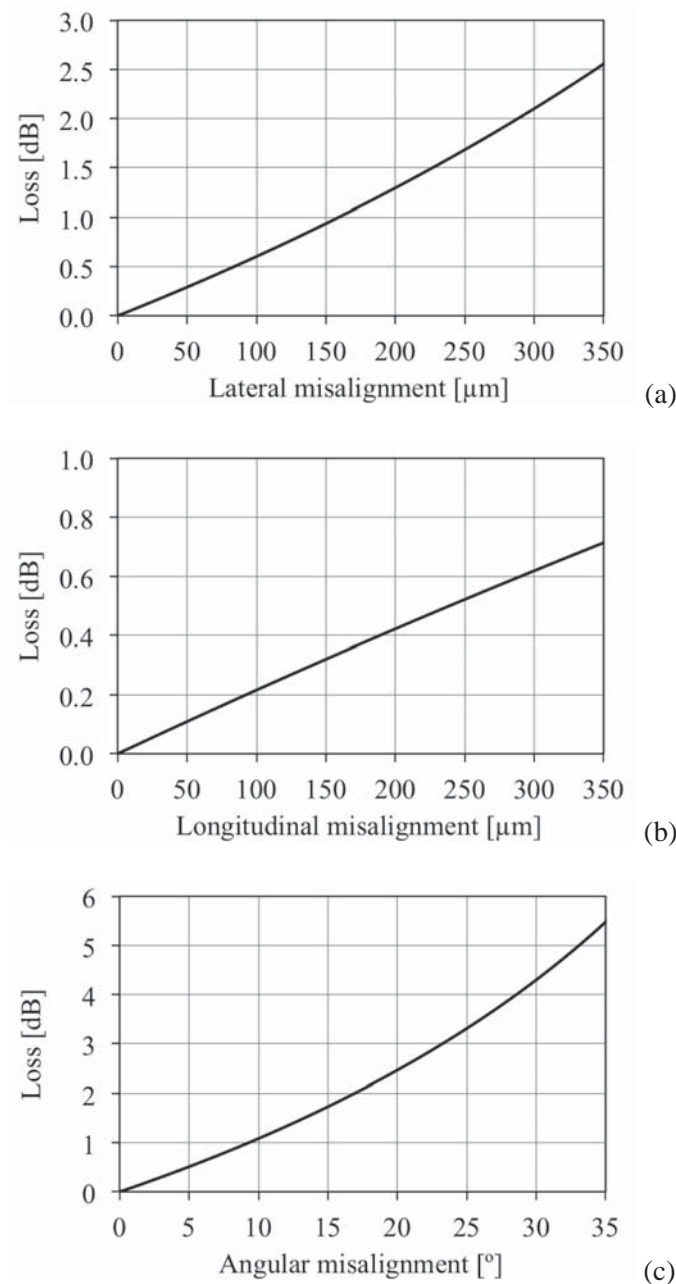


Fig. 2.7: POF-to-POF coupling loss due to (a) lateral, (b) longitudinal and (c) angular misalignment.



2.4 Data transmission techniques for increasing the channel capacity

In this thesis two data transmission techniques were used to overcome the bandwidth limitation of a POF WDM channel, which is primarily caused by the intermodal dispersion of SI-POF. Those were:

1. Non-return-to-zero (NRZ) modulation in combination with electronic dispersion compensation, in particular feed-forward equalization (FFE);
2. Discrete multitone (DMT) modulation.

In the single-channel POF systems with intensity modulation and direct detection (IM/DD) those are well known techniques for increasing the channel capacity, e.g. [Loquai13] and [Vinogradov11] respectively. The next two subsections briefly introduce the two techniques. For detailed explanations about FFE equalization and DMT modulation it is referred to the relevant literature, e.g. [Proakis08], [Voigt14] and [Cioffi91], [Lee09a] respectively.

2.4.1 Non-return-to-zero modulation and feed-forward equalization

According to the Nyquist theorem for two-level signalling, the maximum bit rate (in bits per second) for a noiseless channel of the bandwidth B equals $2B$. Since the real systems encounter noise, this theoretical limit cannot be achieved. Therefore, for 100 m SI-POF link the data rates less than 100 Mb/s are possible. If the data rate further increases, the eye diagram of the received signal becomes partially or completely closed due to the combination of the ISI and additive noise (introduced e.g. by receiver's transimpedance amplifier).

The equalization techniques are used to open the eye diagram at the receiver for clock and data recovery (CDR). In its principle, the equalizer compensates for ISI, which is deterministic (unlike the random noise) and determined by the low pass frequency response of a POF channel. In the thesis a simple linear FFE equalization technique was employed to correct the distorted signal waveforms at the receiver. An FFE equalizer is realized as a discrete-time finite impulse response filter with adjustable coefficients. The output of the equalizer is obtained as the weighted sum of the delayed samples of the input signal as:

$$V_e(t) = \sum_{k=0}^{N-1} c_k V_r(t - kT_D), \quad (2.20)$$

where $V_e(t)$ is the equalized voltage sample at the time t , c_k is the equalizer coefficient (weighting factor), T_D is the tap delay, and $V_r(t - kT_D)$ is the k times delayed uncorrected received voltage sample. A block diagram of the FFE equalizer is shown in Fig. 2.8.

Through its coefficients the equalizer may synthesize a transfer function corresponding to the inverted channel frequency response, thus eliminating the ISI. In a noisy POF channel, and due to inverting the channel frequency response, this would lead to great noise amplification

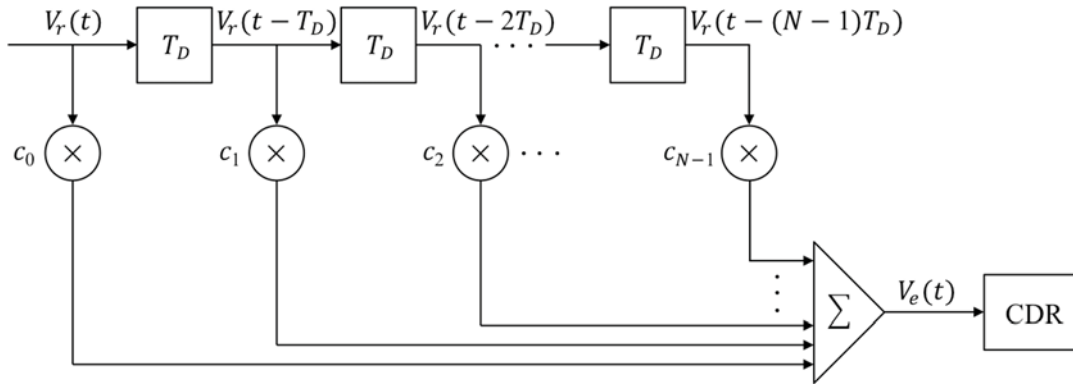


Fig. 2.8: Basic structure of an FFE equalizer.

at higher frequencies where the channel frequency response is small in magnitude. Typically, to minimize the probability of the decision error, the weighting factors are calculated to minimize the noise power at the cost of a certain amount of residual ISI after equalization. The descriptions of different algorithms for optimizing the equalizer coefficients can be found in [Proakis08].

The BER performance of the system was estimated based on the Q-factor of the equalized eye diagram:

$$Q = \frac{V_1 - V_0}{\sigma_1 - \sigma_0}, \quad (2.21)$$

where V_1 and V_0 are the mean values, and σ_1 and σ_0 are the standard deviations of the equalized signal voltages associated with logic 1 and 0 levels respectively, as shown in Fig. 2.9. The corresponding BER was obtained as:

$$BER(Q) = \frac{1}{2} \operatorname{erfc} \left(\frac{Q}{\sqrt{2}} \right), \quad (2.22)$$

where $\operatorname{erfc}(x) = (2/\sqrt{\pi}) \int_x^\infty \exp(-\tau^2) d\tau$ is the complementary error function.

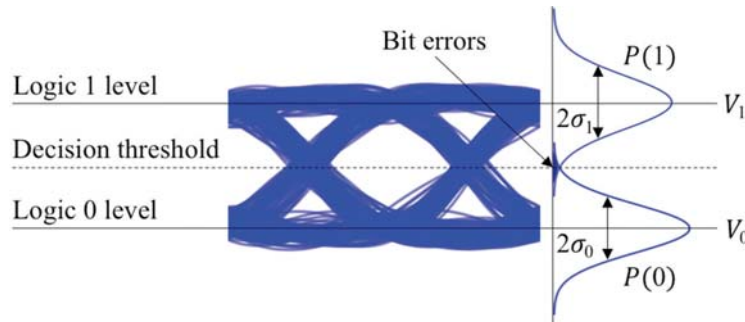


Fig. 2.9: Calculation of the Q-factor from the eye diagram: $P(1)$ and $P(0)$ – probability distributions of received logic 1 and 0 levels respectively.



2.4.2 Discrete multitone modulation

To provide high spectral efficiency of the signals transmitted within POF WDM channels, a DMT modulation technique was used. The DMT is a multicarrier modulation format and represents a baseband version of a better-known orthogonal frequency division multiplexing (OFDM). Unlike the OFDM, which is used in wireless communication systems such as wireless local area networks (WLAN), the DMT is widely employed as enabling technology for digital subscriber lines (DSL), e.g. asymmetric DSL (ADSL) and very high DSL (VDSL). The DMT-based transmission was also shown to be very beneficial for SI-POF communication [Lee09b], [Loquai10], [Vinogradov11].

The DMT technique slices the frequency-selective channel into a large number of subchannels that can be considered to have a flat frequency response. Each subchannel is then used for transmission of a passband signal with quadrature amplitude modulation (QAM). The simultaneous transmission of the low-speed parallel streams reduces the influence of the ISI. Another important property of DMT is that it adapts the signal parameters (QAM size and power in each subchannel) to the characteristic of the communication channel.

The principle of the DMT transmission over an optical IM/DD channel is shown in Fig. 2.10. A high-speed serial data stream is first divided into N parallel lower-speed streams, where N corresponds to the number of subcarriers. Every M bits in each stream are grouped together and mapped into a complex value corresponding to a point of the QAM constellation with 2^M size. The modulation of the complex values onto N different subcarrier frequencies is based on the inverse fast Fourier transform (IFFT). To obtain real-valued time domain signal samples at the output of the IFFT block, a $2N$ -point IFFE has to be carried out. Thereby, the second half of $2N$ IFFT inputs must be complex conjugate of the first half and symmetric around the middle of the input vector, a property referred to as a Hermitian symmetry. The real-valued samples of the DMT time signal are then parallel-to-serial converted and a cyclic prefix (CP) is added as a guard interval at the beginning of each DMT frame to resist to inter-

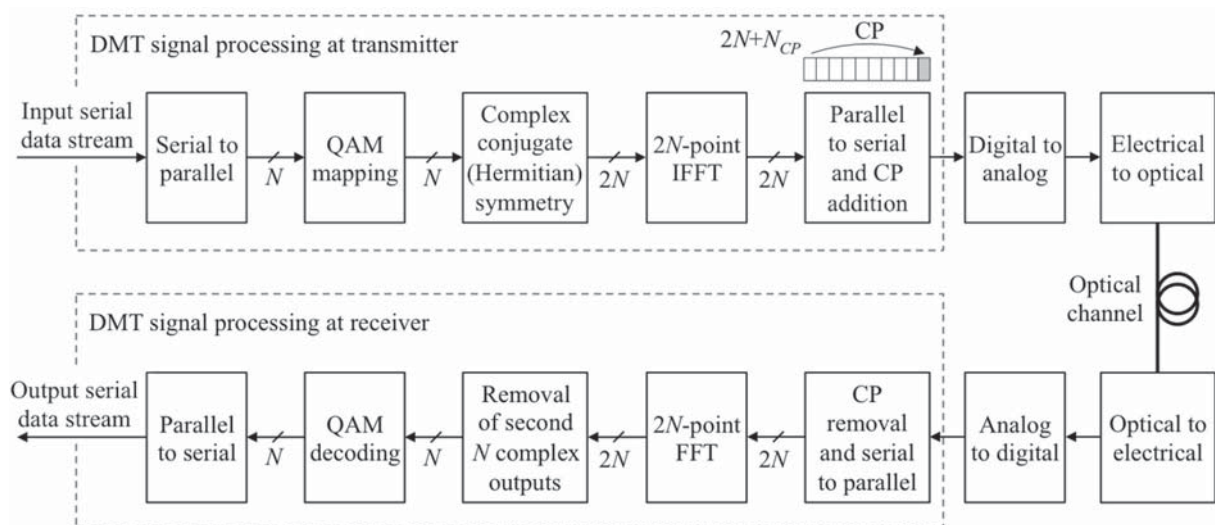


Fig. 2.10: Principle of DMT transmission over an optical IM/DD channel: N_{CP} – length of CP.



frame interference occurring in a band-limited channel. After digital-to-analog conversion, a bipolar continuous-time DMT frame is produced. It is then DC-biased to modulate the intensity of an electrical-to-optical converter.

At the receiver, the DMT waveform is direct-detected, analog-to-digital and serial-to-parallel converted, and demodulated using $2N$ -point fast Fourier transform (FFT). The first N complex outputs of the FFT block are QAM-decoded and parallel-to-serial converted to result in an output serial data stream.

Depending on the signal-to-noise ratio (SNR) of a subchannel, the DMT allocates different number of bits and power for different subchannels. The technique is known as bit loading. There are two types of bit loading algorithms – the margin adaptive and the rate adaptive. The former ones minimize the transmission power for given data rate and BER performance. The latter ones maximize the data rate for fixed total transmission power and BER performance. Having the goal to maximize the data throughput of a POF WDM system, in this thesis the rate-adaptive bit loading was used. From the information theory it is known that the rate adaptive water-filling algorithm provides the optimal bit loading (and power allocation), thereby reaching the channel capacity [Proakis08]. However, it assumes an infinite granularity in constellation size (in number of bits per subchannel), being unsuitable for practical implementation. Instead, a widely employed sub-optimal Chow's rate adaptive bit-loading algorithm was used [Chow95]. For the predetermined BER and total transmission power this numerical algorithm maximizes the bit rate, thereby almost reaching the theoretical channel capacity [Chow95], [Cardiff11]. At the same time it offers a finite granularity in constellation size. This allows easy practical implementation.

2.5 Spectral channels for POF WDM

Besides developing low-IL cost-effective POF WDM components and fast POF WDM systems, it is also important to allocate a unique set of WDM transmission channels in the visible spectrum to support POF WDM applications. Such a set of channels is commonly referred to as a spectral grid.

Spectral grids already exist in the infrared part of the spectrum for use in glass fiber communication. Two recommendations developed by the Telecommunication Standardization Sector of the International Telecommunication Union (ITU-T) specify the frequency and the wavelength grid to support *Dense* and *Coarse* WDM applications respectively. Over the last 15 years the ITU-T developed several more international standards for WDM components and systems in the infrared spectral region. Following the practice established by ITU-T, the terms and concepts provided by the ITU-T recommendations are used in this thesis.



2.5.1 WDM standardization by ITU-T

The terms and concepts relevant for this thesis, in particular for chapter 6, are provided by the following ITU-T Recommendations:

- ITU-T Recommendation G.671, *Transmission characteristics of optical components and subsystems*, 1996 (first edition) / 2012 (in force edition);
- ITU-T Recommendation G.694.1, *Spectral grids for WDM applications: DWDM frequency grid*, 2002 / 2012;
- ITU-T Recommendation G.694.2, *Spectral grids for WDM applications: CWDM wavelength grid*, 2002 / 2003;
- ITU-T Recommendation G.695, *Optical interfaces for coarse wavelength division multiplexing applications*, 2004 / 2015.

Those recommendations are briefly introduced in the next subsections. The actual scopes of the recommendations, especially of G.671 and G.695, extend far beyond presented considerations.

ITU-T Recommendation G.671

The ITU-T Recommendation G.671, *Transmission characteristics of optical components and subsystems*, gives definitions of the transmission-related parameters of the optical components used in long-haul and access networks [ITU12a]. The components covered by the recommendation, among others, include optical filters, connectors, switches, splices, isolators, WDM devices, etc. According to the recommendation, the WDM devices and systems are classified into three categories based on the channel spacing. Those categories are referred to as:

1. Dense WDM, with a frequency spacing between the adjacent channels less than or equal to 1000 GHz;
2. Coarse WDM, with a wavelength spacing between the adjacent channels less than 50 nm, but greater than 1000 GHz (approx. 5.7 nm at 1310 nm and 8 nm at 1550 nm);
3. Wide WDM, with the wavelength spacing between the adjacent channels greater than or equal to 50 nm.

ITU-T Recommendation G.694.1

The ITU-T Recommendation G.694.1, *Spectral grids for WDM applications: DWDM frequency grid*, provides a grid with a narrow optical frequency spacing to support Dense WDM (DWDM) applications [ITU12b]. The grid is anchored to 193.1 THz (1552.52 nm) and supports channel spacings of 100 GHz, 50 GHz, 25 GHz and 12.5 GHz. In the wavelength domain the corresponding spacings are approx. 0.8 nm, 0.4 nm, 0.2 nm and 0.1 nm respectively. Because of the narrow channel spacing, strict requirements for the laser wavelengths are imposed. For 100 GHz channel spacing the typical tolerance for the lasing

wavelength is on the order of ± 0.1 nm. To maintain the wavelength stability, a precise temperature control of the laser transmitters is required. Channel spacings equal to an integer multiple of 100 GHz are also allowed. The recommendation does not impose any limitation to the maximum channel count i.e. the frequency grid has no endpoints.

The DWDM systems tend to be used at a higher level of network hierarchy, typically in backbone networks and metro rings with high capacity. They operate in the C- and L-band where erbium-doped fiber amplifiers are effective [Ramaswami09]. Fig. 2.11 illustrates DWDM channels based on 100 GHz channel spacing. In the C-band, covering 1530-1565 nm wavelength range, a total of 44 DWDM channels are located. The DWDM channels typically provide a capacity of 10 Gb/s to 100 Gb/s over several hundred up to 3000 km. The recent technological advancements allowed further capacity incense to 400 Gb/s over a single wavelength [Zhou12]. One of the highest aggregate data rates ever reported over a single-mode glass fiber employing DWDM technology was greater than 100 Tb/s using 370 channels with 25 GHz spacing [Qian11].

ITU-T Recommendation G.694.2

The ITU-T Recommendation G.694.2, *Spectral grids for WDM applications: CWDM wavelength grid*, defines a set of 18 nominal equidistant central wavelengths to be used for *Coarse* WDM (CWDM) applications [ITU03]. The wavelength grid covers the spectral range from 1271 nm to 1611 nm and specifies 20 nm spacing between the adjacent channels. The nominal central wavelengths of the grid are given in Table 2.3. The comparison of 20 nm CWDM and 100 GHz (0.8 nm) DWDM channel spacing is shown in Fig. 2.11.

Table 2.3: CWDM grid according to ITU-T Recommendation G.694.2.

CWDM channel	Nominal central wavelength [nm]	CWDM channel	Nominal central wavelength [nm]
1	1271	10	1451
2	1291	11	1471
3	1311	12	1491
4	1331	13	1511
5	1351	14	1531
6	1371	15	1551
7	1391	16	1571
8	1411	17	1591
9	1431	18	1611

Unlike DWDM systems, CWDM systems are intended to be cost-effective. That is possible because of the significantly wider channel spacing. To maximize the number of CWDM channels within the usable spectral range of the single-mode glass fiber (from 1260 nm to 1625 nm), the channel spacing was set to 20 nm. This value was formed in the following way:

- To reduce the production costs, the manufacturers of CWDM lasers are allowed to relax tolerances in the production process, resulting in a typical variation of ± 3 nm around the nominal lasing wavelength.
- CWDM systems use lasers without cooling. Consequently, the lasing wavelength changes with the operating temperature. The operating temperature range of a CWDM transmitter is expected to be from 0 to 70°C. Having the typical temperature coefficient of central wavelength of 0.1 nm/°C, the laser wavelength drift of 7 nm around the nominal wavelength was taken into account.
- To accompany ± 6.5 nm variation around the transmitter's nominal central wavelength, the demultiplexers with 13 nm channel passbands are required. For 20 nm channel spacing that leaves 7 nm guardband between the adjacent channels. That is enough to allow implementation of low-cost demultiplexer technologies, typically thin-film filters, rarely gratings (arrayed waveguide and diffraction), for channel separation.

Therefore, the flexibility in CWDM systems is achieved by allowing relaxed tolerances for the laser wavelengths, and by using uncooled lasers and low-cost demultiplexers.

CWDM systems are suited for short-haul communications, typically in metro and access networks, where the transmission distances range between 10 km and 100 km. The capacity

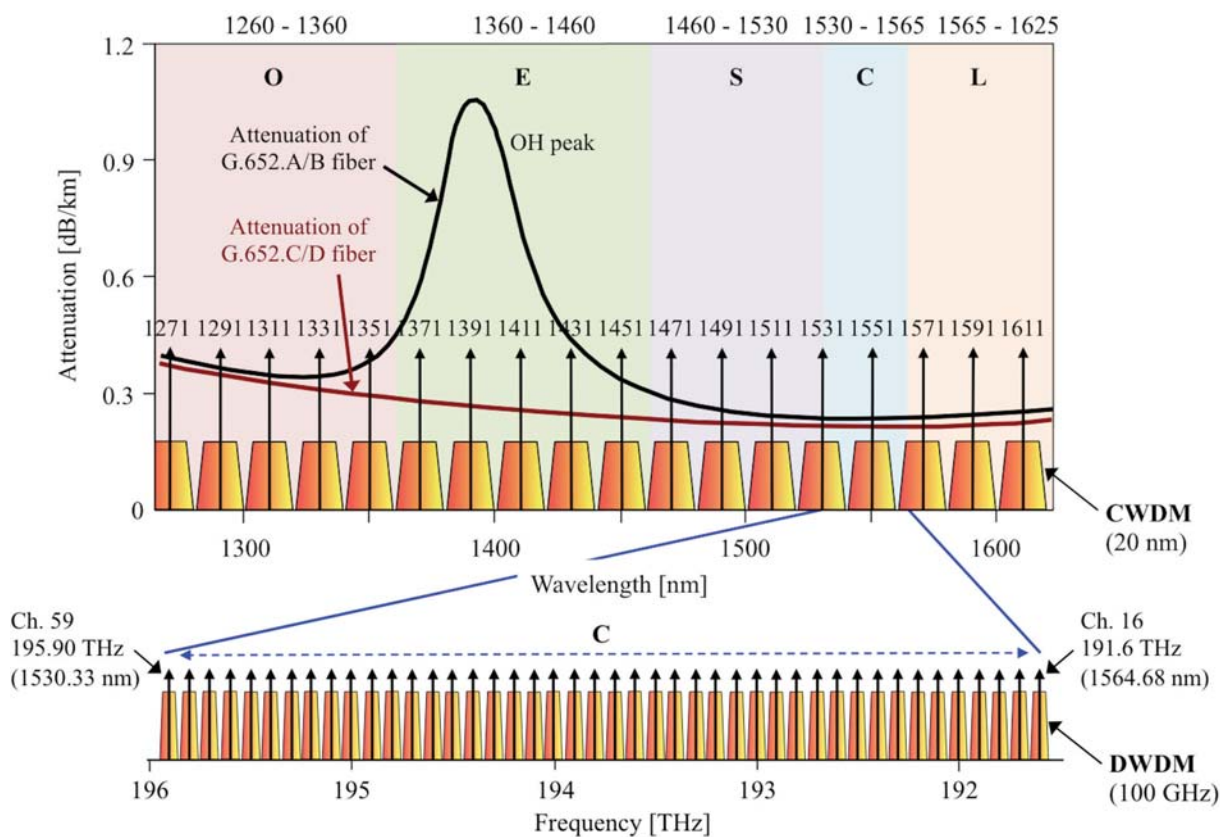


Fig. 2.11: Representation of: (1) 100 GHz DWDM frequency grid according to ITU-T Recommendation G.694.1; (2) 20 nm CWDM wavelength grid according to ITU-T Recommendation G.694.2; (3) attenuation of single-mode glass fiber according to ITU-T Recommendation G.652.A/B (with OH absorption peak) and G.652.C/D (low or zero OH peak).

per wavelength varies between 1.25 Gb/s and 10 Gb/s, depending on the link length [Thiele07]. For 16 channels, each with a 10 Gb/s payload, the maximum data rate of 160 Gb/s over 40 km was reported in [Thiele04].

ITU-T Recommendation G.695

The ITU-T Recommendation G.695, *Optical interfaces for coarse wavelength division multiplexing applications*, defines sets of wavelengths to be used in CWDM applications with different channel counts [ITU10]. Such sets are called channel plans. Even though the CWDM grid offers 18 channels, channel plans are specified for applications with 4, 8, 12 and 16 channels in the way shown in Table 2.4. The first two spectral channels (at 1270 nm and 1290 nm) are typically omitted due to the increased losses caused by the Rayleigh scattering at shorter wavelengths [Thiele07].

Table 2.4: Channel plans according to ITU-T Recommendation G.695.

Nominal central wavelength [nm]	4-channel applications	8-channel applications	12-channel applications	16-channel applications
1271				
1291			*	
1311			*	*
1331			*	*
1351			*	*
1371				*
1391				*
1411				*
1431				*
1451				*
1471		*	*	*
1491		*	*	*
1511		*	*	*
1531	*	*	*	*
1551	*	*	*	*
1571	*	*	*	*
1591	*	*	*	*
1611		*	*	*

The channels plans are designed to maximize the transmission distance of a system. For example, the 4- and 8-channel applications utilize channels in the third window around 1550 nm where the single-mode fiber exhibits minimum attenuation (< 0.3-0.4 dB/km for G.652 fibers). The channels in the E-band were not considered for 12-channel applications



because of the OH absorption peak centered around 1383 nm. That allowed the utilization of both the older G.652.A/B fibers (with water peak) and the newer G.652.C/D fibers (low or zero water peak) (see Fig. 2.11) in 12-channel applications. The realization of 16-channel applications, also known as the full spectrum CWDM, is only possible with low or zero water peak fibers.

3 POF demultiplexer employing thin-film interference filters

This chapter focuses on the experimental realization of a thin-film interference filter-based SI-POF demultiplexer using a modular and precisely adjustable setup. In a step-by-step approach, the intermediate solutions with two and three channels were first established. In addition, two different configurations of the target demultiplexer setup with four channels were realized. The principle of operation and the approach for experimental realization are explained for the simplest case of a two-channel demultiplexer. The same basic principles also apply to the demultiplexers with higher channel count.

3.1 Basic concept of a demultiplexer employing thin-film interference filters

The principle of operation of a two-channel SI-POF demultiplexer is illustrated in Fig. 3.1. An SI-POF link was connected to the input of the demultiplexer over a connector interface (1). A multi-wavelength light beam diverging from 1 m long ingoing SI-POF (2) was first collimated by means of a lens (3). The separation of two wavelength channels was performed by a dichroic mirror (4), which was placed at an angle of 45° with respect to the optical axis of an incident beam. A hard-coated bandpass interference filter (5) further suppressed the remaining unwanted spectral components from the demultiplexed wavelength channel. The filtered light beam was focused onto the end face of 1 m long outgoing SI-POF

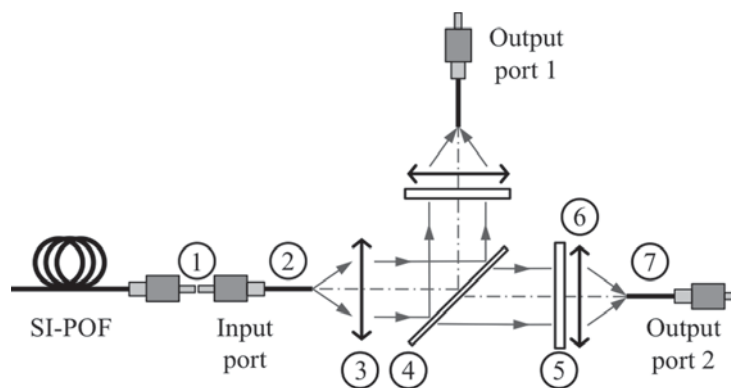


Fig. 3.1: Principle of operation of a two-channel SI-POF demultiplexer employing thin-film interference filters: 1 – connector coupling; 2 – 1 m ingoing SI-POF; 3 – collimating lens; 4 – dichroic mirror; 5 – bandpass interference filter; 6 – focusing lens; 7 – 1 m outgoing SI-POF.

(7) by means of another lens (6) and, depending on the type of measurement, fed to an optical spectrum analyzer, photoreceiver or power meter.

The connector interface i.e. connector coupling at the input port was considered to be an integral part of the demultiplexer. It primarily allowed easy connection of a mode mixer or SI-POF links of different length to the demultiplexer. Furthermore, after an initial alignment, the position of the ingoing fiber was left unchanged with the respect to the collimating lens. Keeping the same optical axis and the distance between the components ensured a reproducible measurement condition, regardless of the input to the demultiplexer. To minimize the IL introduced by the connector coupling in each of the demultiplexer channels, an index-matching gel was applied between the connectors. The 1 m length of the ingoing and the outgoing SI-POF was selected to allow easy manipulation with terminating connectors.

The lenses available for collimation and focusing of light were a single Qioptiq aspheric condenser lens with 18 mm focal length (at 588 nm) and 21.4 mm clear aperture, and four Thorlabs A240TM-A aspheric lenses with 7.93 mm focal length (at 633 nm) and 8 mm clear aperture. Having a large core diameter and high numerical aperture of SI-POF, as well as a broad range of operating wavelengths (400-700 nm), both the monochromatic and the chromatic aberrations were inherent to the demultiplexing system from Fig. 3.1. With the available aspheric lenses it was possible to reduce the spherical aberrations and also the off-axis aberrations such as coma and astigmatism [Hecht05]. However, the setup was much more subject to the chromatic aberrations due to the operation over a broad spectral range. From that standpoint, the available lenses could not provide optimum performance. Nevertheless, the effect of chromatic aberrations was to a certain extent reduced by an adjustable design of the demultiplexer setup, which will be discussed in the next subchapter. In all realized demultiplexer setups the larger Qioptiq lens was used to collect highly divergent light exiting the ingoing SI-POF. The aspheric lenses from Thorlabs were employed in the output ports for focusing of light.

The basic parameters of dichroic mirrors utilized in different demultiplexer setups are given in Table 3.1. The Thorlabs dichroic mirrors with 425 nm, 505 nm, and 567 nm cutoff wavelengths are designed as longpass, whereas the one from Edmund Optics with the cutoff at 650 nm has a shortpass characteristic. As illustrated in Fig. 3.1, the optical axis of the collimated beam was shifted upon passing the dichroic mirror. The amount of shift depends on the material and thickness of the substrate, and on the wavelength of transmitted light. Having the fused silica as a common substrate for the dichroic mirrors from Table 3.1, the 3.2 mm thick dichroic mirrors from Thorlabs introduced larger axis shift than the one from Edmund Optics (1.05 mm thick). The shorter the wavelength is, the higher is the refractive index of fused silica, and therefore the bending of the light path within the substrate. Taking 400 nm as a lower bound of the operating wavelength range, the maximum shift of the optical axis introduced by a single Thorlabs dichroic mirror was 1.02 mm.

Even though the selected dichroic mirrors could perform the separation of different wavelength channels, they did not ensure good isolation between the demultiplexed channels

Table 3.1: Basic parameters of hard-coated dichroic mirrors utilized in different demultiplexer setups (datasheet information).

Type	longpass			shortpass
Cutoff wavelength [nm]	425	505	567	650
Transmission band [nm] (> 85%)	440-700	520-700	584-700	400-630
Reflection band [nm] (> 90%)	380-410	380-490	380-550	675-850
Manufacturer	Thorlabs			Edmund Optics

nor optimally shaped their spectral response [Jončić13a]. For those reasons a bandpass interference filter was employed in each of the output channels. Since designed for the normal incidence, on the optical path the filter was installed in front of the aspheric lens. The basic parameters of hard-coated bandpass interference filters from Edmund Optics utilized in different demultiplexer setups are given in Table 3.2. The center wavelengths of the filters were selected to comply with the nominal center wavelengths of the available laser diodes from Table 5.1. The filters centered at 405 nm, 450 nm, 525 nm and 650 nm were intended for use in combination with the dichroic mirrors from Thorlabs. For the intended application other passband bandwidths could have also been selected, e.g. 25 nm bandwidth for each filter. The filters centered at 640 nm and 660 nm were intended for use with 650 nm cutoff dichroic mirror. To provide higher channel isolation their bandwidth had to be limited to 10 nm.

Table 3.2: Basic parameters of hard-coated bandpass interference filters from Edmund Optics utilized in different demultiplexer setups (datasheet information).

Center wavelength [nm]	405	450	525	640	650	660
3 dB passband bandwidth [nm]	10	10	50	10	50	10

3.2 Experimental setup

A CAD model of the two-channel demultiplexer is shown in Fig. 3.2. The demultiplexer was realized with the components from LINOS Microbench series and was installed on a vibration suppressing optical table. A 4-rod construction system (1) supported with the mounting holders (2) was used to bring together the Microbench mechanical components holding the fibers and bulk optical elements. The ingoing and the outgoing fibers, which were terminated with SMA connectors, were mounted over SMA fiber adapters (3) into XYZ fine adjustment units (4). The units provided a travel range of ± 1 mm in the x - and y -direction, and when anchored to the 4-rod system allowed a travel of 5 mm along the optical axis (z -direction). The aspheric lenses were mounted in XY precision translation stages (5) having a travel range of ± 1 mm along the x - and y -direction. The collimating lens with 25 mm mounting diameter was directly mounted in the stage, whereas the focusing lenses with a smaller mounting diameter were mounted over reduction inserts. In each of the output ports the bandpass



interference filter was mounted in the XY precision translation stage in front of the aspheric lens. The dichroic mirror glued to an adjustable mirror insert (6) was positioned within a beam splitter cube (8) over a rotation adjustment for cube insert (7).

Accordingly, the demultiplexer setup allowed very precise positioning and alignment of the fiber end faces, lenses and dichroic mirrors. The available degrees of freedom can be summarized as follows:

- End faces of the ingoing and the outgoing fibers: x -, y - and z -direction translation;
- Collimating and focusing lenses: x - and y -direction translation;
- Dichroic mirrors: rotation and tip/tilt (when applied together tip and tilt result in translation along the direction perpendicular to the incoming optical axis).

The orientation of the x -, y - and z -direction for the input port and the output port 2 of the demultiplexer is shown in Fig. 3.2.

The alignment of the demultiplexer setup was performed in the following manner. At first, only the lenses and interference filters were installed in the setup, whereas the dichroic mirror and adjustable mirror insert were kept aside. Using the XYZ fine adjustment unit and XY precision translation stage in the input port, the end face of the ingoing fiber had to be positioned with respect to the collimating lens such that the collimated beam was centered within the rod system, i.e. such that the optical axis overlapped with the central axis of the rod system. The validity of the alignment was inspected with a LINOS alignment plate with printed crosshairs, which had to be positioned at different locations along the rod system. For

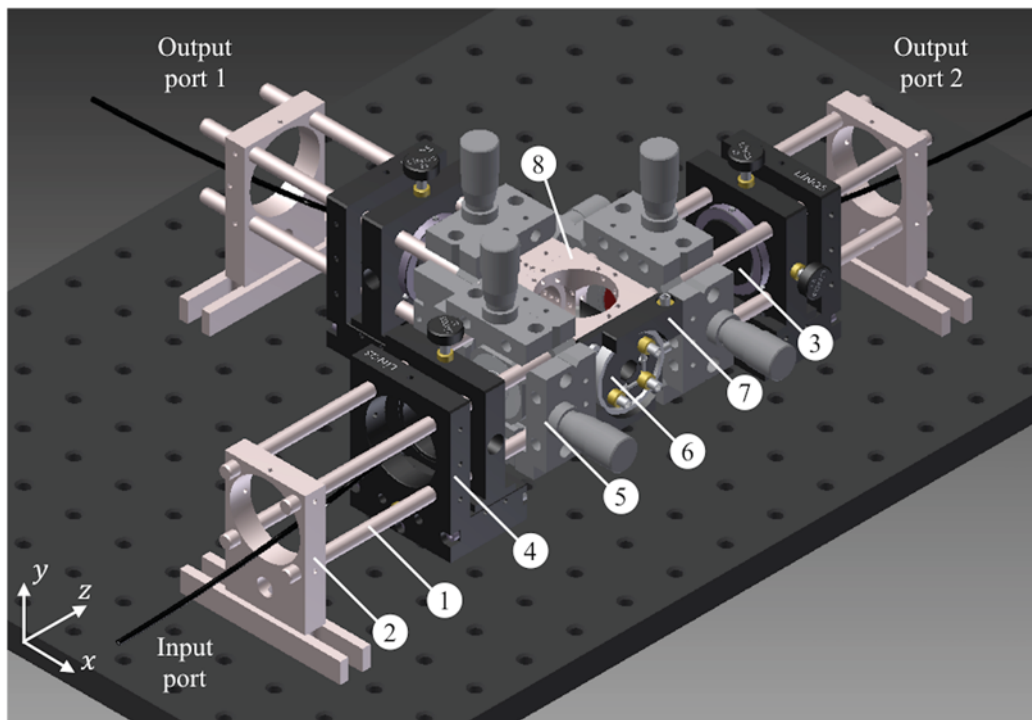


Fig. 3.2: CAD model of the two-channel demultiplexer: 1 – construction rod; 2 – mounting holder; 3 – SMA fiber adapter; 4 – XYZ fine adjustment unit; 5 – XY precision translation stage; 6 – adjustable mirror insert; 7 – rotation adjustment for cube insert; 8 – beam splitter cube.



that purpose, the fine adjustment unit and the precision translation stage in the output port 2 were brought along the rod system into the furthest position from the beam splitter cube. That allowed the alignment plate to be positioned directly after the beam splitter cube and somewhat further, e.g. before the precision translation stage.

In the next step, the dichroic mirror was mounted in the setup and aligned using the adjustable mirror insert and rotation adjustment for cube insert such that the axis of the reflected beam was centered within the rod system of the output port 1. The same procedure as in the output port 2 was used to prove the validity of alignment. The maximum shift of 1.02 mm of the beam passing the dichroic mirror was within the travel range of the lens and fiber positioners in the output port 2.

The final step involved alignment of the focusing lenses and fiber end faces in the output ports. Furthermore, the distances between the fibers and the lenses in the input and the output ports were manipulated in order to maximize the optical throughput in each of the demultiplexer channels. For the available lenses that primarily implied increasing the distance between the ingoing fiber end face and the collimating lens, such that slightly converging rather than collimated beam was obtained after the lens. Thereby, a compromise between the reduced beam diameter that was better suited to the smaller clear aperture of the focusing lens, and the amount of light captured by the collimating lens had to be found. The optimal position, corresponding to the maximum optical throughput, was estimated by monitoring the spectral response of the channel on the optical spectrum analyzer.

Due to the aspheric lenses employed, the effect of chromatic aberrations on the collimating lens could not be reduced. On the other hand, by applying the z-direction translation using XYZ fine adjustment unit, it was possible to optimally position the outgoing fiber end face with respect to the focus point in each of the output ports.

To measure the transfer function of the demultiplexer, a Yokogawa AQ4305 white light source followed by a cylinder mode mixer according to JIS 6863 provided a wide spectral range (400-700 nm) to the input of the demultiplexer. The spectral responses of the channels were recorded by a Yokogawa AQ-6315A optical spectrum analyzer.

3.3 Measurement results for a two-channel demultiplexer

The principle of operation and the CAD model of the two-channel demultiplexer are already shown in Fig. 3.1 and Fig. 3.2 respectively. Fig. 3.3 shows three different transfer functions of the corresponding setup. The 505 nm cutoff dichroic mirror was used to separate the wavelength channels in Fig. 3.3a and Fig. 3.3b. The interference filters centered at 405 nm and 650 nm were utilized in Fig. 3.3a, whereas the filters centred at 450 nm and 525 nm were used in Fig. 3.3b. The 650 nm cutoff dichroic mirror and 640 nm and 660 nm interference filters were used in Fig. 3.3c. Table 3.3 summarizes the basic parameters of the realized demultiplexers, with the IL uniformity defined as the difference between IL of the channel experiencing the highest and channel experiencing the lowest attenuation.

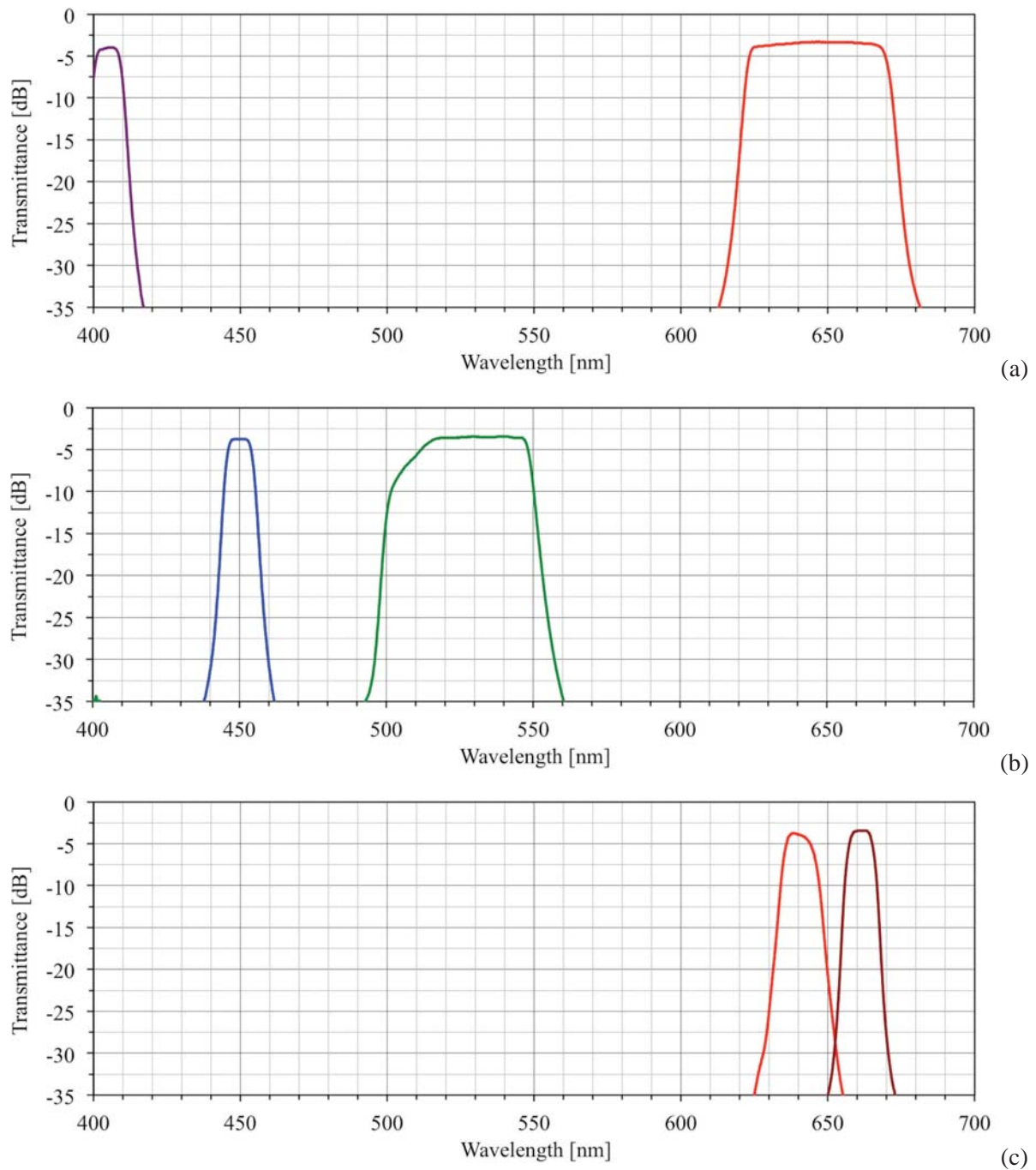


Fig. 3.3: Transfer function of the two-channel demultiplexer with the channels centered at: (a) 405 nm and 646.6 nm; (b) 450 nm and 528.5 nm; (c) 640.3 nm and 661.2 nm.

Table 3.3: Basic parameters of the two-channel demultiplexer.

Transfer function representation	Fig. 3.3a		Fig. 3.3b		Fig. 3.3c	
Output port	1	2	1	2	1	2
Center wavelength [nm]	405	646.6	450	528.5	661.2	640.3
3 dB passband bandwidth [nm]	9.3	47.9	9.2	41	9	10.6
Minimum IL [dB]	3.98	3.30	3.7	3.42	3.39	3.74
IL uniformity [dB]	0.69		0.28		0.35	
(Non)adjacent channel isolation [dB]	> 30		> 30		> 30	

3.4 Operating principle and measurement results for a three-channel demultiplexer

By installing a second dichroic mirror in the demultiplexer setup, it was possible to separate three wavelength channels. In general, the count of dichroic mirrors is by one smaller than the required channel count. The principle of operation of a three-channel demultiplexer is shown in Fig. 3.4. To keep the collimated beam in the output port 3 within the travel range of the lens and fiber positioners, the second dichroic mirror was rotated counterclockwise by 90° with respect to the first one. Thereby, the shift of the optical axis of the collimated beam upon passing the first dichroic mirror was entirely compensated upon passing the second one.

Two different transfer functions and basic parameters of the corresponding setups are shown in Fig. 3.5 and Table 3.4 respectively. The 505 nm and 567 nm cutoff dichroic mirrors were used to separate the wavelength channels. In Fig. 3.5a the interference filters centered at 405 nm, 525 nm and 650 nm were employed in the output ports 1, 2 and 3 respectively. In Fig. 3.5b the filter centered at 450 nm was used instead of 405 nm filter in the output port 1.

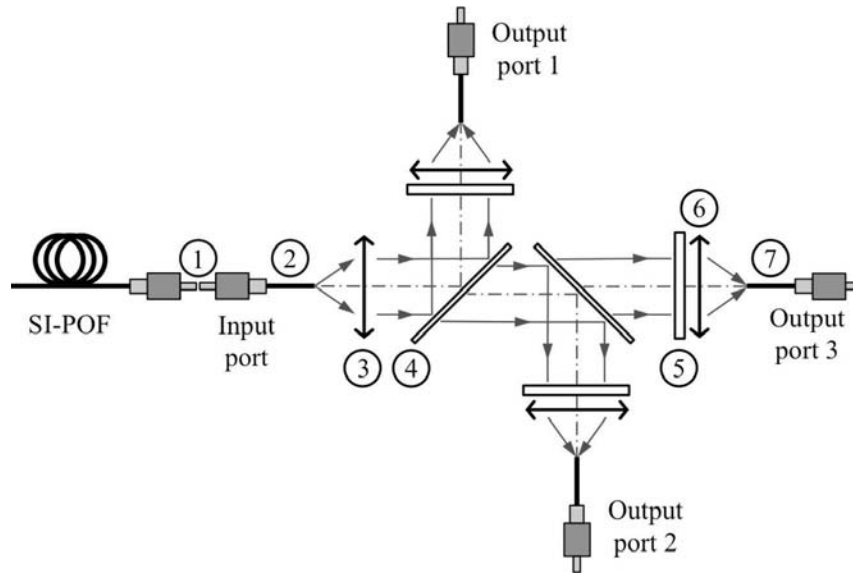
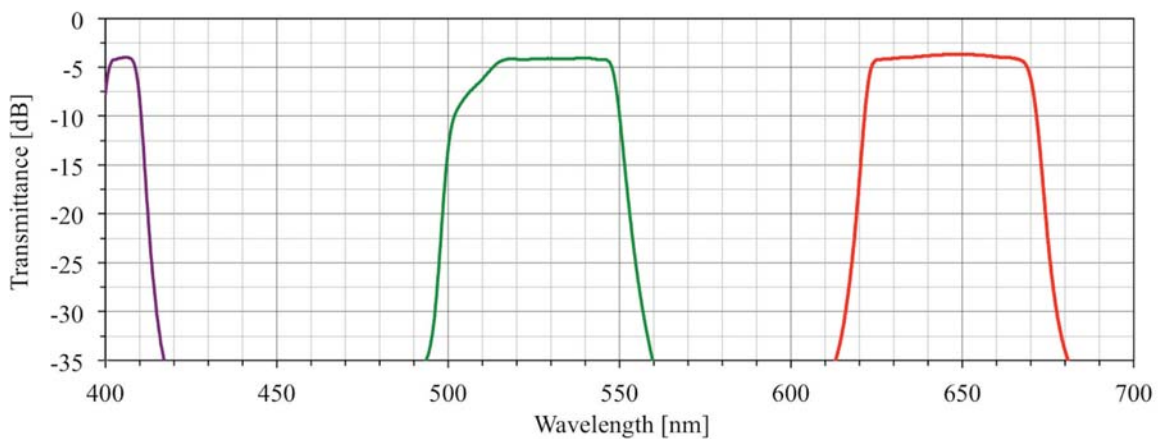


Fig. 3.4: Principle of operation of a three-channel SI-POF demultiplexer employing thin-film interference filters (see enumeration in Fig. 3.1).



(a)

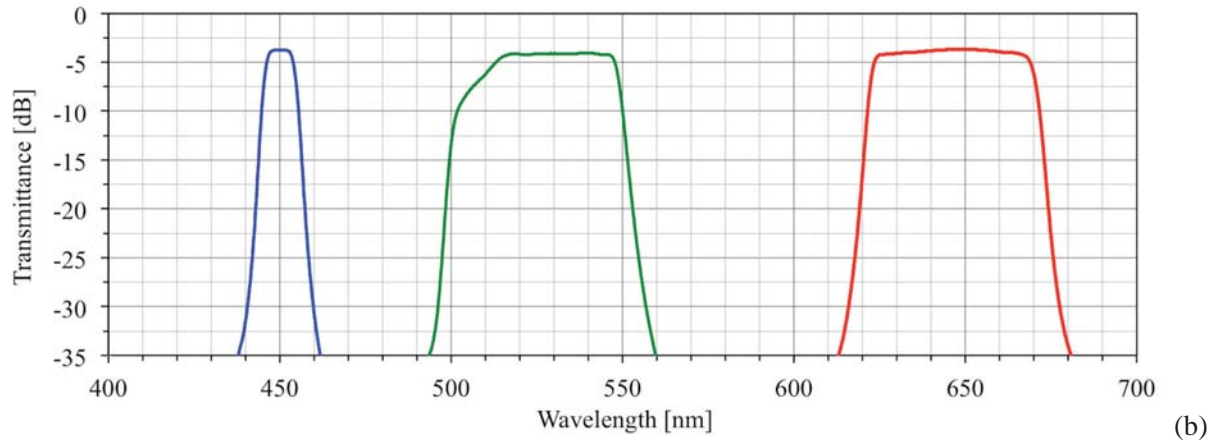


Fig. 3.5: Transfer function of the three-channel demultiplexer with the channels centered at: (a) 405 nm, 528.3 nm and 646.4 nm; (b) 450 nm, 528.3 nm and 646.4 nm.

Table 3.4: Basic parameters of the three-channel demultiplexer.

Transfer function representation	Fig. 3.5a			Fig. 3.5b		
Output port	1	2	3	1	2	3
Center wavelength [nm]	405	528.3	646.4	450	528.3	646.4
3 dB passband bandwidth [nm]	9.3	41.2	47.8	9.2	41.2	47.8
Minimum IL [dB]	4.00	3.99	3.65	3.74	3.99	3.65
IL uniformity [dB]	0.37			0.28		
(Non)adjacent channel isolation [dB]	> 30			> 30		

3.5 Operating principle and measurement results for a four-channel demultiplexer

By extending the channel count to four, it was possible to investigate two different demultiplexer configurations. Those were:

- Serial configuration;
- Two-stage configuration.

The principle of operation of a four-channel demultiplexer with serial configuration is shown in Fig. 3.6. In this configuration the dichroic mirrors were cascaded such that each mirror (except the last one) demultiplexed a single wavelength channel while passing all other wavelengths.

For practical realization 425 nm, 505 nm and 567 nm cutoff longpass dichroic mirrors were cascaded so that the interference filters centered at 405 nm, 450 nm, 525 nm and 650 nm could be implemented in the output ports 1 to 4 respectively. The corresponding transfer function and the basic parameters of the demultiplexer are shown in Fig. 3.7 and Table 3.5

respectively. The factors contributing to high IL in the output ports 3 and 4 are discussed in the next subchapter.

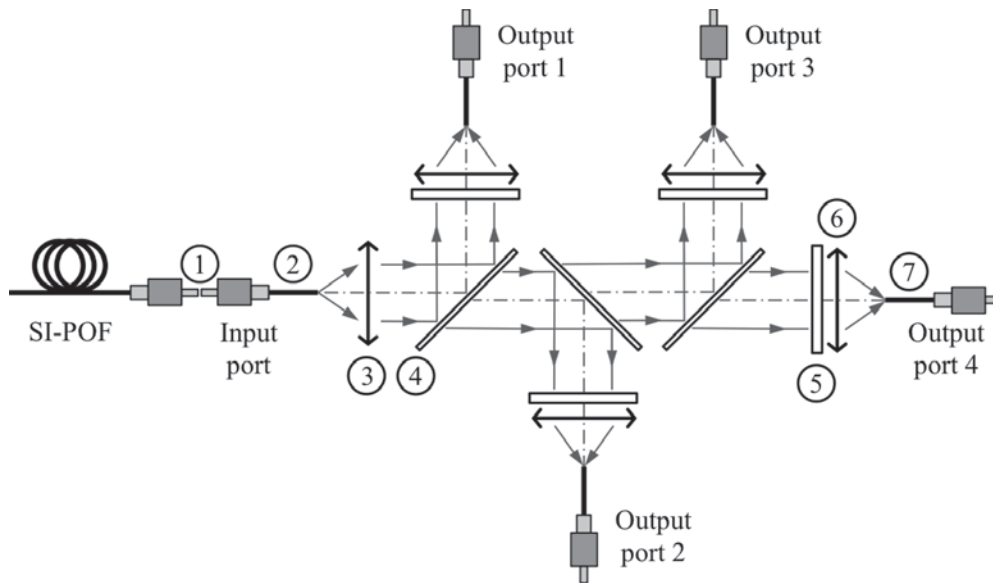


Fig. 3.6: Principle of operation of a four-channel SI-POF demultiplexer with serial configuration (see enumeration in Fig. 3.1).

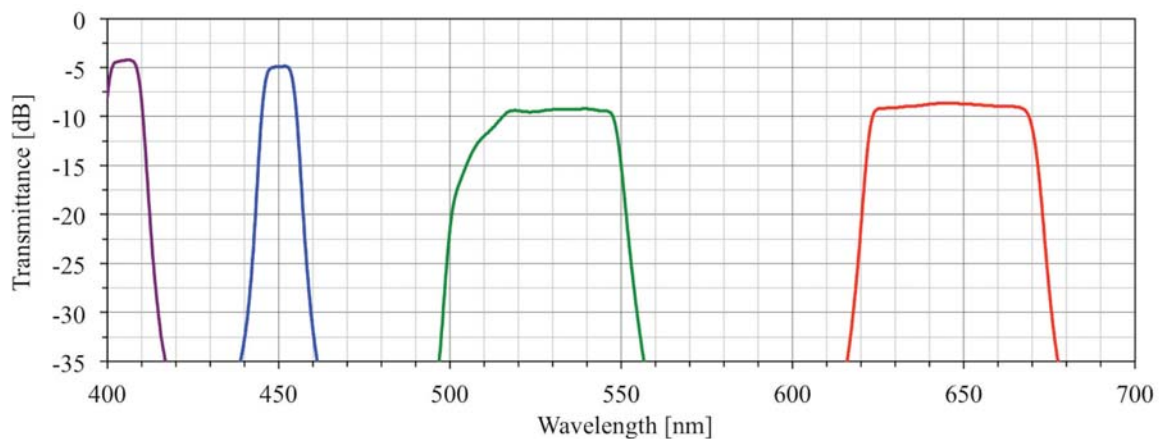


Fig. 3.7: Transfer function of the four-channel demultiplexer with serial configuration and the channels centered at 404.9 nm, 450.1 nm, 529.1 nm and 646.4 nm.

Table 3.5: Basic parameters of the four-channel demultiplexer with serial configuration.

Output port	1	2	3	4
Center wavelength [nm]	404.9	450.1	529.1	646.4
3 dB passband bandwidth [nm]	9.4	9.2	39.6	47.8
Minimum IL [dB]	4.24	4.86	9.21	8.63
IL uniformity [dB]	4.97			
(Non)adjacent channel isolation [dB]	> 30			



The principle of operation of a four-channel demultiplexer with two-stage configuration is shown in Fig. 3.8. The first stage of the demultiplexer, represented by a dichroic mirror that follows directly after the collimating lens, split the incident spectrum into two spectral bands. The separation of the individual wavelength channels was then performed within the second stage of the demultiplexer. The corresponding laboratory setup is shown in Fig. 3.9.

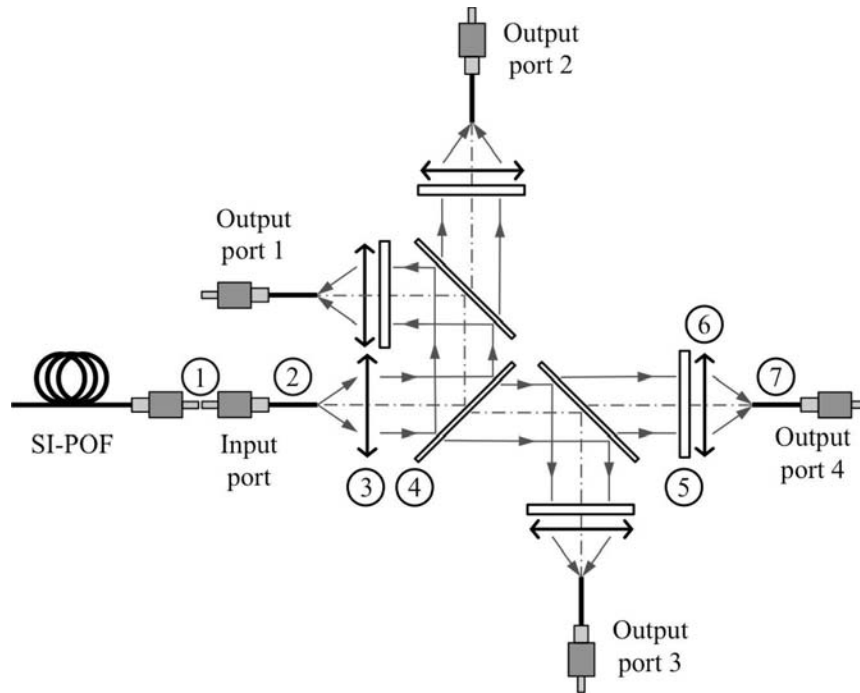


Fig. 3.8: Principle of operation of a four-channel SI-POF demultiplexer with two-stage configuration (see enumeration in Fig. 3.1).

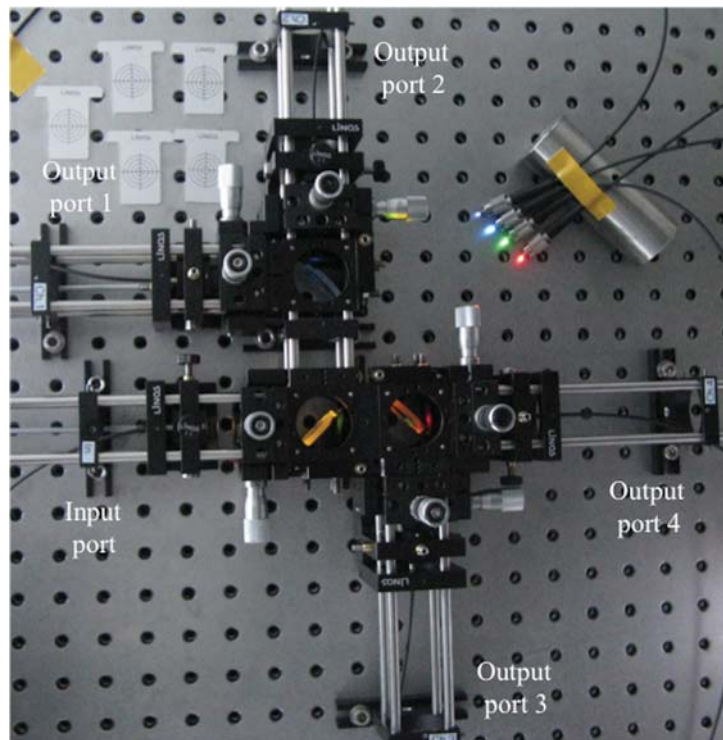


Fig. 3.9: Laboratory setup of the four-channel demultiplexer with two-stage configuration.

The practical realization was carried out with 505 nm cutoff longpass dichroic mirror in the first stage of the demultiplexer. It reflected the lower spectral band so that 425 nm cutoff dichroic mirror was used in the second stage to demultiplex the signals for the output ports 1 and 2 in which 405 and 450 nm filters were employed respectively. The upper spectral band transmitted by 505 nm mirror was demultiplexed in the second stage by 567 nm dichroic mirror. The filters centered at 525 nm and 650 nm were used in the output ports 3 and 4 respectively.

The corresponding transfer function is shown in Fig. 3.10. The basic parameters of the demultiplexer are given in Table 3.6. The measurement results for the four-channel demultiplexer with two-stage configuration were presented at the International Conference on Plastic Optical Fibers (ICPOF) 2013 [Jončić13b]. To comply with all other measurements shown in this chapter, which were performed two years thereafter, the demultiplexer setup was assembled and characterized again. While preserving the same principal behaviour of the spectral response, the minimum IL in the output ports 1 to 4 was 6.15 dB, 5.44 dB, 4.21 dB and 3.85 dB respectively. Those were by 0.49 dB, 0.89 dB, 0.74 dB and 0.66 dB higher values than those reported in [Jončić13b].

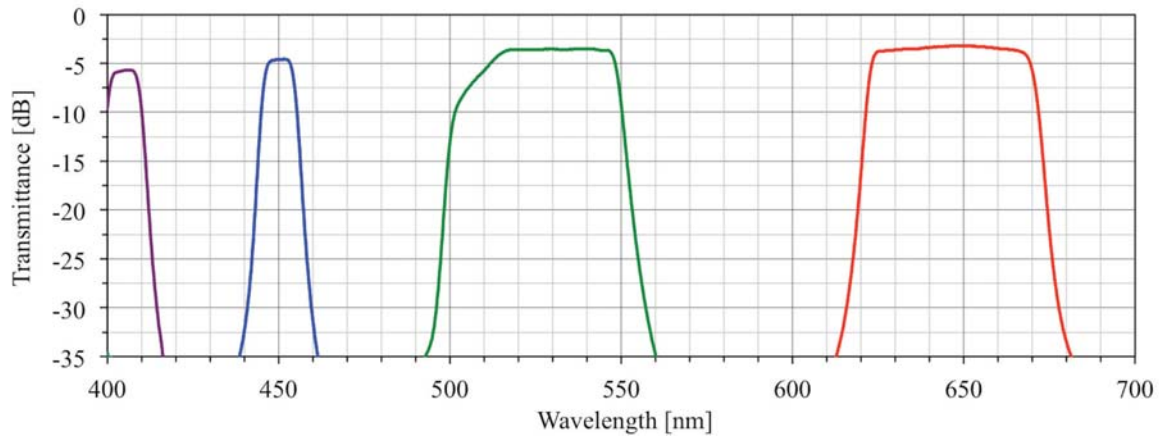


Fig. 3.10: Transfer function of the four-channel demultiplexer with two-stage configuration and the channels centered at 404.9 nm, 450.1 nm, 528.3 nm and 646.4 nm [Jončić13b].

Table 3.6: Basic parameters of the four-channel demultiplexer with two-stage configuration [Jončić13b].

Output port	1	2	3	4
Center wavelength [nm]	404.9	450.1	528.3	646.4
3 dB passband bandwidth [nm]	9.4	9.3	41.6	47.6
Minimum IL [dB]	5.66	4.55	3.47	3.19
IL uniformity [dB]	2.47			
(Non)adjacent channel isolation [dB]	> 30			

3.6 Discussion

The transfer functions shown in Fig. 3.3, Fig. 3.5, Fig. 3.7 and Fig. 3.10 comprised for each demultiplexer channel:

- Loss of the connector interface at the demultiplexer input;
- Attenuation of 1 m ingoing and 1 m outgoing SI-POF;
- Propagation losses through the setup between the fiber end faces.

The loss of the connector interface was minimized by applying the index-matching gel. This loss downscaled the transfer function of the demultiplexer by approx. 0.5 dB. To obtain the performance of the optomechanical setup itself, the value of 0.5 dB should be added to the measured transmittance values. The propagation losses included the Fresnel loss at the end face of the ingoing and the outgoing fiber, the losses introduced by the optical components (including reflections on the anti-reflection coatings), and the coupling losses due to the setup misalignments, optical aberrations and clear aperture of components. For the perfectly aligned components and for given distances between them (obtained e.g. from the CAD model), the minimum loss of the demultiplexer could be estimated by means of an optical ray tracing software. However, that work was beyond the scope of this thesis.

The shape of the spectral response of each demultiplexer channel was predominantly determined by an interference filter that was used. Those filters provided flat-top response, steep transition slopes, and high isolation between the channels due to an optical density greater than 4 (transmission of less than 0.01 %) in the rejection bands within 400-700 nm region. The deviations of the channels from the nominal central wavelengths and bandwidths of interference filters comply with the center wavelength and passband bandwidth tolerances of ± 2 nm and ± 5 nm for 10 nm and 50 nm filters respectively. An exception is the green channel where the spectral response curve was truncated by 505 nm cutoff dichroic mirror with the transmission band starting at 520 nm.

The two-channel demultiplexer was realized to determine the minimum IL required for channel separation. In all three cases the IL ranged between 3.3 dB and 4 dB. The difference in IL of the channels could have been caused by different transmittances of filters and dichroic mirrors. Furthermore, the distance between the ingoing fiber and the collimating lens was adjusted such that the optical throughput was maximized (IL minimized) for the channel experiencing higher attenuation. In all three cases those were the shorter wavelength channels. As a consequence, the longer wavelengths experienced smaller beam convergence after the collimating lens. That led to the increased IL in the longer wavelength channels, resulting also in better IL uniformity.

The two-channel demultiplexers in Fig. 3.3a and 3.3b demonstrated that even though the same dichroic mirror was used for channel separation, the interference filters employed in the output channels determined the operating wavelengths of the demultiplexer. The demultiplexer in Fig. 3.3b is the first SI-POF demultiplexer for the red spectral window reported so far. It offers a narrow channel spacing of 20.9 nm supporting the spectral grid

proposal from chapter 6. Furthermore, it complies well with 650 nm attenuation minima of SI- and GI-POF [Ziemann08], and is suitable for use with 640 nm and 660 nm red laser diodes (see Fig. 6.3).

By extending the channel count to three, the IL in the shortest wavelength channel (violet or blue) remained the same, while the IL in two longer wavelength channels was increased, but still remained below 4 dB. The three-channel demultiplexer was realized for direct performance comparison with the solutions offered by [Kruglov12], [Pinzon14] and [Junger02]. The demultiplexer from Fig. 3.5a outperforms the one from [Kruglov12] by at least 2 dB in any of the output ports. It also slightly outperforms the three-channel plane grating-based demultiplexer from [Pinzon14]. Compared to [Junger02], the demultiplexer from Fig. 3.5b offers an overall IL of 11.5 dB at 450 nm, 520 nm and 650 nm, which is 0.5 dB higher than the demultiplexer from [Junger02]. On the other hand, it provides 2.2 dB better IL uniformity.

The four-channel demultiplexer introduced an additional channel in the short wavelength region. That allowed simultaneous operation at the violet and blue wavelengths, which are both very attractive for POF communication due to the availability of commercial laser diodes. Two different demultiplexer configurations offered significantly different performance.

In the serial configuration the longer wavelength channels corresponded to the higher output ports. Because of the longer optical path compared to the shorter wavelength channels, the longer wavelength channels:

- Were more sensitive to alignment inaccuracies;
- Encountered more optical components (dichroic mirrors);
- Suffered from stronger optical aberrations;
- Experienced increased beam radius due to the beam divergence caused by the finite size of the source fiber [Diaz12].

The influence of those effects can be observed in the transfer function from Fig. 3.7, where the green and red channels experienced significantly higher IL than the violet and blue ones. If the effect of alignment inaccuracy, which is a parameter related to the particular setup adjustment, would be disregarded, all other effects that are inherent to the serial configuration would lead to the same principal behavior of the transfer function.

In contrast, in the two-stage configuration all wavelength channels experienced the same length of the optical path and encountered the same number of dichroic mirrors. Even though the IL in the violet channel was increased compared to the serial configuration (due to the additional reflection), the IL in the green and red channels corresponded to the values obtained for the three-channel demultiplexer. The lower overall minimum IL of 19.65 dB and better IL uniformity of 2.3 dB of the reassembled two-stage demultiplexer outperformed the serial configuration (26.94 dB and 4.97 dB respectively). Therefore, it can be concluded that

the two-stage configuration is better suited for realization of a four-channel POF demultiplexer than the serial configuration.

The [Jončić13b] demultiplexer outperformed the four-channel solution from [Appelt02] in terms of IL and especially crosstalk. An exceptional performance of that demultiplexer with IL between 3.19 dB and 5.66 dB (overall minimum IL of 16.87 dB) may be explained by a very precise alignment of the components. However, all other measurements (performed two years thereafter) with two, three and four-channel setups, that had to be each time newly aligned, showed somewhat higher IL but also very consistent behavior to one another. Therefore, it cannot be excluded that some other factors such as accumulated dust on the optical surfaces or coating damages due to improper handling could have introduced additional attenuation compared to [Jončić13b] measurement, which was performed with brand new components. In spite of that, all subsequent measurement results, including the IL of 3.85-6.15 dB for the reassembled two-stage demultiplexer, can be considered as excellent achievements.

For the channel count up to four it was demonstrated that SI-POF demultiplexers employing interference filters offer the advantages of good wavelength selectivity, high channel isolation, low IL and flat-top spectral response (that is less sensitive to the spectral shift of transmitters caused by the manufacturing tolerances and temperature changes). The main characteristic of the realized demultiplexer setup compared to the previous solutions was its precise adjustability. That allowed the maximization of the optical throughput in the individual channels. On the other hand, a complex and time-consuming alignment procedure was required. The costly, bulky and alignment sensitive setup was primarily intended for the laboratory applications, and would be difficult to implement in non-laboratory conditions.

The significance of these and of the other previously reported interference filter-based SI-POF demultiplexers is that they enable realization of POF WDM systems and investigation on their data-carrying capacity. For these reasons it is important to further optimize the realized demultiplexer setup and extend the channel count:

- Using achromatic lenses in the input and the output ports, as suggested by [Tschekalinskij10], represent an apparent solution for achieving color correction over a broad spectral range. Alternatively, complex aspherized achromatic lenses could be used to achieve not only color correction but also a small spot size of the focused beam [Edmund13].
- The channel count could be increased up to eight by employing a three-stage configuration where each wavelength channel would encounter three dichroic mirrors. Thereby, the dimensions and the complexity of the demultiplexer setup could be reduced by designing a housing with slits for lenses, dichroic mirrors and interference filters, similar to [Junger02].

4 POF demultiplexer based on a concave diffraction grating

The work presented in this chapter addresses subsequent theoretical and experimental analysis of the concave grating-based SI-POF demultiplexer produced within the VIP HOPE project (see subchapter 2.2.2). Two measurement methods for characterization of transmission properties of the demultiplexer samples were proposed and investigated. The measurement results were interpreted in relation to the theoretical calculations and optical simulations, and were used to qualify the manufacturing process. The results of the analysis were partially presented at the ICPOF 2015 [Jončić15].

4.1 Theoretical calculations on the designed grating

This subchapter calculates the diffraction parameters of the designed concave grating that are referred to throughout the chapter. The physical parameters of the grating are already shown in Table 2.2. For 2.5 μm groove spacing and 0° angle of incidence Table 4.1 gives the angles of diffraction obtained from Equation 2.9 for the first four positive diffraction orders at five lasing wavelengths in the visible spectrum (see also Fig. 4.1). Due to 0° angle of incidence, the diffraction angles in the negative orders have the same values as their positive counterparts but a negative sign. The values of refractive index of PMMA in the visible spectrum and shortening of the corresponding vacuum wavelengths are given in Table 4.2.

Table 4.1: Angles of diffraction $\theta_m(\lambda)$ [$^\circ$] at five lasing wavelengths in the visible spectrum.

Wavelength [nm]	405	450	520	638	660
Diffraction order					
+1	6.18	6.89	8.00	9.87	10.22
+2	12.43	13.89	16.17	20.05	20.78
+3	18.84	21.10	24.69	30.95	32.16
+4	25.50	28.69	33.84	43.29	45.21

Table 4.2: Refractive index of PMMA [Szczurowski13] and shortening of vacuum wavelengths.

Vacuum wavelength [nm]	400	405	450	520	638	660	700
Refractive index of PMMA	1.5059	1.5051	1.4998	1.4941	1.4887	1.4880	1.4869
Wavelength in PMMA [nm]	265.63	269.08	300.05	348.03	428.57	443.56	470.79

From Table 4.1 it can be observed that in the first diffraction order the 405-660 nm wavelength range is free from superposition of light from the second order. However, the same wavelength range in the second order partially overlaps with the third order. The free spectral range $\Delta\lambda_m$ in the first four positive diffraction orders with $\lambda_1=400$ nm as the shortest wavelength is given in Table 4.3. As can be noticed, 400-788.9 nm wavelength range is free from overlap in the first diffraction order. In the second, the third and the fourth order the superposition of light from higher adjacent order starts at 593.8 nm, 529 nm and 496.6 nm respectively. Thereby, Equation 2.10 could be solved only approximately since both λ_2 and $n_{2\text{ PMMA}}$ were unknown. For the wavelength resolution of 0.1 nm the pairs $(\lambda_2, n_{2\text{ PMMA}})$ that best satisfy the ratio $(m+1)\lambda_1/mn_{1\text{ PMMA}}$ were first found. Those pairs are given in the fourth and the fifth column of Table 4.3

Table 4.3: Calculation of the free spectral range.

m	λ_1 [nm]	$(m+1)\lambda_1/mn_{1\text{ PMMA}}$ [nm]	λ_2 [nm]	$n_{2\text{ PMMA}}$	$\Delta\lambda_m$ [nm]
+1	400	531.2438	788.9	1.4849	388.9
+2	400	398.4328	593.8	1.4903	193.8
+3	400	354.1625	529	1.4936	129
+4	400	332.0273	496.6	1.4957	96.6

For the polychromatic light from 400 nm to 700 nm, Fig. 4.1 illustrates the diffraction orders and gives the diffraction angles for the boundary wavelengths.

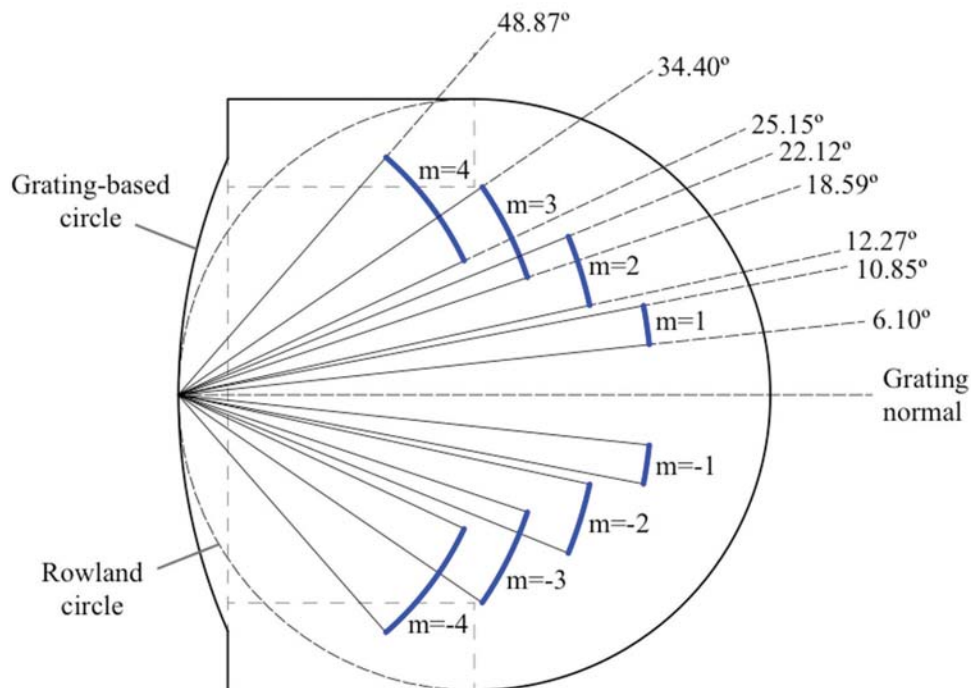


Fig. 4.1: Dispersion of 400-700 nm polychromatic light with angles of diffraction for the boundary wavelengths.

The angular dispersion of the grating is given in Table 4.4. The reciprocal linear dispersion of the grating is given in Table 4.5 for the boundary wavelengths of the intended operating wavelength range.

Table 4.4: Angular dispersion \mathcal{D} [°/nm] of the grating for the boundary wavelengths of the visible spectrum.

Wavelength [nm] \ Diffraction order	400	700
+1	0.0153	0.0157
+2	0.0311	0.0332
+3	0.0482	0.0559
+4	0.0673	0.0936

Table 4.5: Reciprocal linear dispersion \mathcal{P} [nm/mm] of the grating for the boundary wavelengths of the visible spectrum.

Wavelength [nm] \ Diffraction order	400	700
+1	167.32	165.21
+2	83.66	82.61
+3	55.77	55.07
+4	41.83	41.30

4.2 Theoretical considerations on the designed demultiplexer

Comparing the theoretical values for diffraction angles given in Table 4.1 with the results obtained by the ray tracing simulation (OpTaliX) revealed a considerable mismatch between the calculated and the simulated angles. The mismatches in the second and in the third order at 405 nm, 520 nm and 638 nm are illustrated in Fig. 4.2. The theoretical angles are represented in solid lines, whereas the simulation results are represented in dashed lines. The reason for the mismatch is that shortening of wavelengths when light enters PMMA was not taken into account when designing the demultiplexer. Instead, the design vacuum wavelengths were considered to be incident on the grating. The diffraction angles obtained from the grating equation (Equation 2.6) for a grating which has the same parameters and is surrounded by air (or vacuum) fully comply with the ray tracing results, confirming this hypothesis. Therefore, the optimization of the grating parameters for detection in the second diffraction order was based on a false assumption that the design vacuum wavelengths were incident on the grating. In the following, the possibilities for detection in the second and in the third diffraction order are discussed in detail.

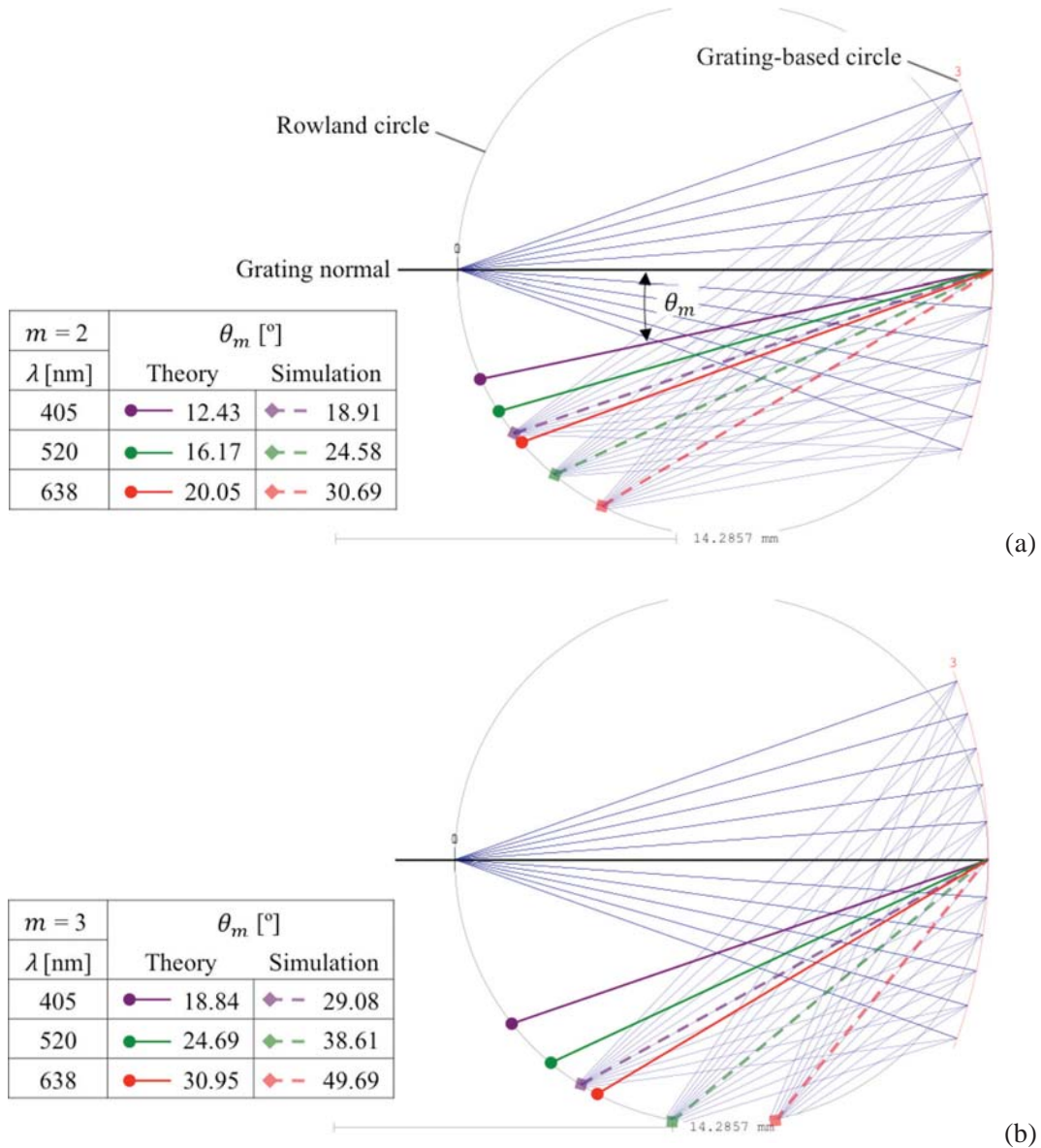


Fig. 4.2: Simulated [Haupt15] and theoretical diffraction angles at 405 nm, 520 nm and 638 nm in (a) the second and (b) the third diffraction order plotted on a 2D ray tracing model of the demultiplexer provided by [Haupt15].

4.2.1 Detection in the second diffraction order

In the second order the angles of diffraction are smaller than expected due to the failure in design. That results in shortening of distances between the wavelengths on the focal curve. The values of the theoretical and simulated diffraction angles at 405 nm, 520 nm and 638 nm, as well as the corresponding focal points on the Rowland circle are shown in Fig. 4.2a.

For 1 mm SI-POF as the output fiber, the minimum wavelength separation between adjacent channels is determined by the reciprocal linear dispersion of the grating. In the second order it equals approx. 83 nm/mm (see Table 4.5). For four fibers densely packed in the detection layer that would, for example, allow to have the channels at 405 nm, 488 nm, 571 nm and 654 nm. Unlike the diodes at 405 nm, 488 nm and around 655 nm, there is no commercial

yellow device at or around 571 nm. Furthermore, to achieve better channel isolation, the fibers should be placed more apart from each other [Bartkiv05]. It would be reasonable to have the channels at 405 nm, 520 nm and around 650 nm, as shown in Fig 4.2a. That would reduce the number of channels in the second order from initially planned four to three.

In addition, the diffraction efficiency of the grating is reduced in the second order for the wavelengths of interest. For 0° angle of incidence the blaze angle was optimized to maximize the diffraction efficiency in the second order within 400-700 nm operating wavelength range. Because of the failure in design, that range refers to the wavelengths in PMMA (λ_{PMMA}). The corresponding range of vacuum wavelengths (λ_{vac}) would be 596.1-1037.3 nm. On the other hand, 400-700 nm λ_{vac} range would be mapped into 265.63-470.79 nm λ_{PMMA} range.

Moving off from the second order blaze wavelength (753.5 nm in vacuum i.e. 507.22 nm in PMMA) would reduce the diffraction efficiency. Such behaviour can also be observed in Fig. 4.3, where the simulated (OpTaliX) theoretical efficiency of the grating employing unpolarized light is shown for the first, the second and the third diffraction order [Haupt15]. The graph in Fig. 4.3 provides two horizontal axes for the simultaneous display of λ_{vac} and λ_{PMMA} . The simulation results show that in the second order the grating could be used with red and near infrared λ_{vac} (600-1050 nm). Within 400-550 nm λ_{vac} range the efficiency would be less than 5%, making those wavelength unsuitable for use in the second order.

Finally, the imaging aberrations of the grating, in particular the astigmatism, are larger in the second diffraction order for the wavelengths of interest. Two spot diagrams for the second order are combined together in Fig. 4.4 to illustrate the rise of imaging aberrations. The diagram on the left [Haupt15] (in lighter colours) was obtained with the design wavelengths that refer to PMMA. The diagram on the right [Haupt15] was obtained with the correct set of

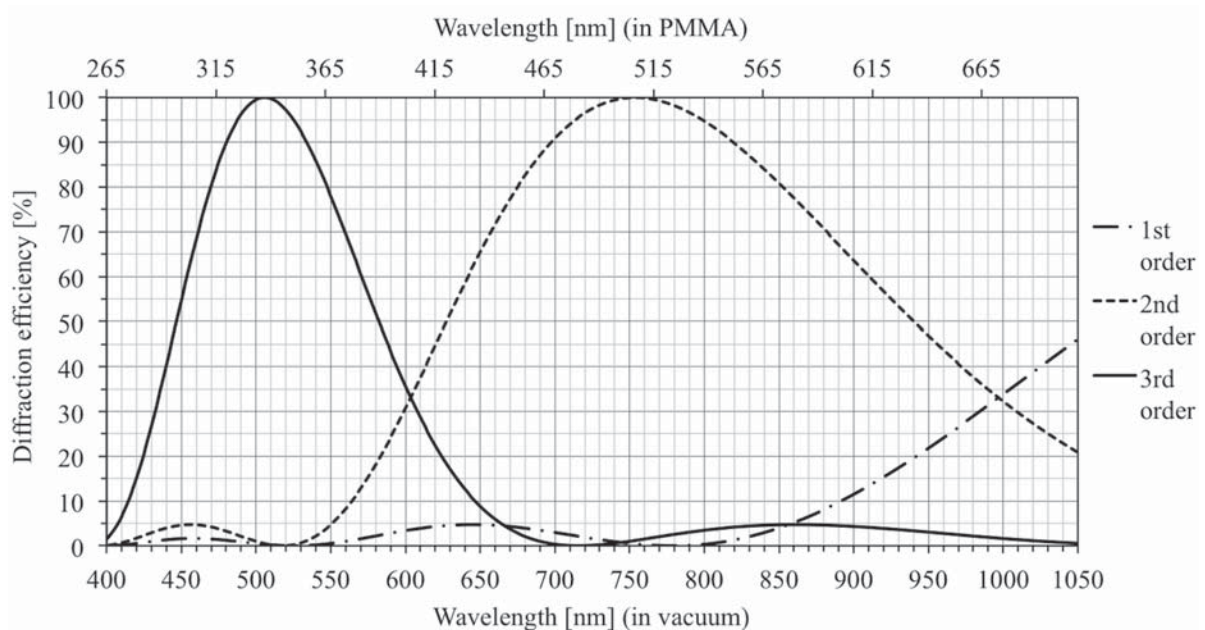


Fig. 4.3: Theoretical diffraction efficiency of the grating for the first, the second and the third diffraction order [Haupt15].

λ_{vac} . The images would experience the same behaviour if a point source was replaced with an area source corresponding to 1 mm SI-POF [Haupt12]. The larger the separation from the wavelength where the astigmatism is minimized, the image height would increase and the image width would decrease, reducing the amount of light coupled into the output fiber.

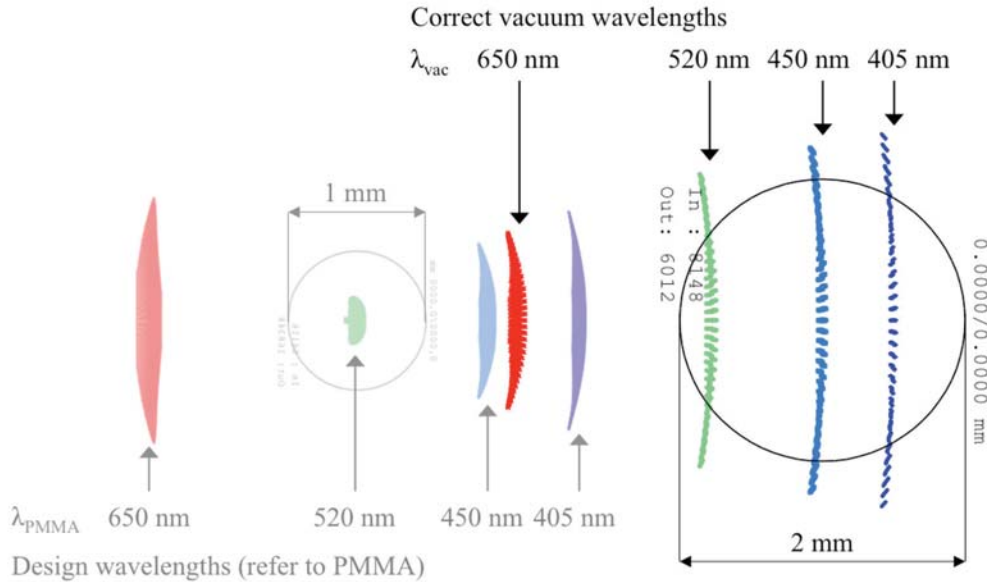


Fig. 4.4: Two spot diagrams for the second diffraction order combined together to illustrate the rise of imaging aberrations (note: diameters of the reference circles were set within the ray tracing software).

To conclude, in the second order the grating provides good diffraction efficiency and low aberrations within 600-1050 nm λ_{vac} range. Within that range the demultiplexing of four wavelength channels would be possible with sufficient separation between 1 mm output fibers. Within λ_{vac} range that is used for SI-POF communication (400-700 nm) it would be possible to use three detecting fibers in the second diffraction order. However, the reduced diffraction efficiency and increased imaging aberrations for $\lambda_{vac} < 600$ nm make the second order unsuitable for SI-POF applications.

4.2.2 Detection in the third diffraction order

From Fig. 4.2a and Fig. 4.2b it can be noticed that the simulated diffraction angles in the second order, corresponding to the grating surrounded by air (or vacuum), have similar values as the theoretical diffraction angles in the third order. That is due to the fact that in Equation 2.8 the ratio m/n_{PMMA} approximately equals 2 for $m=3$, influencing the equation in the same way as if the grating was in the air for $m=2$. Therefore, the third diffraction order offers almost the same reciprocal linear dispersion i.e. provides the same separation between the wavelengths on the focal curve as it was initially planned for the second order.

In addition, the diffraction efficiency in the third order rises as the wavelength decreases with respect to the second order blaze wavelength. Using equation:

$$m\lambda_{Bm\ PMMA} = 2d \sin \theta_B \cos(\theta_i - \theta_B), \quad (4.1)$$

where θ_B is the blaze angle, the third order PMMA blaze wavelength $\lambda_{B3\ PMMA}$ is obtained to be 338.15 nm and the corresponding vacuum wavelength $\lambda_{B3\ vac}$ is 505.6 nm. The identical result can be observed from Fig. 4.3 with the diffraction efficiency of 100% at $\lambda_{vac}=505.6$ nm. However, because of higher angular dispersion (see Table 4.4), the efficiency curve has a steeper fall-off than in the second order. That reduces the operating wavelength range in the third order. For example, in the second order the grating was designed to provide the efficiency greater than 23% within 400-700 nm λ_{PMMA} range. In the third order the efficiency is above that value within 427-620 nm λ_{vac} range.

Finally, for a given angle of incidence the wavelengths from different orders diffracted at the same angle experience the same imaging aberrations [Loewen97]. As shown in Fig. 4.4, in the second order 520 nm λ_{PMMA} experiences the lowest aberrations. In the third order 520 nm λ_{vac} is diffracted at approximately the same angle as 520 nm λ_{PMMA} in the second order, also experiencing the lowest aberrations. Correspondingly, 405 nm, 450 nm and 650 nm λ_{vac} in the third order experience almost the same aberrations as 405 nm, 450 nm and 650 nm λ_{PMMA} in the second order. Therefore, in the third diffraction order the imaging properties of the grating are optimized for 400-700 nm λ_{vac} operating wavelength range.

Due to the fact that wavelength shortening in PMMA by a factor of approx. 1.5 and the ratio of the third and the second diffraction order of $3/2=1.5$ cancel each other, the performances of the grating in the third order satisfy the conditions for wavelength separation and aberrations initially set for the second order. The biggest constrain for the implementation of the demultiplexer in the third order would be shortening of λ_{vac} operating wavelength range to 427-620 nm because of reduced diffraction efficiency. Having the minimum channel separation of 55 nm (see Table 4.5), and according to Fig. 4.3 the violet and red lasers unsuitable for use, the available channels left would be those at 450 nm and 520 nm. These two wavelengths fall within the free spectral range of 129 nm in the third order (see Table 4.3). Consequently, there would be no overlap with the images from the second and the fourth order (as shown in Fig. 4.1), even when the input fiber had 1 mm diameter.

4.3 Description of demultiplexer samples

Within the project VIP HOPE four demultiplexer samples were produced. In the following, those samples are numbered with S1, S2, S3 and S4, based on the chronology of their production. The first produced was the Sample S1. It is introduced in Fig. 4.5. The body of the demultiplexer lies between the Rowland circle-based half-sphere on the front side and the toroidal grating on the back side of the device. The labels plus (+) and minus (-) added to a CAD model in Fig. 4.5a indicate from which demultiplexer side are the positive and the negative orders respectively. An intersection between the back side of the demultiplexer body and the toroidal surface forms an elliptical cross section with 16 mm width and 15.17 mm

height, as shown in Fig. 4.5b. The Sample S1 mounted in a holder is shown in Fig. 4.5c. To demonstrate the wavelength separating function, the sample was excited over an input SI-POF with white light of low intensity. The input fiber was fixed to the demultiplexer using an UV-curable adhesive with the refractive index close to the one of PMMA. The images of the segments from the upper and the lower half of the toroidal surface, obtained by a scanning electron microscope, are shown in Fig. 4.5d and Fig. 4.5e respectively [HOPE14b]. The sawtooth profile can be recognized in the upper half of the toroidal surface. However, in the lower half of the toroidal surface the quality of the grating deteriorates. According to [Höll14] that is because of the change in how the ruling engine applies the force on the surface – once the diamond tool reaches the highest point on the toroidal surface its motion changes from pulling to pushing, leading to a poor grating structure in the lower half of the surface.

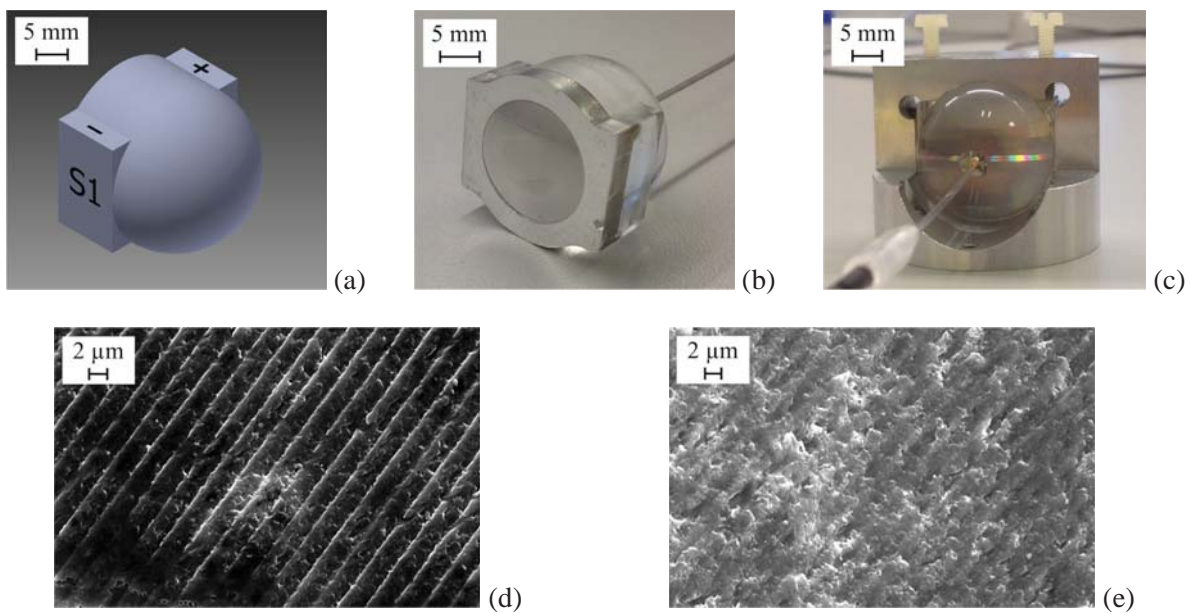


Fig. 4.5: Demultiplexer Sample S1: (a) CAD model; (b) back side with the grating; (c) sample mounted in a holder; (d) recognizable sawtooth profile in the upper half of the toroidal surface [HOPE14b]; (e) poor grating structure in the lower half of the toroidal surface [HOPE14b].

The Sample S2 offered better quality of the grating. Fig. 4.6a shows a segment from the upper half of the toroidal surface with a good grating structure. A segment from the lower half of the surface, shown in Fig. 4.6b, experiences coarse but still recognizable groove pattern.

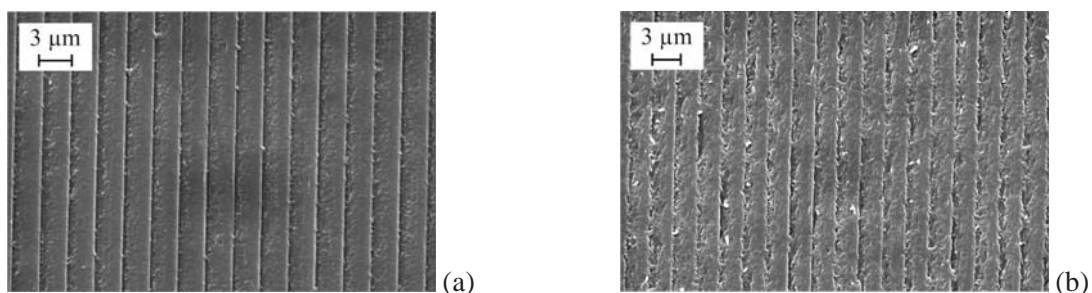


Fig. 4.6: Demultiplexer Sample S2: (a) good grating structure in the upper half of the toroidal surface [Höll14]; (b) coarse grating structure in the lower half of the toroidal surface [Höll14].

The grating segments of the sample S3 are shown in Fig. 4.7. Again, the difference in the quality of the grating surface when the diamond tool is pulled or pushed to form the grooves is clearly observable.

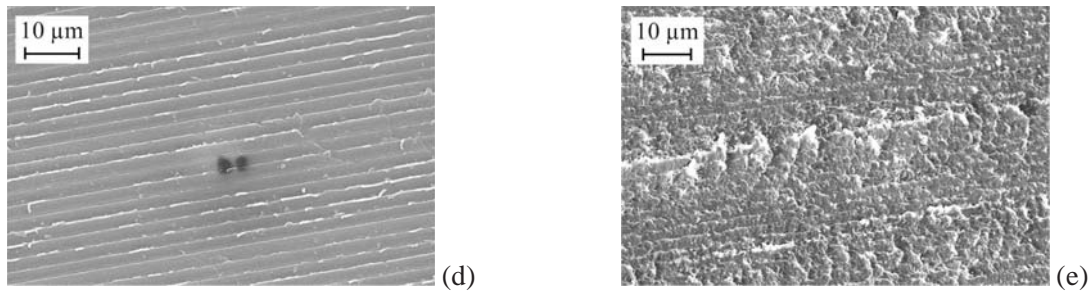


Fig. 4.7: Demultiplexer Sample S3: (a) recognizable sawtooth profile in the upper half of the toroidal surface [HOPE14a]; (b) poor grating structure in the lower half of the toroidal surface [HOPE14a].

The Sample S4 is introduced in Fig. 4.8. Like the Sample S3, it was redesigned to offer easier mounting possibilities due to a larger demultiplexer body, and more precise alignment of the input fiber due to an alignment guide at the top of the Rowland circle-based half sphere. The changes in design can be seen in Fig. 4.8a. In spite of different attempts to improve the ruling process, the Sample S4 had the poorest grating quality among all manufactured samples, as can be observed from Fig. 4.8d and Fig. 4.8e.

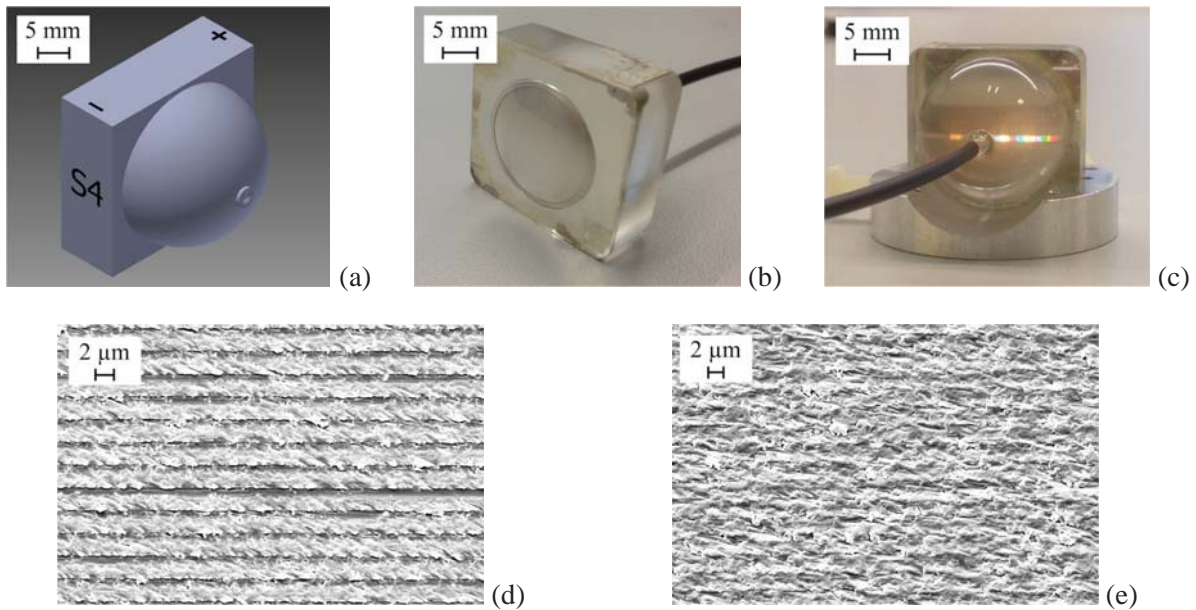


Fig. 4.8: Demultiplexer Sample S4: (a) CAD model; (b) back side with the grating; (c) sample mounted in a holder; (d) coarse sawtooth profile recognizable in the upper half of the toroidal surface [HOPE14b]; (e) poor grating structure in the lower half of the toroidal surface [HOPE14b].

Based on a limited number of grating segments obtained with the scanning electron microscope, it can be stated that the Sample S2 offered the best grating quality. It was followed by the Samples S1 and S3. The Sample S4 had the poorest grating structure.

4.4 Measurement methods

The characterization of transmission properties of the demultiplexer was performed by scanning its curved focal surface with 1 mm output SI-POF. Two measurement methods, which differ in the orientation of the scanning output fiber with respect to the grating center, and the corresponding mounting setups were proposed and investigated. For ease of understanding, the simplified measurement method, that had to be developed as an alternative to the initially developed more complex method, is introduced first.

4.4.1 Simplified measurement method

The principle of the simplified measurement method is illustrated in Fig. 4.9. The ideal position of the output fiber for the angle of diffraction θ_m , with the fiber axis going through the center of the grating, is shown in dashed lines. However, in the current demultiplexer design that position could not be physically reached. Instead, the method is based on a simplified approach where the output fiber is always perpendicular to the demultiplexer surface regardless of the angle of diffraction. The center of the output fiber touches the surface of the demultiplexer at the same point as the center of the ideally positioned fiber would do. The output fiber axis goes through the center of the Rowland circle with the radius r and forms the angle $2\theta_m$ with the grating normal. The scan of the demultiplexer surface over a range of diffraction angles is performed by rotating the demultiplexer and the input fiber counterclockwise around the center of the Rowland circle.

As indicated in Fig. 4.9, positioning the output fiber perpendicular to the demultiplexer surface introduces an angular displacement between the actual and the ideal axis of the fiber. For a given angle of diffraction θ_m the angular displacement also equals θ_m . Therefore, compared to the ideal fiber position when the space between the demultiplexer surface and the

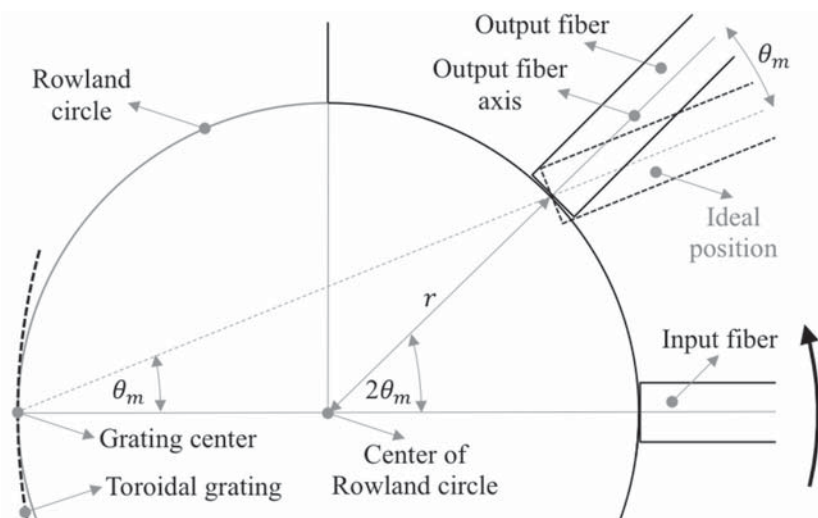


Fig. 4.9: Principle of the simplified measurement method. The output fiber stays in the fixed position perpendicular to the demultiplexer surface. To perform the scan, the input fiber and the demultiplexer are rotated counterclockwise around the center of the Rowland circle.

output fiber would be filled with index-matching adhesive or gel, the measurement results contained additional losses due to angular misalignment and Fresnel reflection.

The coupling loss between the image of the input fiber and the output fiber was approximated by the loss due to angular misalignment between two identical multimode step-index fibers with uniform mode distribution. The calculation of the loss was performed using Equation 2.18. The resulting Fresnel loss in the image layer was taken to be 0.35 dB according to Equation 2.13. It was assumed that no Fresnel reflections occur when the light transits from the input fiber into the demultiplexer due to the UV-curable adhesive filling the air gap. The correction factor comprising the loss due to angular misalignment and the Fresnel loss is represented by a solid line in Fig. 4.10.

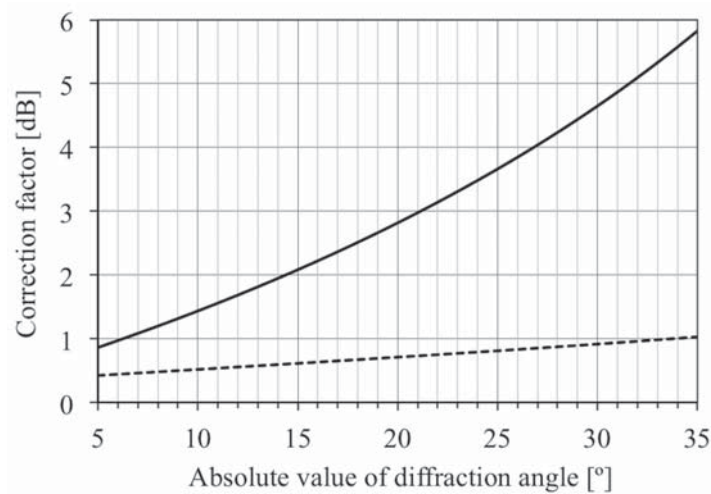


Fig. 4.10: Correction factor for the simplified method (due to angular misalignment and Fresnel reflection) – solid line (—); correction factor for the initially developed complex method (due to longitudinal misalignment and Fresnel reflection) – dashed line (---).

It is known that the theoretical models assuming a uniform mode distribution, as in Equation 2.15-18, typically overestimate the actual coupling losses due to misalignments [Ziemann08]. Therefore, adding the correction factor to the measured optical level would indicate the theoretical upper limit of the demultiplexer performance. The optical level that would be detected with an ideally positioned fiber would rather lie below the corrected level. For example, let the optical level detected by the output fiber at a certain wavelength and diffraction angle be -20 dBm. Furthermore, let the corresponding correction factor be 2 dB. Then, the actual optical level that would be detected with an ideally positioned output fiber would not be -18 dBm, but rather slightly below that value (for an illustration see Fig. 4.22b).

The mounting of the demultiplexer Sample S4 is shown in Fig. 4.11. The Sample S4 (2) with the input fiber (1) was installed on a rotation stage M-RS40 (4) over an appropriate holder (3) so that the rotational axis of the stage went through the center of the Rowland circle. The rotation stage allows the angular position readout to 0.2° from the vernier scale, but also has a micrometer screw allowing for the finer resolution. It was fixed to a stationary bracket (6) of F-206 hexapod over a mounting plate (5). The F-206 hexapod system is a high-precision

automated fiber optic alignment system allowing the minimum incremental translational motion of $0.1 \mu\text{m}$. The output fiber (11) was centered within a fiber chuck (10), which was mounted to a movable platform (7) of the hexapod over a cable clamp (9) and a movable platform adapter (8). The complete setup was installed on a vibration suppressing optical table.

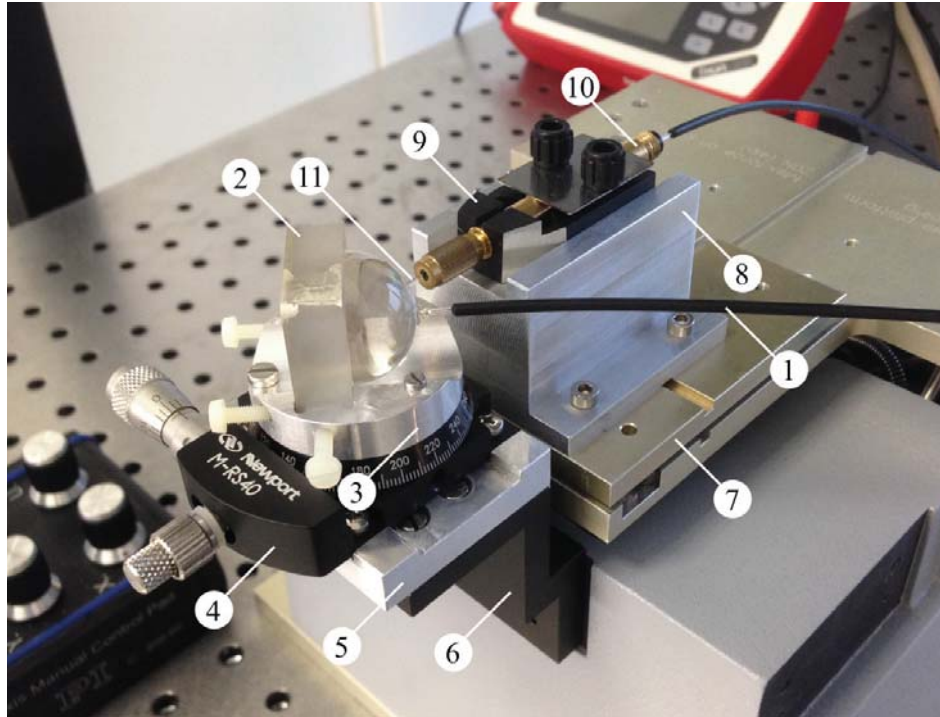


Fig. 4.11: Mounting of the demultiplexer Sample S4 for the simplified measurement method: 1 – input fiber; 2 – demultiplexer Sample S4; 3 – holder for demultiplexer sample S4; 4 – M-RS40 rotation stage; 5 – rotation stage mounting plate; 6 – bracket of F-206 hexapod system for affixing stationary components; 7 – movable platform of F-206 hexapod system; 8 – movable platform adapter; 9 – cable clamp; 10 – fiber chuck; 11 – output fiber.

The alignment between the demultiplexer and the output fiber was performed in the following manner. After all components were mounted on F-206 hexapod, the rotation stage was used to position the demultiplexer as if the input fiber entered Fig. 4.12 from the bottom side, such that the angle between the input and the output fiber was 90° . Instead of the output fiber and the fiber chuck, a centering rod sharpened on top was mounted in the cable clamp. The top of the rod was aligned with the front edge of the demultiplexer body using the incremental translational motion of $10 \mu\text{m}$. That had to provide that the rod axis intersects the rotational axis of M-RS40 stage. The alignment process was monitored under a Stemi 2000 stereo microscope. After the alignment was performed, the rod was taken out and the output fiber and the chuck were mounted back in the clamp. The angle between the input and the output fiber was then reduced so that the end face of the output fiber could be brought to the surface of the demultiplexer (as shown in Fig. 4.12). The incremental translational motion used for that and all other positioning was $10 \mu\text{m}$, primarily because of the multiple larger SI-POF diameter, but also because of the limited magnification of the microscope. In addition, the

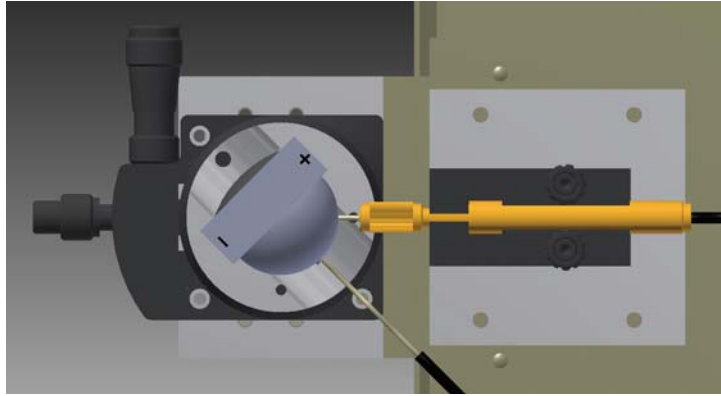


Fig. 4.12: Positioning of the demultiplexer Sample S4 and of the output fiber for the simplified measurement method at the diffraction angle of 22.5° .

vertical alignment took place. The laser radiation was introduced through the input fiber, and the output fiber was vertically aligned so that maximum optical power could be detected at its output with an optical power meter. To verify the vertical alignment, the same procedure was performed for several diffraction angles. After this final adjustment step, the demultiplexer was brought into initial angular position corresponding to the diffraction angle of 30° or 35° , and the setup was ready to start the scan. For the purpose of aligning and fixing the input fiber to the demultiplexer, a specialized mounting on the movable platform of F-206 hexapod was used.

4.4.2 Initially developed measurement method

The principle of the initially developed more complex measurement method is illustrated in Fig. 4.13. The ideal position of the output fiber for the angle of diffraction θ_m , with the center of the fiber located on the Rowland circle and the fiber axis going through the center of the grating, is shown in dashed lines. In this method the scanning output fiber always preserves the ideal orientation with respect to the grating center. With respect to the ideal end face position, the fiber is shifted backwards along the ideal fiber axis and kept as close as possible to the demultiplexer surface. Assuming the uppermost position of the output fiber in Fig. 4.13 as the initial position, the scanning is performed by clockwise rotation and then translation of the output fiber to the position corresponding to the new diffraction angle. The demultiplexer and the input fiber stay in a fixed position during the scan. Such functionality was achieved by mounting the output fiber over the rotation stage on the movable platform of F-206 hexapod, while the demultiplexer was affixed to its stationary bracket. That can be observed from Fig. 4.16. A detailed description of the mounting setup follows on the next pages.

To perform the scan, it was essential to determine the input coordinates of F-206 hexapod system that ensured correct positioning of the output fiber with respect to the surface of the demultiplexer and the center of the grating. In the first step, it was necessary to calculate the diffraction angle-dependent backward shift of the output fiber with respect to its ideal

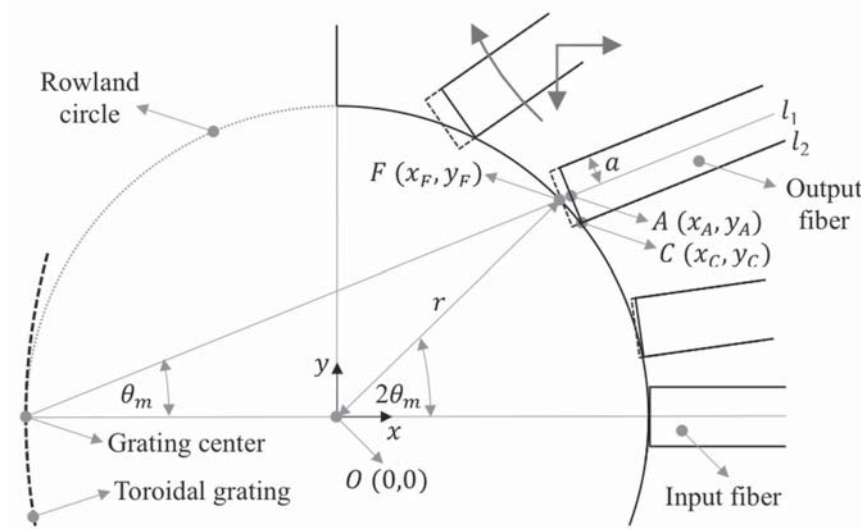


Fig. 4.13: Principle of the initially developed measurement method. The output fiber is rotated and then translated closest possible to the demultiplexer surface so that its axis goes through the center of the grating. The input fiber and the demultiplexer stay in the fixed position.

position. For that purpose, the key points and their coordinates in Fig. 4.13 are denoted as follows:

- $O(0,0)$ – origin of the Cartesian coordinate system xOy positioned in the center of the Rowland circle;
- $F(x_F, y_F)$ – focal point on the Rowland circle i.e. demultiplexer surface where the center of the ideally positioned output fiber is located;
- $C(x_C, y_C)$ – contact point between the output fiber and the demultiplexer surface;
- $A(x_A, y_A)$ – actual position of the center of the output fiber.

Let l_1 be a line representing the axis of the output fiber. For the angle of diffraction θ_m the equation of l_1 is given by:

$$y = x \tan \theta_m + r \tan \theta_m. \quad (4.2)$$

To work with the general numbers, the cladding radius of the output fiber is designated as a . In practical calculations a value of $500 \mu\text{m}$ was used. The equation of a line l_2 , which is parallel to and at a distance a from the line l_1 , is therefore:

$$y = x \tan \theta_m + r \tan \theta_m - a / \cos \theta_m. \quad (4.3)$$

In the first quadrant the line l_2 intersects the Rowland circle at a point C . The ordered pair (x_C, y_C) is of a form:

$$x_C = -r \sin^2 \theta_m + a \sin \theta_m + \sqrt{p} \cos \theta_m \quad (4.4)$$

$$y_C = r \sin \theta_m \cos \theta_m - a \cos \theta_m + \sqrt{p} \sin \theta_m \quad (4.5)$$

with

$$p = r^2 \cos^2 \theta_m + 2ar \sin \theta_m - a^2. \quad (4.6)$$

Knowing the ordered pairs $(x_F, y_F) = (r \cos \theta_m, r \sin \theta_m)$ and (x_C, y_C) , the distance \overline{FC} can be easily calculated. The backward shift Δ of the output fiber along the fiber axis for a given diffraction angle is therefore:

$$\Delta = \overline{FA} = \left| \sqrt{\overline{FC}^2 - a^2} \right| = \sqrt{p} - r \cos \theta_m. \quad (4.7)$$

For example, the backward shift at the diffraction angle of 10° equals $77 \mu\text{m}$. At the angle of 35° the shift rises to $331 \mu\text{m}$. The resulting coupling loss due to the backward shift of the output fiber was approximated by the loss due to longitudinal misalignment between two identical multimode step-index fibers with uniform mode distribution. The calculation of the loss was performed using Equation 2.17. The resulting Fresnel loss in the image layer was taken to be 0.35 dB according to Equation 2.13. It was assumed that no Fresnel reflections occur when the light transits from the input fiber into the demultiplexer due to the UV-curable adhesive filling the air gap. The correction factor comprising the loss due to longitudinal misalignment and the Fresnel loss is shown by a dashed line in Fig. 4.10. Like in the simplified measurement method, adding the correction factor to the measured optical level would indicate the theoretical upper limit of the demultiplexer performance. The actual optical level that would be detected with an ideally positioned fiber would rather lie slightly below the corrected level.

Knowing Δ , the coordinates of the center of the scanning output fiber can be calculated as:

$$x_A = x_F + \Delta \cos \theta_m = r \cos 2\theta_m + \Delta \cos \theta_m \quad (4.8)$$

$$y_A = y_F + \Delta \sin \theta_m = r \sin 2\theta_m + \Delta \sin \theta_m. \quad (4.9)$$

The position of the scanning output fiber when the movable platform of F-206 hexapod is in its initial position is shown in Fig. 4.14. The center of the fiber is located in the origin $O'(0,0)$ of the $x'O'y'$ Cartesian coordinate system in which the coordinates of the hexapod are expressed. The coordinates of the fiber center with respect to (w.r.t.) xOy are designated with x_I and y_I . The setup from Fig. 4.16 is realized so that when F-206 hexapod is in its initial position, the axis of the output fiber (coinciding with the x' -axis) and the grating normal (coinciding with the x -axis) form an angle of 45° .

For further calculations it is necessary that the coordinates of a point expressed w.r.t. the coordinate system xOy are expressed w.r.t. the coordinate system $x'O'y'$ and vice versa. To achieve that, the active transformation, which maps the origin O into O' , and the x - and y -axis into the x' - and y' -axis respectively, must be found first. This transformation is a composition of a counterclockwise rotation by $\pi/4$ about the origin O and a translation by the vector $(x_I \ y_I)^T$. The inverse of the active transformation matrix is a matrix P , which is the required passive transformation matrix:



$$P = \begin{pmatrix} \cos \pi/4 & \sin \pi/4 & -x_I \cos \pi/4 - y_I \sin \pi/4 \\ -\sin \pi/4 & \cos \pi/4 & x_I \sin \pi/4 - y_I \cos \pi/4 \\ 0 & 0 & 1 \end{pmatrix}. \quad (4.10)$$

For example, let an arbitrary point M have the coordinates (x_M, y_M) w.r.t. the coordinate system xOy . The coordinates of the point M w.r.t. $x'O'y'$, x'_M and y'_M , can be obtained as:

$$\begin{pmatrix} x'_M \\ y'_M \\ 1 \end{pmatrix} = P \begin{pmatrix} x_M \\ y_M \\ 1 \end{pmatrix}. \quad (4.11)$$

To establish the connection between the xOy and $x'O'y'$ coordinate systems, the coordinates of a point $I(x_I, y_I)$, which are initially unknown, have to be determined. To do that, the output fiber must be translated into position 1a, as shown in Fig. 4.14. The coordinates of the fiber center w.r.t. xOy can be calculated as $x_R = a \cos \pi/4$ and $y_R = r + a \sin \pi/4$. The coordinates of the same point w.r.t. $x'O'y'$, x'_R and y'_R , represent the travel of the movable platform of F-206 hexapod along the x' - and y' -axis respectively, and can be directly read from the display of the hexapod system. Substituting the coordinates of the point R w.r.t. both coordinate systems in Equation 4.11 and solving the system of two equations with x_I and y_I as unknowns yields:

$$x_I = x_R - x'_R \cos \pi/4 + y'_R \sin \pi/4 \quad (4.12)$$

$$y_I = y_R - x'_R \sin \pi/4 - y'_R \cos \pi/4. \quad (4.13)$$

To bring the output fiber into position corresponding to an arbitrary angle of diffraction θ_m (position 2 in Fig. 4.14), it would first have to be rotated from position 1a by the angle of $\pi/4 - \theta_m$ into position 1b. The point of rotation, which lays on the rotational axis of the

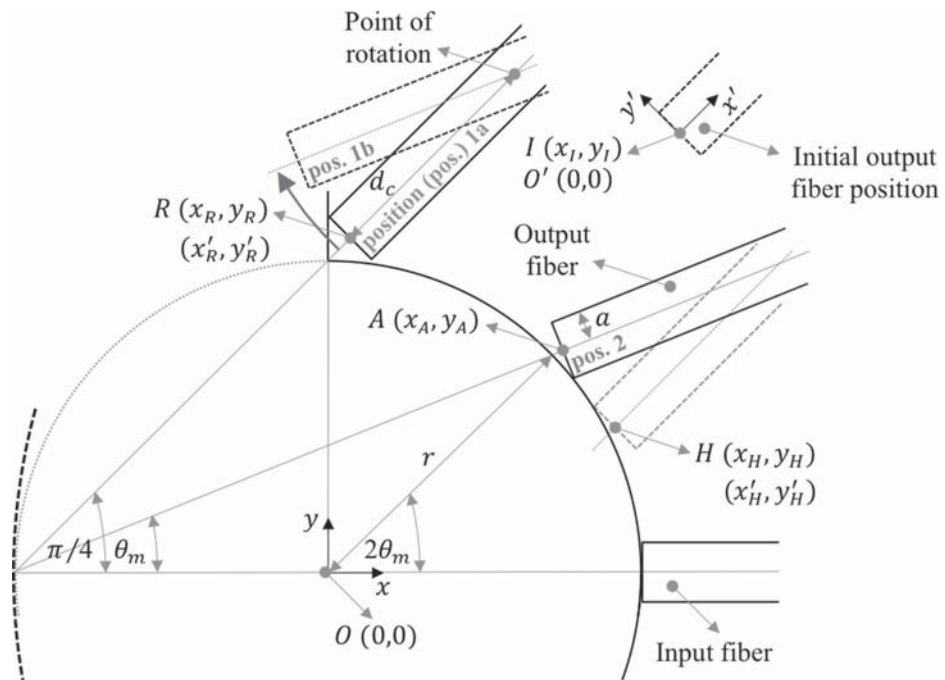


Fig. 4.14: Determining the input coordinates of F-206 hexapod system.

rotation stage, is at the distance d_c from the center of the output fiber. Since the rotation stage is mounted on the movable platform, the rotation of the fiber is independent from its translation, and the positioning coordinates of the hexapod system are still x'_R and y'_R . To bring the output fiber from position 1b into position 2, the coordinates of the hexapod would have to be changed to x'_H and y'_H , which corresponds to a point H in Fig. 4.14.

Using the basic principles of trigonometry, it can be shown that the distance \overline{AH} equals:

$$\overline{AH} = 2d_c \sin(\pi/8 - \theta_m/2), \quad (4.14)$$

and that the coordinates of the point H w.r.t. the coordinate system xOy , expressed as a function of x_A and y_A , are:

$$x_H = x_A + 2d_c \sin(\pi/8 - \theta_m/2) \cos(3\pi/8 - \theta_m/4) \quad (4.15)$$

$$y_H = y_A - 2d_c \sin(\pi/8 - \theta_m/4) \sin(3\pi/8 - \theta_m/4). \quad (4.16)$$

After applying the transformation matrix P , the coordinates of the point H w.r.t. the coordinate system $x'O'y'$, can be calculated as:

$$x'_H = (x_H - x_I) \cos \pi/4 + (y_H - y_I) \sin \pi/4 \quad (4.17)$$

$$y'_H = -(x_H - x_I) \sin \pi/4 + (y_H - y_I) \cos \pi/4. \quad (4.18)$$

The obtained ordered pairs (x'_H, y'_H) represent the input coordinates of the hexapod system that ensure correct positioning of the output fiber with respect to the surface of the demultiplexer and the center of the grating. Besides the cladding radius of the output fiber a and the radius of the Rowland circle r , which are predetermined constants, the input of the mathematical model which calculates the diffraction angle-dependent ordered pairs (x'_H, y'_H) are also the ordered pair (x'_R, y'_R) and the distance d_c .

The relative change of the x' - and the y' -axis coordinates of F-206 hexapod system w.r.t. the point R (x'_R, y'_R) for diffraction angles from 45° to 0° is shown in Fig. 4.15. The distance d_c is

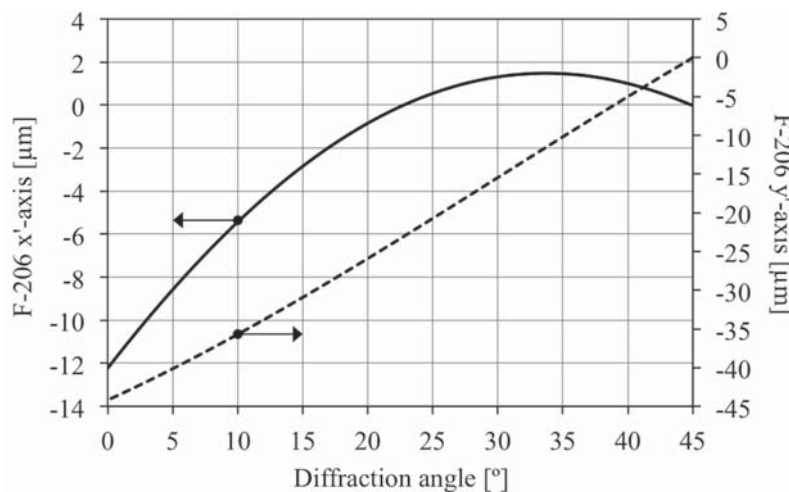


Fig. 4.15: Relative change of the x' and y' -axis coordinates of F-206 hexapod system w.r.t. the point R (x'_R, y'_R) for $d_c=40$ mm.

set to 40 mm, which is a value suitable for practical realization of the mounting setup. For example, to go into position corresponding to the diffraction angle of 10° , the travel of -5.43 mm and -35.69 mm has to be performed along the x' - and the y' -axis respectively. However, the travel range of the hexapod system is from -8 mm to 5.7 mm along the x' -axis, and from -5.7 mm to 5.7 mm along the y' -axis. Consequently, to reach the positions corresponding to lower diffraction angles, the use of an external translation stage is required.

The mounting of the demultiplexer Sample S2 for the scan over positive diffraction angles is shown in Fig. 4.16. The Sample S2 (2) with the input fiber (1) had to be mounted on an uppermost TB 50-16 linear translation stage (5) over a holder (3) and an appropriate adapter (4) such that the grating normal formed an angle of 45° with the x' -axis (as shown in Fig. 4.17). The translation stage has a resolution of 10 μm and allows 16 mm travel along a single axis. Three translation stages (one for x' - and two for y' -direction) were mounted on the top of each other to extend the measurement range and to allow flexible initial positioning of the demultiplexer. For affixing the lowermost translation stage to the stationary bracket (8) of F-206 hexapod, two mounting plates (6,7) were used. The output fiber (15) was centered within a fiber chuck (14), which had to be mounted on the M-RS40 rotation stage (11) over a cable clamp (13) and a rotation stage adapter (12) such that the rotational axis of the stage intersected the axis of the output fiber. The rotation stage was fixed to the movable platform (9) of the hexapod (9) over an appropriate adapter (10).

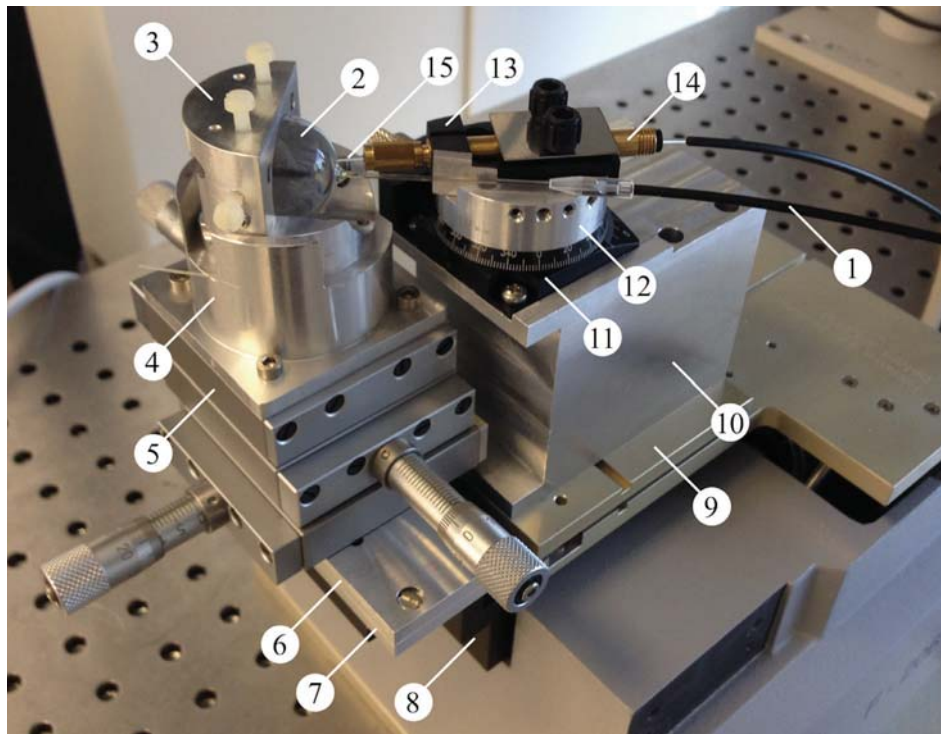


Fig. 4.16: Mounting of the demultiplexer Sample S2 for the initially developed measurement method: 1 – input fiber; 2 – demultiplexer Sample S2; 3 – holder for demultiplexer Sample S2; 4 – translation stage adapter; 5 – liner translation stage; 6 – top mounting plate; 7 – bottom mounting plate; 8 – bracket of F-206 hexapod system for affixing stationary components; 9 – movable platform of F-206 hexapod system; 10 – movable platform adapter; 11 – M-RS40 rotation stage; 12 – rotation stage adapter; 13 – cable clamp; 14 – fiber chuck; 15 – output fiber.



The alignment between the demultiplexer and the output fiber was performed in the following manner. At first, the hexapod system was initialized and the centering rod sharpened on top was mounted in the cable clamp. Under the microscope and by using the incremental translational motion of $10\ \mu\text{m}$ the horizontal and vertical alignment of the rod was carried out. The top of the rod had to point at the transition between the Rowland circle-based half sphere and the demultiplexer body in the dispersion plane, as shown in Fig. 4.17 for the Sample S4. That had to ensure that the axis of the rod went through the grating center and formed an angle of 45° with the grating normal.

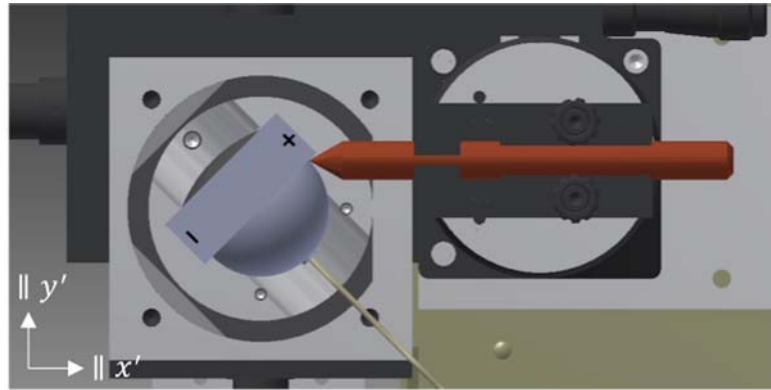


Fig. 4.17: Alignment of the centering rod. The axes parallel to x' - and y' -axis are also designated.

The rod was then taken out and the output fiber centred within the chuck was mounted in the clamp, such that the distance between the fiber center and the rotational axis of the M-RS40 stage was approx. 40 mm. By translation only along the x' -axis the output fiber had to be brought to the position corresponding to position 1a from Fig. 4.14. The x'_R and y'_R coordinates were then directly read from the display of the hexapod system. Together with the cladding radius of the output fiber a , radius of the Rowland circle r and distance d_c , those coordinates were used as the input of the mathematical model for calculating the ordered pairs (x'_H, y'_H) .

The rotational direction of the output fiber during the scan as well as its translational directions parallel to x' - and y' -axes are illustrated in Fig. 4.18 with black arrows. From Fig. 4.15 it can be observed that the y' -coordinate decreases much faster than the x' -coordinate as the diffraction angle decreases. Consequently, during the scan the hexapod system first reached its travel limit on the y' -axis (see Fig. 4.18, step 1). Once that happened, one of the translation stages was used to push the demultiplexer in the positive direction along the axis parallel to the y' -axis (step 2). To place the output fiber in the same position with respect to the demultiplexer as before it was pushed, the hexapod system had to travel the same distance along the y' -axis in the positive direction (step 3). The hexapod was then again within its allowed travel range, and the scan could be continued for the lower diffraction angles (step 4).

Before the actual scan could start, the described procedure was used to accurately determine the distance d_c , since it could not be exactly measured. Namely, the ordered pairs (x'_H, y'_H)

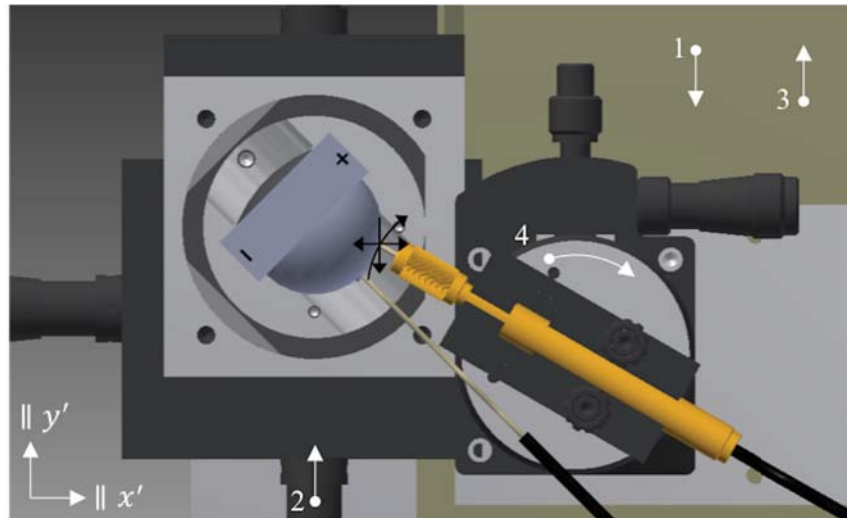


Fig. 4.18: Positioning of the demultiplexer Sample S4 and of the output fiber for the initially developed measurement method at the diffraction angle of 15° .

were first determined with an approximate value of d_c which was taken to be slightly smaller than it actually was. The demultiplexer and the output fiber were brought into position corresponding to some of the lower angles of diffraction, e.g. 15° . Because of the smaller distance d_c , the output fiber did not touch the demultiplexer. In the iterative process, the ordered pair (x'_H, y'_H) corresponding to the diffraction angle of 15° had to be recalculated for increasing values of d_c until the fiber touched the demultiplexer, as illustrated in Fig. 4.18. After this final adjustment step, the output fiber and the demultiplexer had to be brought to the position corresponding to the diffraction angle of 30° or 35° , and the setup would be ready to start the scan. The additional vertical alignment would not be necessary since it was already performed with the centering rod.

The described measurement method was first developed because it locates the scanning output fiber most closely to its ideal position, which primarily refers to the ideal orientation of the fiber with respect to the grating center. That had to ensure that the measurement results most closely correspond to the actual values. On the other hand, that implied an alignment sensitive mounting setup. To prevent the error propagation and thus the uncertainty (both angular and translational) of the output fiber position during the scan, the (x'_R, y'_R) input to the mathematical model had to be most exactly determined. Furthermore, the initial alignment of the components shown in Fig. 4.17 had to be most precise. However, the realized mounting of the demultiplexer samples, conditioned by the available mechanical components, lead to a bulky design subject to misalignments and imprecisions. During the test scans, the propagation of accumulated errors combined with an inaccurate distance d_c introduced deviations of the output fiber from the desired position that could not be resolved, thus making any measurement attempt unreliable.

For those reasons, the simplified measurement method was subsequently developed. As shown in Fig. 4.10, the method requires larger correction factor, thus introducing more uncertainty into the measurement results. However, it is less alignment-sensitive and therefore

more suitable for practical realization. The results represented in the next subsection were obtained with the simplified method.

The initially developed method requires smaller correction factor, thus introducing less uncertainty into the measurement results compared to the simplified method. For example, for the diffraction angle of 20° the respective correction factors are 2.8 dB and 0.7 dB. As can be observed from Fig. 4.10, the difference becomes even more significant for higher diffraction angles ($> 20^\circ$). Therefore, it would be recommendable to optimize the mounting setup of the initially developed method for characterization of future demultiplexer samples.

4.5 Experimental setup and measurement results

A block diagram of the experimental setup for measuring the diffraction angle-dependent transmission spectrum of the demultiplexer over a broad wavelength range is shown in Fig. 4.19a. The blocks of the diagram are mutually connected with 1 mm SI-POF. The broad optical spectrum covering 400-700 nm wavelength range was provided by an Anritsu AQ4305 white light source. To ensure reproducible measurement conditions, a cylinder mode mixer according to JIS 6863 was used before the input fiber that introduced the light into the demultiplexer under test (DUT). The focusing and dispersion of the spectral components of white light along the curved focal surface of the demultiplexer Sample S2 are shown in Fig. 4.20a. The spectral components entering the output fiber were detected by an Anritsu AQ-6315A optical spectrum analyzer (OSA). To obtain the spectral response of the demultiplexer at a certain diffraction angle, a reference measurement was also required. It was performed by replacing the input fiber, the demultiplexer and the output fiber by a short piece of SI-POF with the length equal to the sum of lengths of the input and the output fiber. By scanning the demultiplexer surface over a range of diffraction angles, the overall transmission characteristic i.e. the transfer function was obtained.

Fig. 4.21a (page 66), Fig. 4.23a (page 68), Fig. 4.25 (page 70) and Fig. 4.27 (page 71) show measured transfer functions of the demultiplexer Samples S1, S2, S3 and S4 respectively, for positive diffraction angles. Fig. 4.21b (page 66) and Fig. 4.23b (page 68) show measured transfer functions of two best demultiplexer Samples (S1 and S2 respectively), for negative diffraction angles.

The represented transfer functions were obtained with the simplified measurement method using an angular resolution of 1° . The lowest reachable diffraction angle (typically 8°) was determined by the extent of spreading of the UV-curable adhesive on the demultiplexer surface around the input fiber (see Fig. 4.20). The noise level of OSA limited the highest diffraction angle for which the measurements were performed to 30° . From the transfer functions it can be noticed that at higher diffraction angles the transmission curves are more noisy at shorter than at longer wavelengths. This is because the power spectral density of white light source increases with the wavelength (from approx. -50 dBm/nm at 400 nm to -39 dBm/nm at 700 nm), raising the level of longer spectral components more above the noise

level. The spectral density curve also experiences a local minimum at around 620 nm, resulting in more noisy transmission curves in that region. As the diffraction angle decreased, the levels of spectral components entering the output fiber increased, leading to noise-free transmission curves.

The representation of the transfer function using a 3D graph, with diffraction angle as the third axis (wavelength and transmittance are standard axes), gives a comprehensive insight into transmission properties of the demultiplexer. From an individual curve, which is related to a particular angle of diffraction, it is possible to observe the IL over the wavelengths and the isolation between different wavelengths i.e. orders. It is also possible to determine the wavelengths of transmission maxima corresponding to different diffraction orders. The long spectral tails from both sides of transmission maxima are due to operation with 1 mm input fiber. In the detection layer the image of the input fiber at a particular wavelength overlaps with the images at the neighbouring wavelengths, thus causing such behaviour. Another effect contributing to the long spectral tails is the interorder scatter (see subsection 4.6.2).

By bringing several curves together to form the 3D graph, it becomes possible to observe the diffraction angles of a certain wavelength, and the shift of diffraction orders along the wavelength axis for determining e.g. the angular dispersion. Furthermore, based on the levels of transmission maxima in the successive curves, the order and the wavelength region that are the most suitable for transmission can be determined. Therefore, it is possible to completely describe the demultiplexer using a single graph.

A block diagram of the experimental setup for measuring the diffraction angle-dependent demultiplexer transmittance at a particular wavelength is shown in Fig. 4.19b. An edge-emitting laser diode launched a narrow spectral band over the mode mixer and the input fiber into the demultiplexer. The focusing and dispersion of 638 nm laser radiation along the curved focal surface of the demultiplexer Sample S2 are shown in Fig. 4.20b. A Thorlabs S140C integrating sphere and a PM100D optical power meter were used to measure the transmitted power at the end of the output fiber. As in the previous measurement, to obtain the

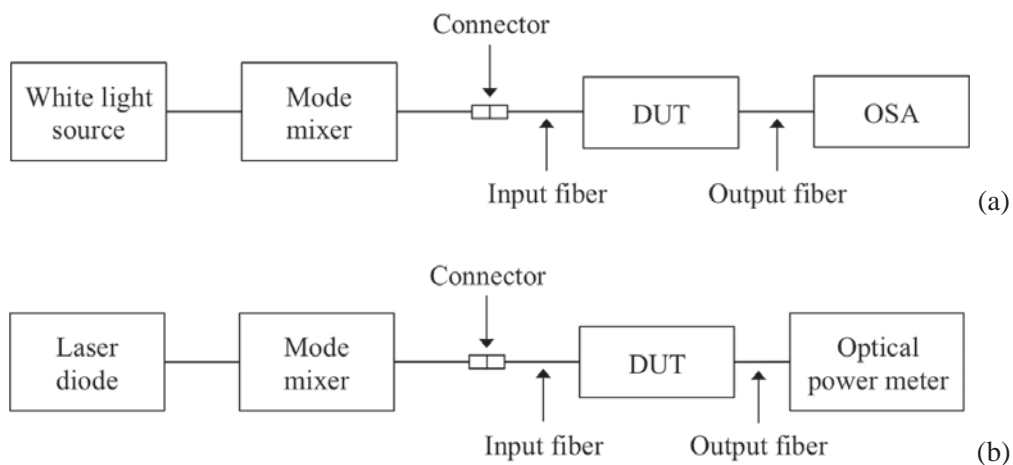


Fig. 4.19: Block diagram of the experimental setup for measuring: (a) transmission spectrum of the demultiplexer using a white light source and an OSA; (b) transmittance of the demultiplexer using a laser diode and an optical power meter.

transmittance for a given diffraction angle, a reference measurement was required. For a given lasing wavelength the transmittance curve was obtained by performing the measurement over a range of diffraction angles.

Fig. 4.22 (page 67) and Fig. 4.24 (page 69) show transmittance curves of the demultiplexer Samples S1 and S2 respectively, for positive and negative diffraction angles at five different lasing wavelengths. Fig. 4.26 (page 70) and Fig. 4.28 (page 71) show transmittance curves of the demultiplexer Samples S3 and S4 respectively, for positive and negative diffraction angles at the shortest (405 nm) and the longest (660 nm) available lasing wavelength.

The represented transmittance curves were obtained with the simplified measurement method using an angular resolution of 0.5° . The measured curves are shown in solid lines with colored markers, whereas the curves obtained by adding the correction factor to the measurement results are shown in dashed lines. The characterization was performed for the angles up to 35° , which was enough to observe the third diffraction order at 660 nm.

When the demultiplexer is to be used with the pre-defined transmitter wavelengths, describing it with transmittance curves may be more beneficial than by using complex 3D graphs. An individual transmittance curve, related to a particular lasing wavelength, gives the transmittance of the demultiplexer as a function of diffraction angle. The local maxima in the curve locate the angles of diffraction, and give the minimum IL of the demultiplexer in a particular order (see analysis in Fig. 4.22). By placing several transmittance curves below each other (as in the thesis), it becomes possible to easily determine the isolation between the individual channels. Therefore, the representation over transmittance curves gives a clear and concise insight into the demultiplexer performance with predefined transmitter wavelengths (see analysis in Fig. 4.24)

The transmittance curves can also be extracted from the transfer function drawn on the 3D graph. However, in the particular case the white light source could not provide the power spectral density high enough to compensate for high IL of the demultiplexer. That resulted in noisy curves at shorter wavelengths and higher diffraction angles. In contrast, the laser diodes provided high optical output power, allowing the noise-free measurements at short operating wavelengths and high diffraction angles.

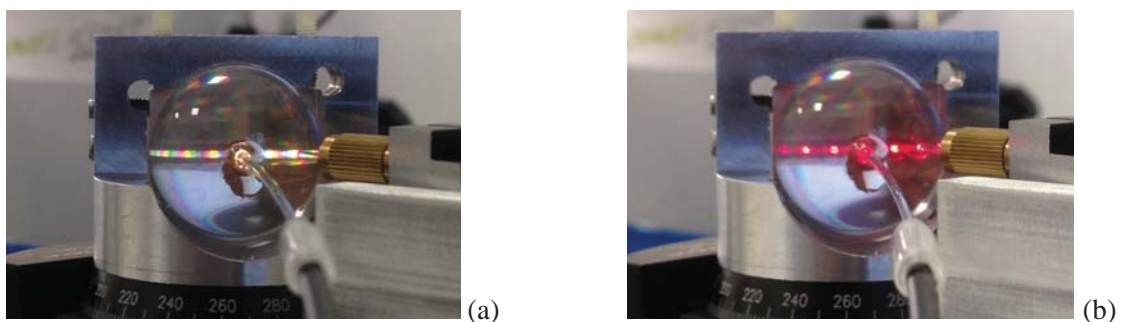


Fig. 4.20: Measuring transmission properties of the demultiplexer Sample S2 when launching with (a) white light source and (b) 638 nm laser diode. For the purpose of taking both photos an excitation of low intensity was used.

Measurement result for the Sample S1

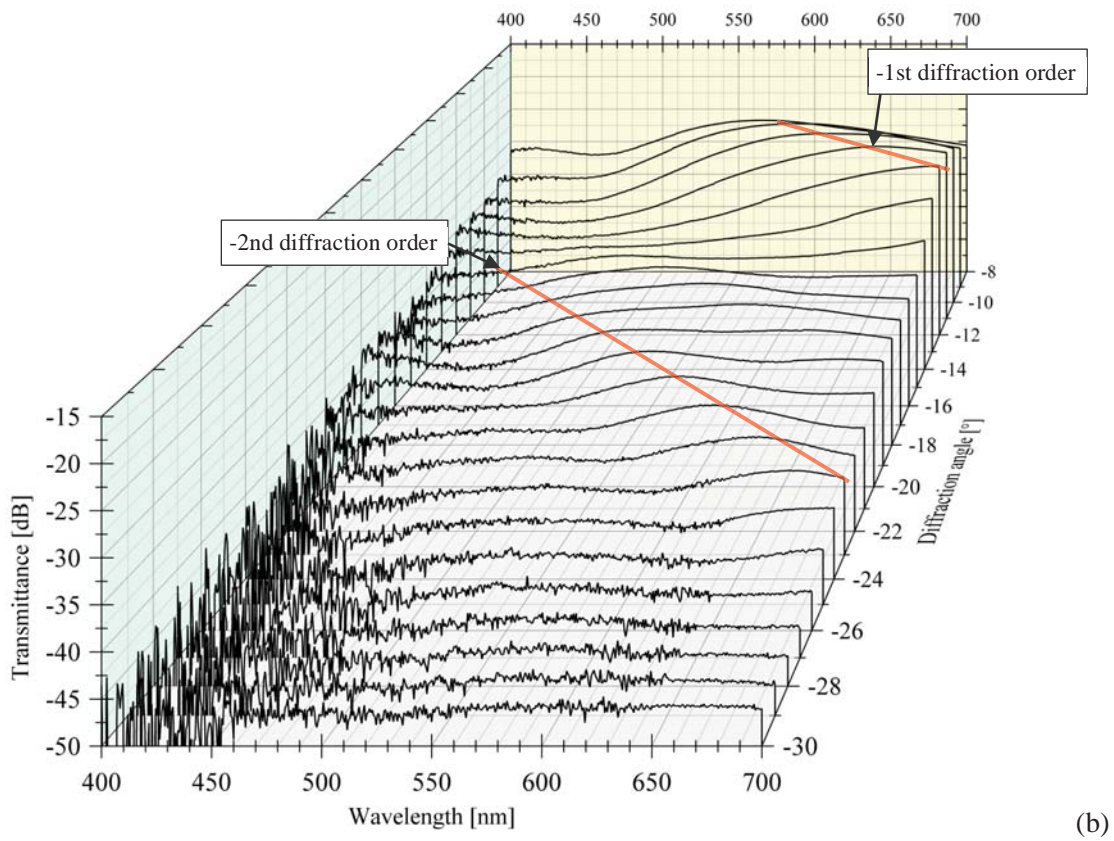
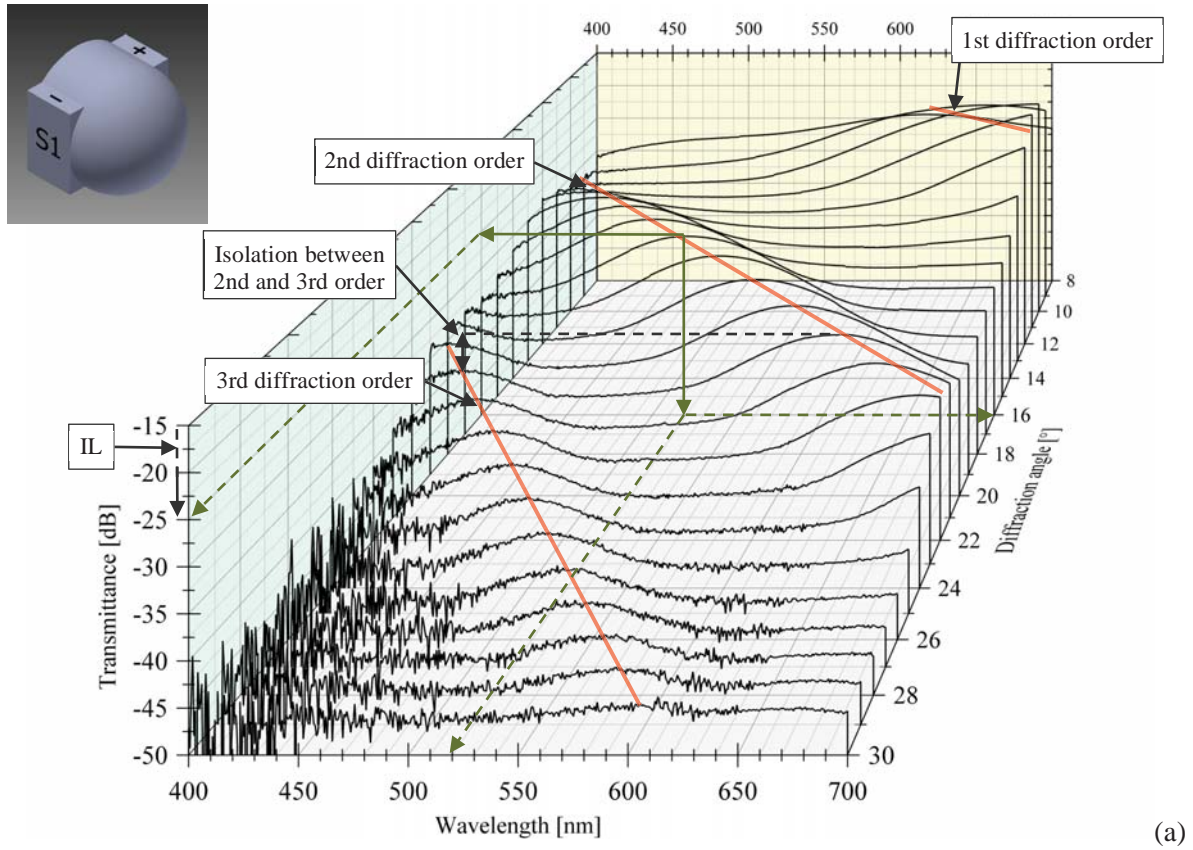


Fig. 4.21: Transfer function of the demultiplexer Sample S1 for (a) positive and (b) negative diffraction angles (measured).

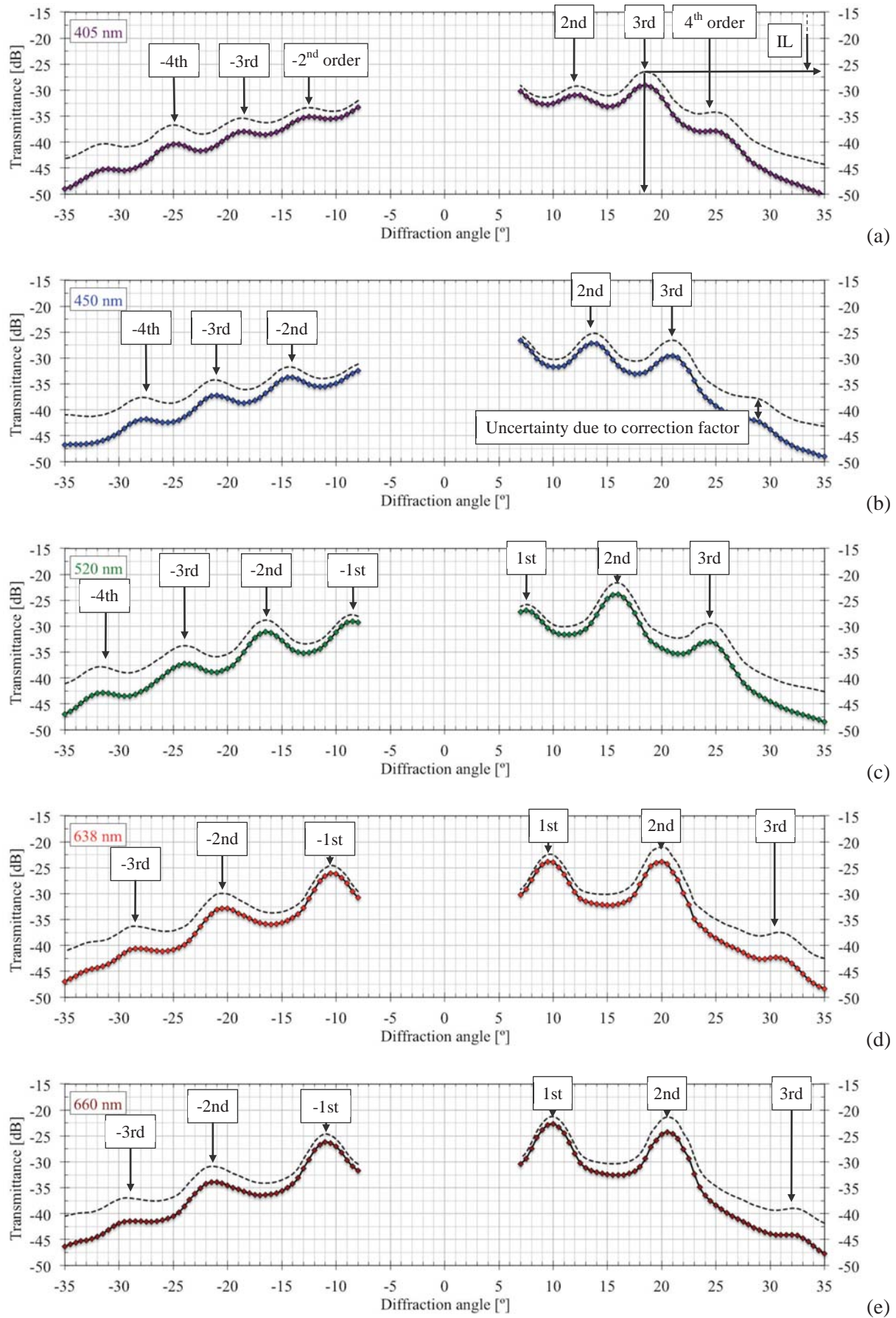


Fig. 4.22: Transmittance of the demultiplexer Sample S1 at (a) 405 nm, (b) 450 nm, (c) 520 nm, (d) 638 nm and (e) 660 nm: measured – solid line (—) with markers; corrected – dashed line (---).

Measurement result for the Sample S2

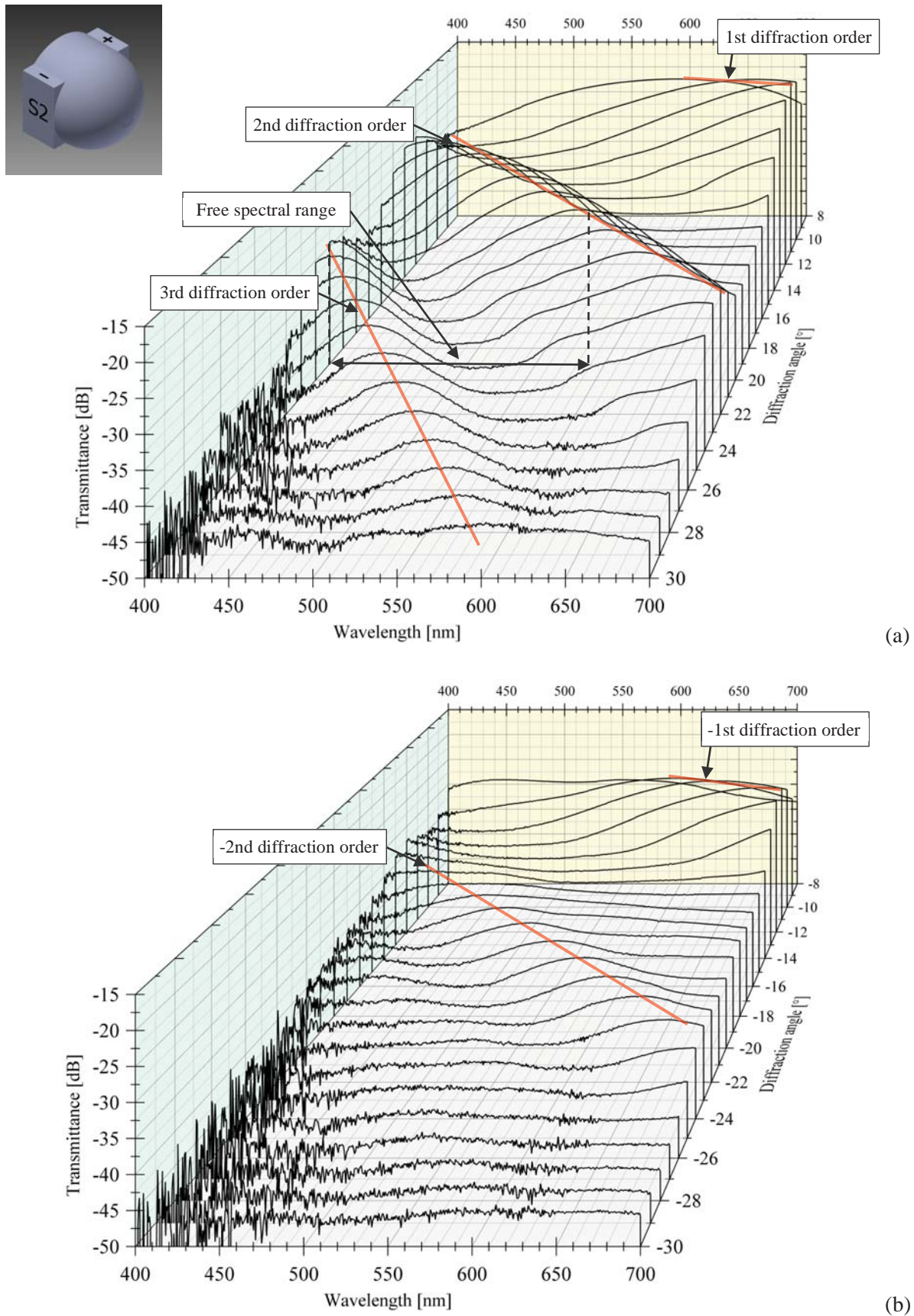


Fig. 4.23: Transfer function of the demultiplexer Sample S2 for (a) positive and (b) negative diffraction angles (measured).

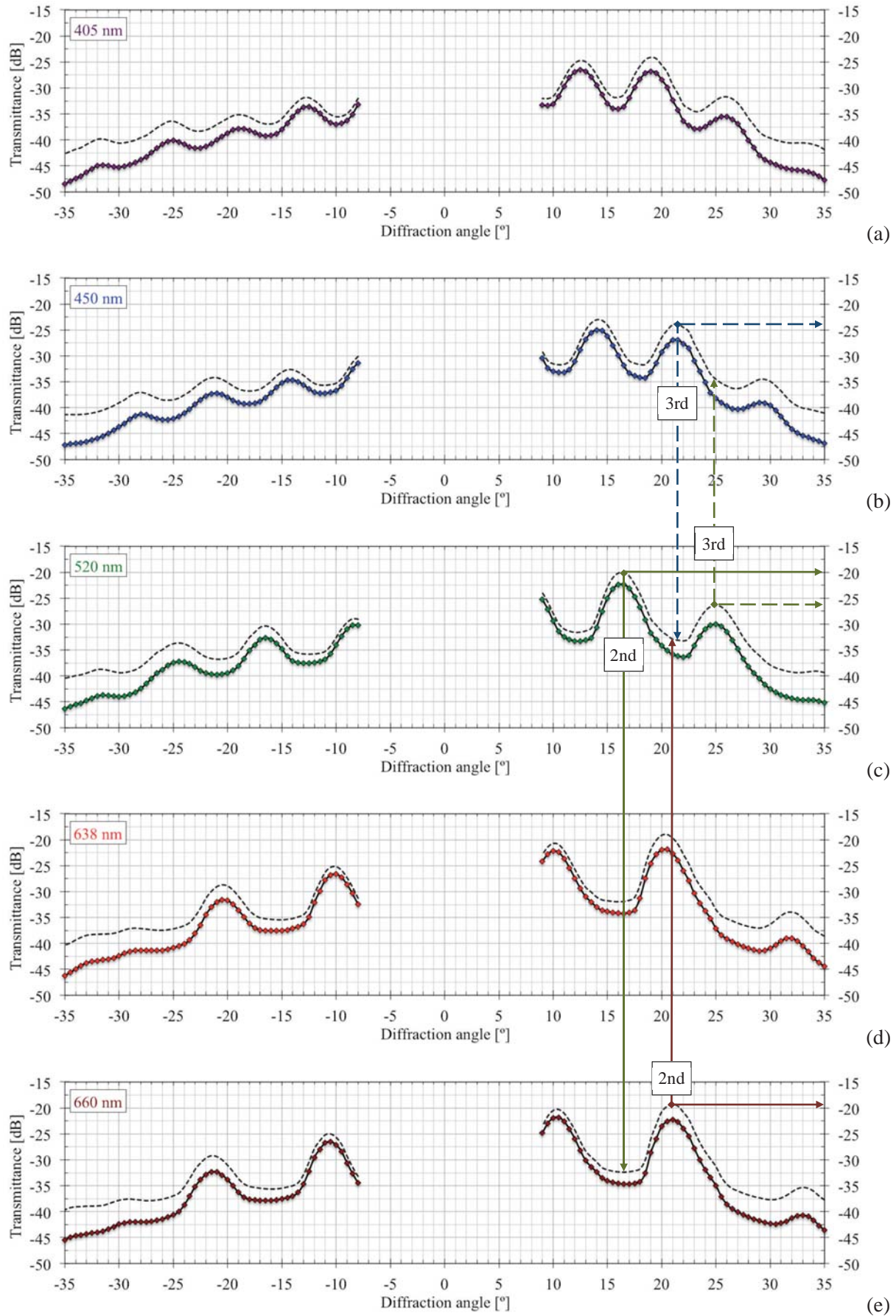


Fig. 4.24: Transmittance of the demultiplexer Sample S2 at (a) 405 nm, (b) 450 nm, (c) 520 nm, (d) 638 nm and (e) 660 nm: measured – solid line (—) with markers; corrected – dashed line (---).

Measurement result for the Sample S3

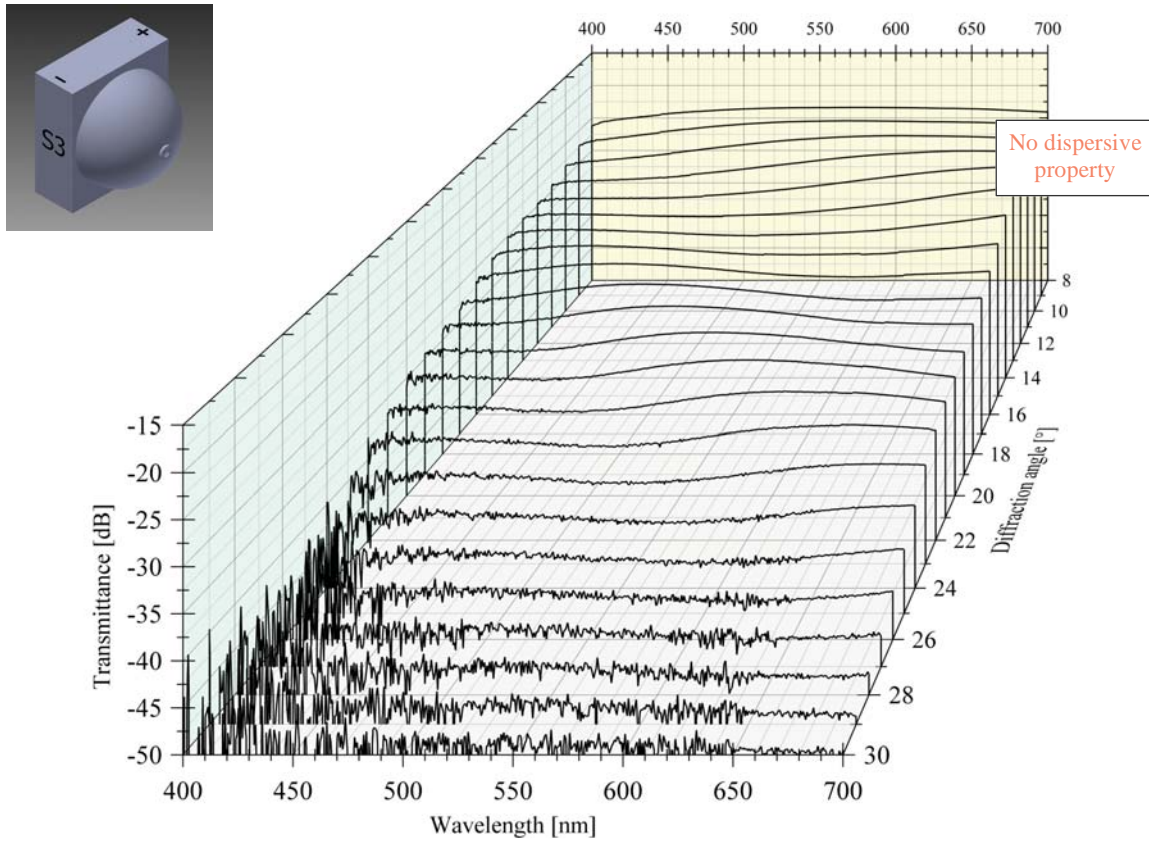


Fig. 4.25: Transfer function of the demultiplexer Sample S3 for (a) positive and (b) negative diffraction angles (measured).

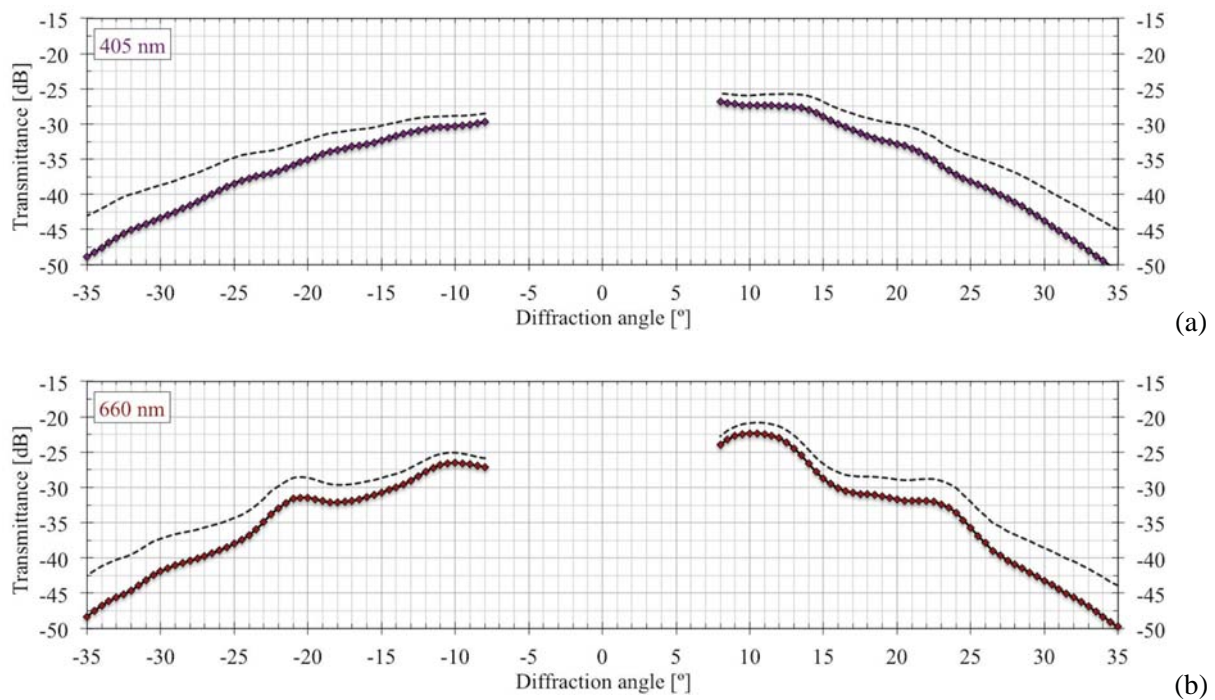


Fig. 4.26: Transmittance of the demultiplexer Sample S3 at (a) 405 nm and (b) 660 nm: measured – solid line (—) with markers; corrected – dashed line (---).

Measurement result for the Sample S4

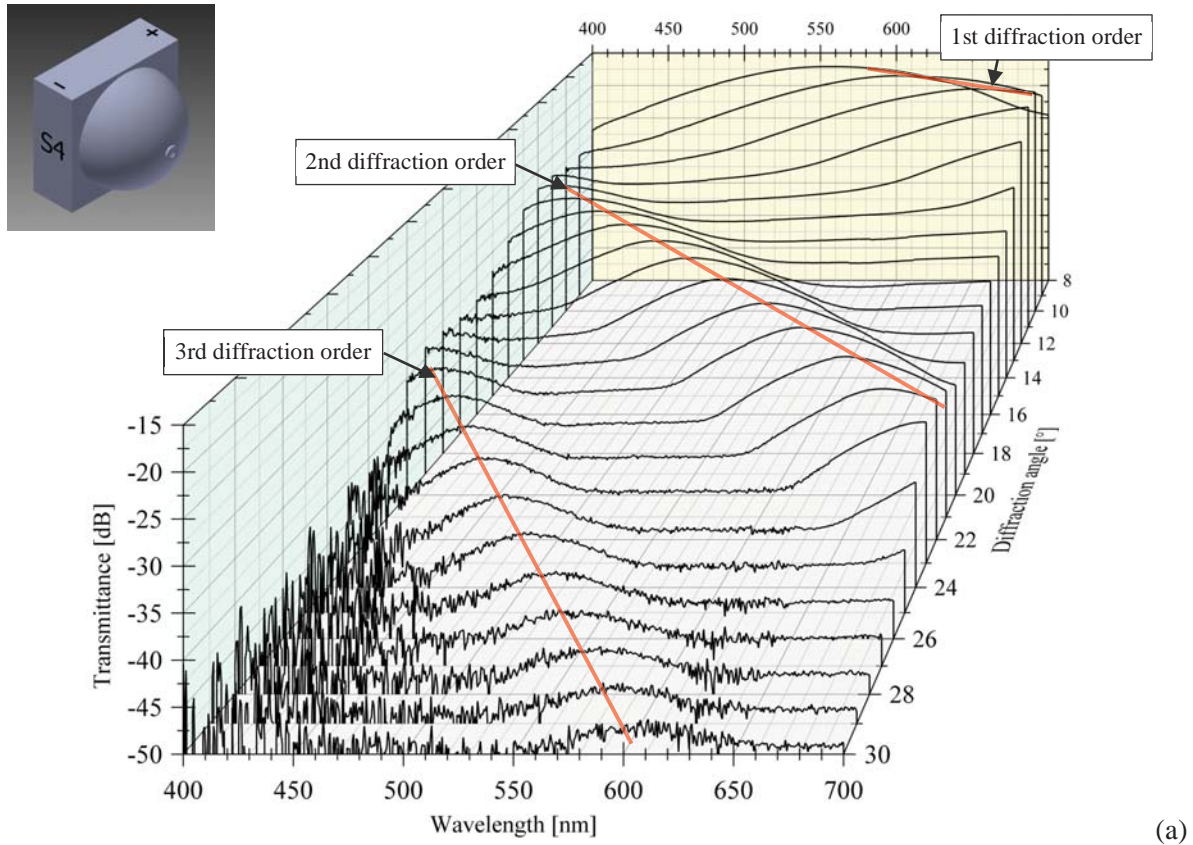


Fig. 4.27: Transfer function of the demultiplexer Sample S4 for (a) positive and (b) negative diffraction angles (measured).

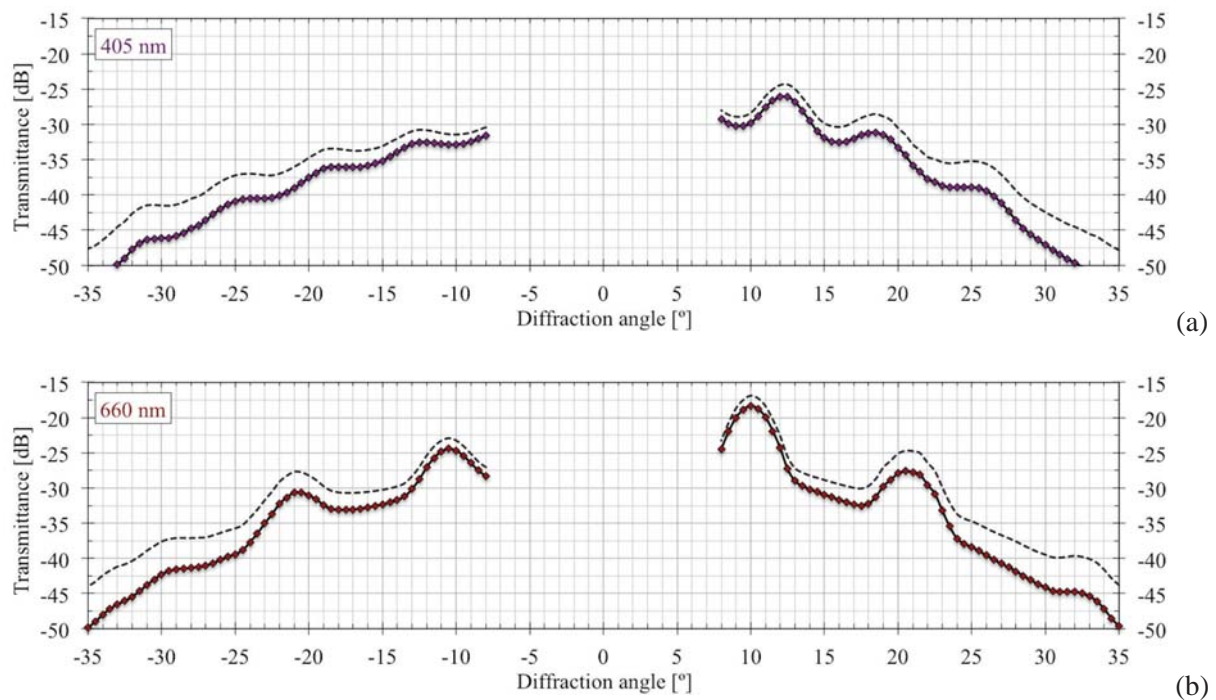


Fig. 4.28: Transmittance of the demultiplexer Sample S4 at (a) 405 nm and (b) 660 nm: measured – solid line (—) with markers; corrected – dashed line (---).



4.6 Discussion

The measurement results shown in Fig. 4.25 and Fig. 4.26 indicate that the demultiplexer Sample S3 does not exhibit any dispersive property. The subsequent visual examination of the grating and comparison to the other samples revealed that the grating looked as if it was of a spherical shape with 20.3 mm radius of curvature instead of being elliptical with 22.5 mm tangential and 20.3 mm sagittal radius (see Table 2.2). This was most likely due to the failure in the manufacturing process. Since the source was positioned outside the new Rowland circle (with 10.15 mm radius), the tangential focus was inside the new Rowland circle [Loewen97], and thus inside the demultiplexer. That resulted in reduction of the image height and spreading of the image width in the detection layer of the demultiplexer, causing the loss of dispersive property.

Further considerations in this subchapter refer to the Samples S1, S2 and S4. Since the demultiplexer was intended for use in a communication system with the pre-defined lasing wavelengths, the analysis was carried out on the basis of the transmittance curves from Fig. 4.22, Fig. 4.24 and Fig. 4.28.

4.6.1 Discussion on wavelength separating performances

Fig. 4.29 gives an overview of the diffraction angles of the Samples S1, S2 and S4 obtained from the transmittance curves as the angles where the curves exhibit local maxima. The theoretical diffraction angles are given in the same figure as a comparative reference. In addition, Fig. 4.30 closely shows the deviations of the measurement values from the theoretical ones. The deviations may partially be caused by the measurement limitations. These include:

1. Measurement resolution of 0.5° (corresponding to 1° rotation of the M-RS40 stage), introducing an angular inaccuracy of up to $\pm 0.25^\circ$.
2. Angular position readout to 0.2° from the vernier scale of the rotation stage, adding an additional inaccuracy of up to $\pm 0.1^\circ$.
3. Misalignments in the measurement setup. Those were minimized through the precise design of components and carefully controlled alignment process. A significant and under the microscope easily noticeable shift of $\pm 50 \mu\text{m}$ of the output fiber axis from the nominal one would result in an inaccuracy of approx. $\pm 0.125^\circ$. A $\pm 10 \mu\text{m}$ misalignment, corresponding to the minimum translational motion used, would cause an insignificant angular inaccuracy of $\pm 0.025^\circ$.

Therefore, it would be reasonable to adopt $\pm 0.4^\circ$ ($0.25^\circ + 0.1^\circ + 2 \cdot 0.025^\circ$) inaccuracy for the measured diffraction angles due to the measurement limitations, as indicated in Fig. 4.30.

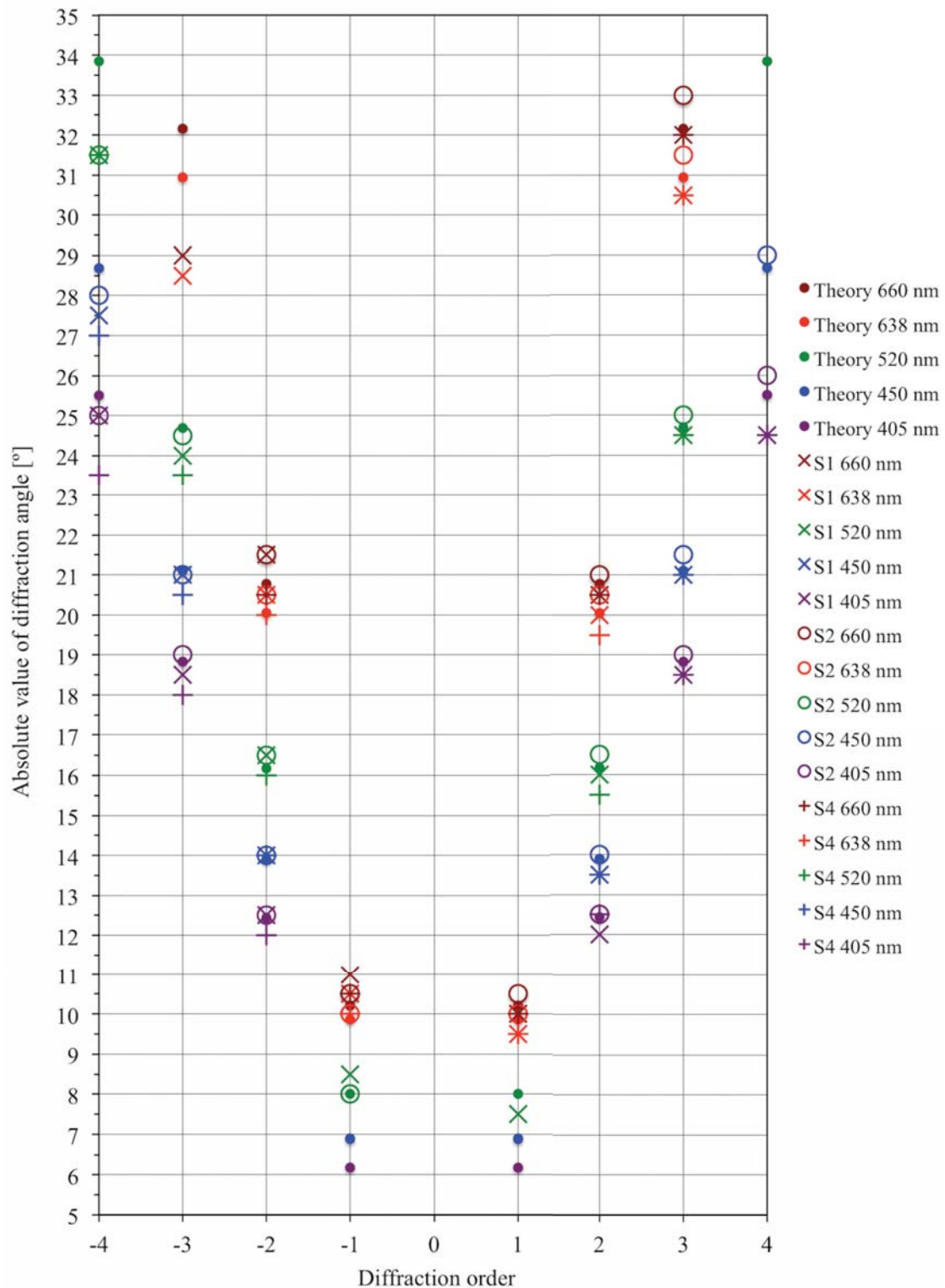


Fig. 4.29: Theoretical and measured diffraction angles of the demultiplexer Samples S1, S2 and S4 at five laser wavelengths.

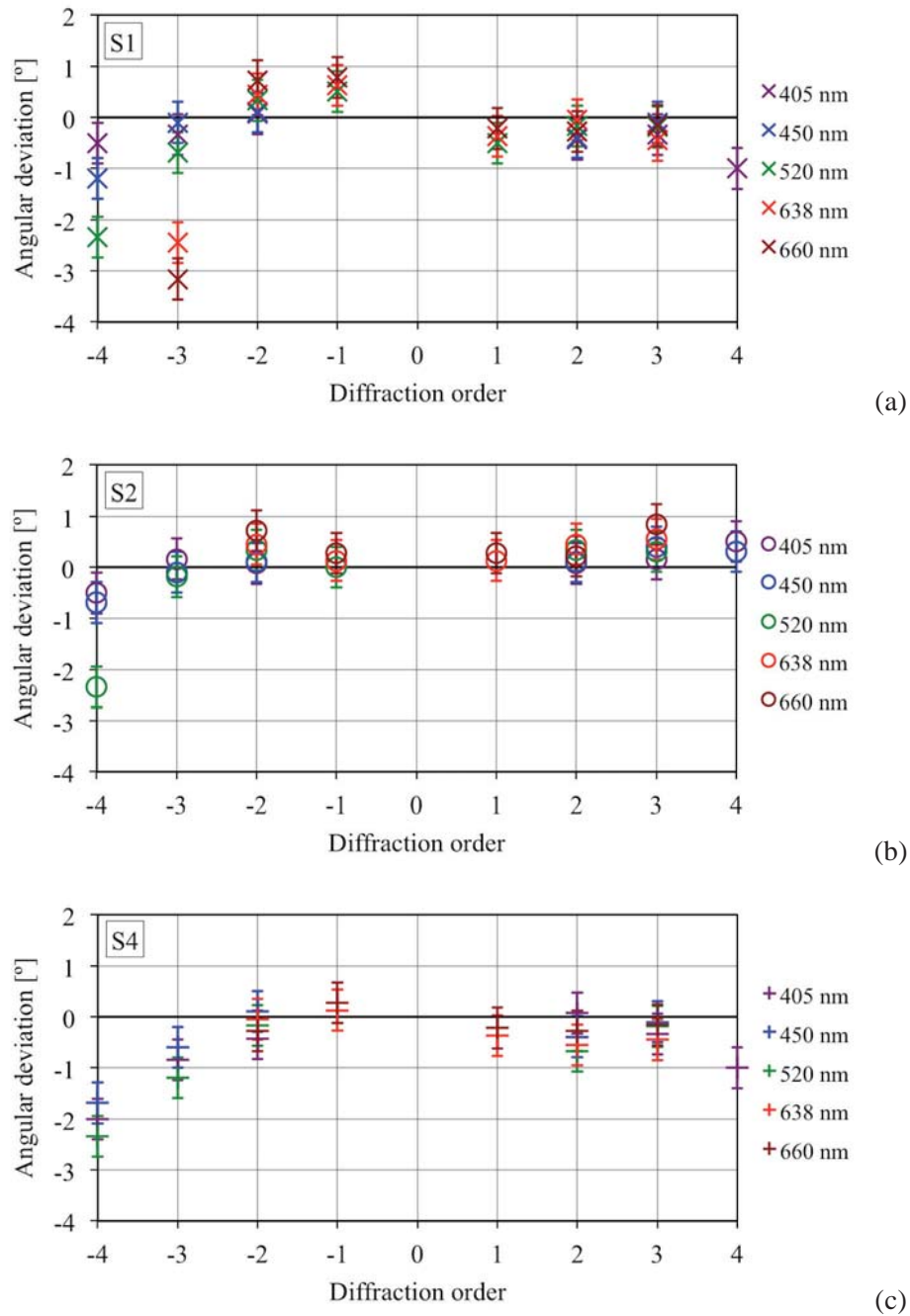


Fig. 4.30: Deviations of the measured diffraction angles (including $\pm 0.4^\circ$ inaccuracy due to measurement limitations) from the theoretical values for the demultiplexer Samples (a) S1, (b) S2 and (c) S4 at five lasing wavelengths.

The deviations of the groove spacing from the nominal value could also be identified as a reason for the mismatch between the theoretical and the measured diffraction angles. For example, Table 4.6 gives the measured groove spacing of the grating segments of the Samples S1, S2 and S4 as well as the resulting diffraction angles at 520 nm in the third order. The deviations of the corresponding diffraction angles from the theoretical value of 24.69° range between -0.54° and -1.91° . In contrast, the measurement results have deviations of only -0.19° , 0.31° and -0.19° from the theoretical angle respectively. That provides a strong indication that there exist random variations of the groove spacing across the toroidal surface.

Table 4.6: Measured groove spacings and corresponding diffraction angles at 520 nm in the third diffraction order.

Sample	S1	S2	S4
Grating segment representation	Fig. 4.5d	Fig. 4.6a	Fig. 4.8d
Measured groove spacing [μm]	2.668 [HOPE14b]	2.552 [Höll14]	2.696 [HOPE14b]
Diffraction angle at 520 nm in 3rd order [$^\circ$]	23.04	24.15	22.78
Deviation form the theoretical angle [$^\circ$]	-1.65	-0.54	-1.91

From Fig. 4.30 it can be observed that the deviations of the measured values from the theoretical ones that do not come from the measurement limitations might be present. Large deviations (e.g. in -4th order) might indicate that the constructive interference occurs at smaller angles then expected due to the inhomogeneous structure of the grating. The differences in the absolute diffraction angles between the positive and the corresponding negative orders can also be noticed, probably due to the same reason. Because of the random variations of the groove spacing across the toroidal surface, only a general observation based on Fig. 4.29 and Fig. 4.30 can be made that the measurement results are closely distributed around the theoretical values. That implies that the groove spacing was a parameter of the ruling process that was easier to control than the groove shape and the groove depth (see next subchapter).

4.6.2 Discussion on transmission performances

The considerations in this subchapter refer to the Samples S1 and S2, which exhibit better grating structure (groove depth and groove shape) and thus better demultiplexing properties than the Sample S4. As can be observed from the transmittance curves of the Samples S1 and S2, the minimum IL (with the correction factor included) was around 20 dB. In Table 4.7 the author roughly estimates individual contributions to the overall IL of the demultiplexer.

The light entering the demultiplexer suffered from the propagation loss in PMMA. Because of the short optical path in the demultiplexer (approx. 4.5 cm), the propagation loss played an insignificant role in the overall IL of the demultiplexer. For example, according to Fig. 2.1 the

Table 4.7: Estimation of individual contributions to the IL of the demultiplexer.

Fresnel reflection between the input fiber and the demultiplexer [dB]	0
Propagation loss in PMMA material of the demultiplexer [dB]	0.005
Absorption on the aluminium coating deposited on the grating [dB]	0.36
Diffuse scattering introduced by the grating [dB]	6
Diffraction efficiency of the grating, interorder scatter and coupling loss in the image layer [dB]	> 14
Total loss [dB]	> 20

propagation loss at 650 nm was approx. 0.005 dB. Furthermore, it could be assumed that no Fresnel reflections occurred when the light transited from the input fiber into the demultiplexer due to the UV-curable adhesive filling the air gap.

From the light incident on the toroidal grating one portion was absorbed on the aluminium coating, another portion was scattered and the rest was diffracted according to grating equation. For an average reflectivity of aluminium of around 92% within λ_{PMMA} operating range (266-471 nm), the contribution of 0.36 dB to the IL was considered at any wavelength and diffraction angle.

An unwanted effect of the light being diffusely radiated (i.e. into all directions) from the Rowland circle-based half sphere and from the demultiplexer body was possible to observe in a darkened room or with an increased intensity of white light or laser excitation. The diffuse scattering was predominantly caused by a poor, practically non-existent grating structure in the lower half of the toroidal surface. Taking the grating segments from Fig. 4.5e and Fig. 4.6b as a reference, it could be reasonably assumed that most of the light incident on the lower half of the grating (50% of total light intensity) was diffusely scattered. That resulted in approx. 3 dB contribution to the IL.

Furthermore, the roughness of the grating surface on the scale of the incident wavelength [Loewen97] as well as the obvious imperfections (e.g. pinholes, bumps and scratches) in the upper half of the grating caused a portion of incident light to be scattered diffusely. It was considered that up to 50% of light incident on the upper half of the grating could have been diffusely scattered, causing the additional loss of 3 dB.

Therefore, approx. 75% of light incident on the grating was diffusely scattered due to the poor quality of the grating surface. That corresponded to 6 dB loss. The minimum IL of around 20 dB suggests that the diffraction efficiency, interorder scatter and imaging aberrations caused most of the optical power loss in the demultiplexer (> 14 dB).

For the light diffracted according to the grating equation the intensity distribution of a certain wavelength among diffraction orders was determined by the diffraction efficiency in the individual orders. Even though the blaze condition should have been satisfied for 505.6 nm in the third order, it can be noticed that for a neighbouring wavelength of 520 nm the Samples S1 and S2 concentrated more energy in the second than in the third order (see Fig. 4.22c and Fig. 4.24c respectively). However, the simulated diffraction efficiency according to Fig. 4.3 experienced a maximum in the third and a minimum in the second order around 520 nm. Correspondingly, the behaviour opposite to the measured one was expected. An additional contradiction was imposed by the fact that the imaging aberrations were minimized around 520 nm in the third order. Therefore, the measurement results provided a strong indication that the parameters of the ruling process were not stable enough to produce an accurately shaped sawtooth profile with a required blaze angle (groove depth). As a consequence, the distribution of light among the orders did not follow the expected diffraction efficiency according to Fig. 4.3.

Furthermore, for the Sample S2 the interorder scatter can be observed in Fig. 4.20b where the laser excitation of low intensity was used. It was manifested as a reduced but still present light intensity in the dispersion plane between the orders. According to [Palmer05], this type of scatter indicates the presence of the random deviations in the groove spacing from the nominal one, and of the irregularities in the depth of the grooves.

Finally, the dimensions of the input fiber images in the detection layer were primarily affected by the sagittal radius of the grating. That was the production parameter certainly easier to control than e.g. the groove depth. However, the inhomogeneous grating structure also influenced the dimensions of the fiber images and their intensity distribution. Consequently, it was not possible to analyse the coupling efficiency separate from two other loss mechanisms (diffraction efficiency and interorder scatter).

Since the diffraction efficiency, interorder scatter and image dimensions complexly depend on the groove depth, groove shape and groove spacing, it was not possible to determine their individual contributions to the IL of the demultiplexer based on the performed transmittance measurements. However, their joint contribution was estimated to be larger than 14 dB. That indicates that the ruling process would have to be optimized in order to produce a more accurate grating structure that could possibly ensure demultiplexer IL of less than 5 dB.

Among all analyzed samples, the Sample S2 offered the best demultiplexing properties. In the third diffraction order the corrected IL at 450 nm and 520 nm was 23.83 dB and 26.34 dB (measured 26.89 dB and 30 dB) respectively. The respective channel isolation was 9.27 dB and 8.17 dB. In contrast to the theoretical expectations given in subchapter 4.2, the demultiplexer offered better detecting possibilities in the second then in the third order (see analysis in Fig. 4.24). As described in subchapter 4.2.1, the suitable wavelength channels in the second order would be those at 405 nm, 520 nm, and 660 nm. The corresponding corrected IL was 24.72 dB, 20.06 dB and 19.27 dB (measured 26.47 dB, 22.35 dB and 22.24 dB). The isolation between the channels is shown in Table 4.8. Because of the low isolation in 405 nm channel, it can be stated that the best performance from the Sample S2 can be obtained for 520 nm and 660 nm channels in the second order (IL \approx 20 dB, channel isolation \approx 13 dB).

Table 4.8: Isolation between 405 nm, 520 nm and 660 nm channels in the second order.

Channel Rx \ Channel Tx	405	520	660
405	/	11.26	10.1
520	6.83	/	13.64
660	1.73	12.33	/

4.6.3 Recommendations

Due to the high IL and low channel isolation, the produced demultiplexer samples did not fulfil the requirements to be used for high-speed POF WDM transmission experiments. Further optimization of the demultiplexer is required to realize a functional device capable of supporting POF WDM applications:

- When used with SI-POF, the demultiplexer with the current parameters could separate two channels in the third diffraction order (see subchapter 4.2.2). The blaze angle and the sagittal radius should be re-optimized for operation with three channels in the second order. For operation with a higher channel count the dimensions of the demultiplexer (e.g. tangential radius, grating height and width) would have to be increased. Alternatively, the demultiplexer could be re-designed for use with the smaller-diameter fibers.
- Stabilizing the parameters of the ruling process is necessary to obtain an accurately shaped sawtooth profile with the required groove spacing and groove depth. If that would be achieved, a master grating could be directly ruled on a molding tool in order to cost-effectively produce the demultiplexer through injection moulding. That could open up the possibilities for commercial implementation of POF WDM.
- To enable easy plug-in of the input and the output fibers, a demultiplexer design with the fixed entrances for the fibers, as suggested in [Höll13], could be employed.

5 Four-channel POF WDM transmission experiments

The lack of functional low-loss multiplexing and demultiplexing components and of fast visible light sources was the key factor preventing high-speed POF WDM experiments for a long time. In the early attempts, the LED-based POF systems exploiting WDM technology could not provide sufficient capacity [Junger02], [Appelt02], [Bartkiv03]. Only recently, supported by the advance in visible laser diode technology, the record-breaking POF WDM transmission experiments were performed. First, 10.7 Gb/s transmission over 50 m SI-POF employing a three-channel interference filter-based demultiplexer was reported in [Kruglov12a]. The same authors further increased the capacity to 21.4 Gb/s over the same link length using a six-channel plane diffraction grating-based demultiplexer [Kruglov14]. Shortly thereafter, preceded by several optimization steps shown in [Jončić13b], [Jončić13c], [Jončić14a], a capacity of 14.77 Gb/s was demonstrated over 50 m SI-POF employing a four-channel interference filter-based demultiplexer [Jončić14b]. Based on the same demultiplexing solution, the transmission distance was extended to 100 m resulting in 8.26 Gb/s capacity [Jončić14c]. All data rates were measured at the $\text{BER}=10^{-3}$, allowing for error free transmission after applying FEC with 7% redundancy. The experiments not only demonstrated the feasibility of a high-speed POF WDM concept, but also offered significant capacity increase compared to the single-wavelength systems.

This chapter describes the author's activities resulting in the record-breaking four-channel POF WDM transmission experiments over 50 m and 100 m links. Several optimization steps with intermediate results are represented before the target experimental setup and results are shown.

In the experiments a pre-coded target BER of 10^{-3} was adopted, which is a common value used in high-speed POF communication, e.g. [Vinogradov11], [Kruglov12a], [Loquai13]. That BER value complies with the FEC threshold and can be reduced to $\text{BER}<10^{-9}$ after applying FEC with 7% redundancy ratio [ITU04].

The experiments were carried out over 1 mm Asahi KASEI DC-1000 SI-POF (POF class A4a.2 according to IEC 60793-2-40). To separate the wavelength channels at the receiver, the four-channel interference filter-based SI-POF demultiplexer with two-stage configuration was used. The corresponding transfer function is represented in Fig. 3.10.

The basic parameters of the laser diodes used in different measurements are listed in Table 5.1. Besides the diode in position 4, all other devices are commercially available. The diode operating at 515 nm was a research and development sample provided by Osram Opto

Semiconductors. The product with similar characteristics (diode in position 5) became available on the market afterwards.

Table 5.1: Basic parameters of the laser diodes used in different data transmission experiments (datasheet information for the case temperature of 25° C): λ_{op} – operating wavelength; P_{out} – optical output power; I_{th} – threshold current; I_{bias} – recommended bias current.

Position	λ_{op} [nm]	P_{out} [dBm]	I_{th} [mA]	I_{bias} [mA]	Type name	Manufacturer	Package
1	405	16	35	70	DL-5146-101S	Sanyo	TO-56
2	405	19	45	110	DL-7146-101S	Sanyo	TO-56
3	450	19	30	100	PL 450B	Osram	TO-38
4	515	17	60	160	R&D sample	Osram	TO-38
5	520	14	45	150	PL 520	Osram	TO-38
6	639	10	30	40	HL6358MG	Opnext	TO-56
7	656	14.8	35	65	QL65I7SA	QSI	TO-56
8	660	17	60	115	HL6544MG	Opnext	TO-56

A Graviton SPD-2 receiver comprising a lens coupling system, a Ø 400 µm silicon PIN-photodiode and a transimpedance amplifier was used for detection. The receiver is widely accepted as a benchmark optical to electrical converter for the laboratory tests and has a sensitivity of -19 dBm at 1 Gb/s (at 650 nm) [Gaudino11]. It provides a frequency bandwidth from DC to 1.2 GHz, and has a saturation power level of -4 dBm at 650 nm. The maximum optical power providing a proper signal output at the available lasing wavelengths, estimated on the basis of the responsivity curve [Graviton06], is given in Table 5.2.

Table 5.2: Saturation power of the Graviton SPD-2 receiver at the available lasing wavelengths.

Operating wavelength [nm]	405	450	515	520	639	656	659
Saturation power [dBm]	1.24	-0.32	-1.55	-1.65	-3.76	-4.05	-4.07

5.1 WDM transmission employing NRZ modulation

This subchapter shows the initial experimental setup and gives the measurement results prior and after the first optimization step. Even though performed measurements cannot be considered as real WDM, the setup with multiplexer and demultiplexer along the optical path was assembled, and its functionality was demonstrated. The results of the experiments were presented at the ICPOF 2013 [Jončić13b].

5.1.1 Experimental setup

The data transmission setup is shown in Fig. 5.1. It comprised an Agilent N4903A bit error rate tester (BERT), four butt-coupled edge-emitting laser diodes, multiplexing POF coupler, 10 m SI-POF link, interference-based POF demultiplexer, optical receivers and Agilent 86100B sampling oscilloscope.

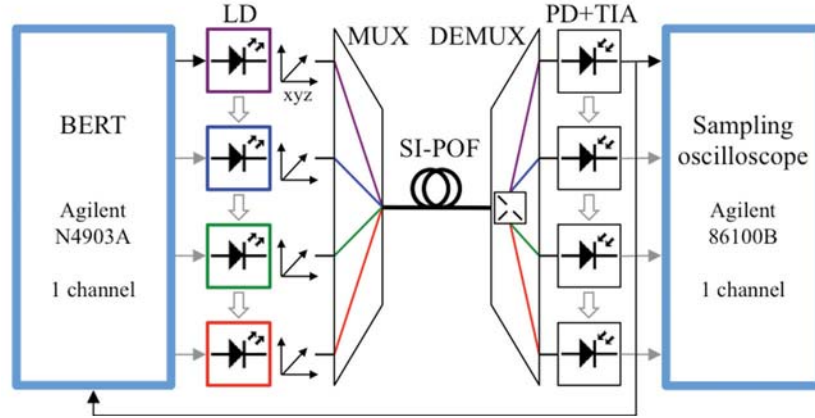


Fig. 5.1: Experimental setup for the measurements employing NRZ modulation: LD – laser diode; MUX – multiplexer; DEMUX – demultiplexer; PD – photodiode; TIA – transimpedance amplifier.

To provide precise temperature control, prevent possible damage from overheating and extend the lifetime, the laser diodes were mounted in Thorlabs TCLDM temperature controlled laser diode mounts. The temperature of an integrated temperature control (TEC) element of the mount was adjusted to +15 °C. Only for OSRAM samples the cooling at +10 °C was used to provide better stability of the optical output power. Both the temperature of the TEC element and the bias current were controlled over a Thorlabs ITC8022 module. Four of those modules were installed in a Thorlabs PRO8000 modular chassis for the simultaneous control of four operating diodes (see Fig. 5.6). To maximize the coupling efficiency from the laser diode into the fiber, a butt-coupling unit based on an *xy*-translator (0.25 mm pitch of the adjustment screws) was utilized. The translator was mounted on the TCLDM9 mount over a 4-rod construction system, as shown in Fig. 5.3c.

To combine the optical signals with different wavelengths onto the SI-POF link, a Comcore 4×1 fused POF coupler was used. Two tested coupler samples showed similar IL behavior. For direct launching with 405 nm (DL-5146-101S), 450 nm, 515 nm and 639 nm laser diodes, the IL between any of four input (laser coupled) ports and the output (fiber coupling) port was 8-9 dB. Taking into account the launching loss from the laser diode into the input coupler port (1.3-1.5 dB), and the loss of a connector interface between the output coupler port and SI-POF link (approx. 0.5 dB), the fiber-coupled power was by approx. 10 dB lower than the optical output power of any of the employed laser diodes (see Table 5.3).

Table 5.3: Optical power loss at the transmitter side when using 4×1 fused POF coupler.

Operating wavelength [nm]	405	450	515	639
Laser diode-to-coupler port launching loss [dB]	1.5	1.3	1.3	1.5
IL of 4×1 fused POF coupler [dB]	7.9	8.9	8.1	8.6
Connector loss (with index matching gel) [dB]	0.5			
Total loss [dB]	9.9	10.7	9.9	10.6

The BERT was used to generate an up to 1.8 V_{pp} bipolar NRZ signal based on 2⁷-1 pseudo-random binary sequence (PRBS). After adding a DC-bias, the signal was used to modulate the optical output of the laser diodes in their linear lasing region. The eye diagrams were monitored on the sampling oscilloscope, whereas the BERT was used for BER estimation. Since the BERT and the sampling oscilloscope provided one electrical output and input channel respectively, the transmission experiments were performed with one active WDM channel at a time, as indicated in Fig. 5.1.

5.1.2 Measurement results and discussion

2.5 Gb/s transmission over 10 m SI-POF

The laser diodes providing the signals at four different wavelengths operated at 405 nm (DL-5146-101S), 450 nm, 515 nm and 660 nm. Each diode was inserted into a laser socket of the TCLDM mount, which was also equipped with an internal 500 MHz bandwidth bias-tee and had separate inputs for the bias and modulating current. The respective data rates achieved in the individual WDM channels were 0.5 Gb/s, 0.5 Gb/s, 0.7 Gb/s and 0.8 Gb/s. The corresponding eye diagrams are represented in Fig. 5.2. The effect of pulse shaping due to the low pass characteristic of the fiber can clearly be recognized, e.g. in 405 nm channel. The irregular signal trajectories, e.g. in the eye diagrams of 515 nm and 660 nm channels, indicate the presence of nonlinearities in the electrical domain (presumably introduced by the bias-tee circuit). No BER measurement data were saved. However, due to the eye diagrams still opened wide enough, it can be reasonably assumed that the corresponding BERs were below the FEC threshold of 10⁻³, allowing for the error correction.

High optical isolation of the demultiplexer provided very low optical crosstalk between the WDM channels. The crosstalk of < -35 dB, coming from 450 nm channel, was detected in 515 nm channel. In all other channels the crosstalk lower than -45 dB was detected with a Melles Griot 13 PDH 005 integrating sphere. Considering the amplitude levels of the recorded eye diagrams and low interchannel crosstalk, no reduction in the SNR of the received signals could be assumed if the laser diodes were modulated simultaneously. Therefore, it can be stated that an aggregate bit rate of 2.5 Gb/s could be transmitted over 10 m SI-POF with four simultaneously active channels and no interchannel errors. The corresponding information rate after deduction of 7 % FEC overhead would be 2.33 Gb/s.

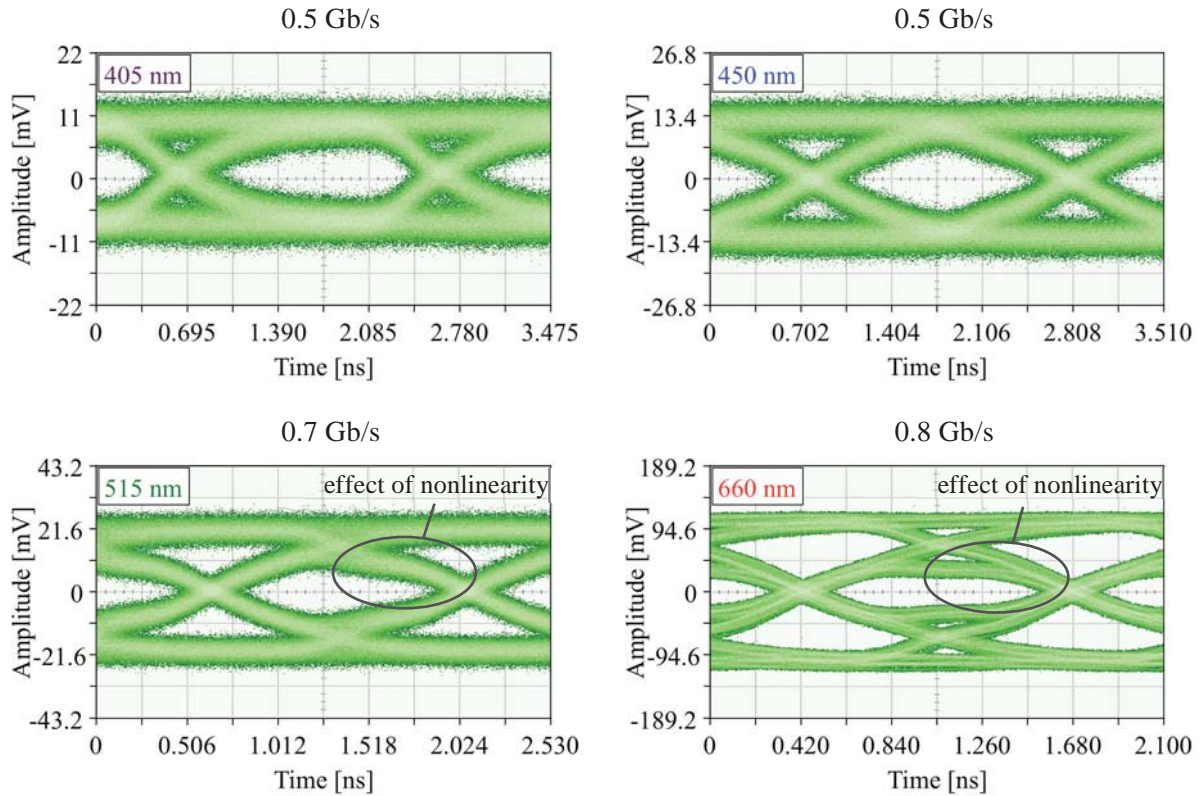


Fig. 5.2: Eye diagrams for 10 m SI-POF link at an aggregate bit rate of 2.5 Gb/s (note: the full time scale was automatically set by the oscilloscope and is smaller than two unit intervals of the signal).

5 Gb/s transmission over 10 m SI-POF

In the next experiment, 405 nm (DL-5146-101S), 450 nm, 515 nm and 639 nm laser diodes were used as WDM optical sources. To directly modulate the diodes with a higher modulation bandwidth, each diode was soldered to a 50 ohm SMA formable coax cable (Fig. 5.3a), which was connected to the output of an external bias-tee with 6 GHz bandwidth and 0.1 MHz low cutoff frequency. Due to the low impedance of the laser diodes (typically 2-5 ohms), a severe impedance mismatch was present. However, by using higher power of the modulating signals the mismatch could be compensated. For mounting the diodes into the mounts, copper retainer rings for both TO-56 and TO-38 packages were fabricated (Fig. 5.3b). For better thermal conductivity between the TEC element of the mount, the retainer ring and the laser diode housing, a heat-conductive paste was applied on the contact surfaces.



Fig. 5.3: Driving, cooling and coupling of laser diodes: (a) TO-56 diode soldered to a formable coax cable; (b) TO-56 diode mounted in a retainer ring; (c) TCLDM9 mount with a butt-coupling unit.

The bit rates in the individual channels were 1.25 Gb/s (405 nm channel), 1.05 Gb/s (450 nm channel), 1.25 Gb/s (515 nm channel) and 1.45 Gb/s (639 nm channel). The transmission parameters for the individual channels are listed in Table 5.4. The corresponding eye diagrams are represented in Fig. 5.4. In contrast to the previous measurement, no signal nonlinearities were present, and the maximum achievable data rates were limited by the ISI.

Table 5.4: Transmission parameters for 10 m SI-POF link at an aggregate bit rate of 5 Gb/s.

Operating wavelength [nm]	405	450	515	639
Bit rate [Gb/s]	1.25	1.05	1.25	1.45
BER	$6 \cdot 10^{-5}$	$7 \cdot 10^{-5}$	$1.1 \cdot 10^{-6}$	$9 \cdot 10^{-7}$

Taking into account the amplitude levels of the recorded eye diagrams and low interchannel crosstalk, like in the previous experiment no power penalty due to crosstalk could be assumed if the laser diodes were modulated simultaneously. Therefore, it can be stated that 5 Gb/s transmission could be realized over 10 m SI-POF link at the $\text{BER} < 10^{-4}$ with four simultaneously active channels and no interchannel errors. Using a standard Reed-Solomon (255,247) FEC with 3.2% redundancy, 4.84 Gb/s transmission could be achieved at the $\text{BER} < 10^{-9}$ [Azadet99].

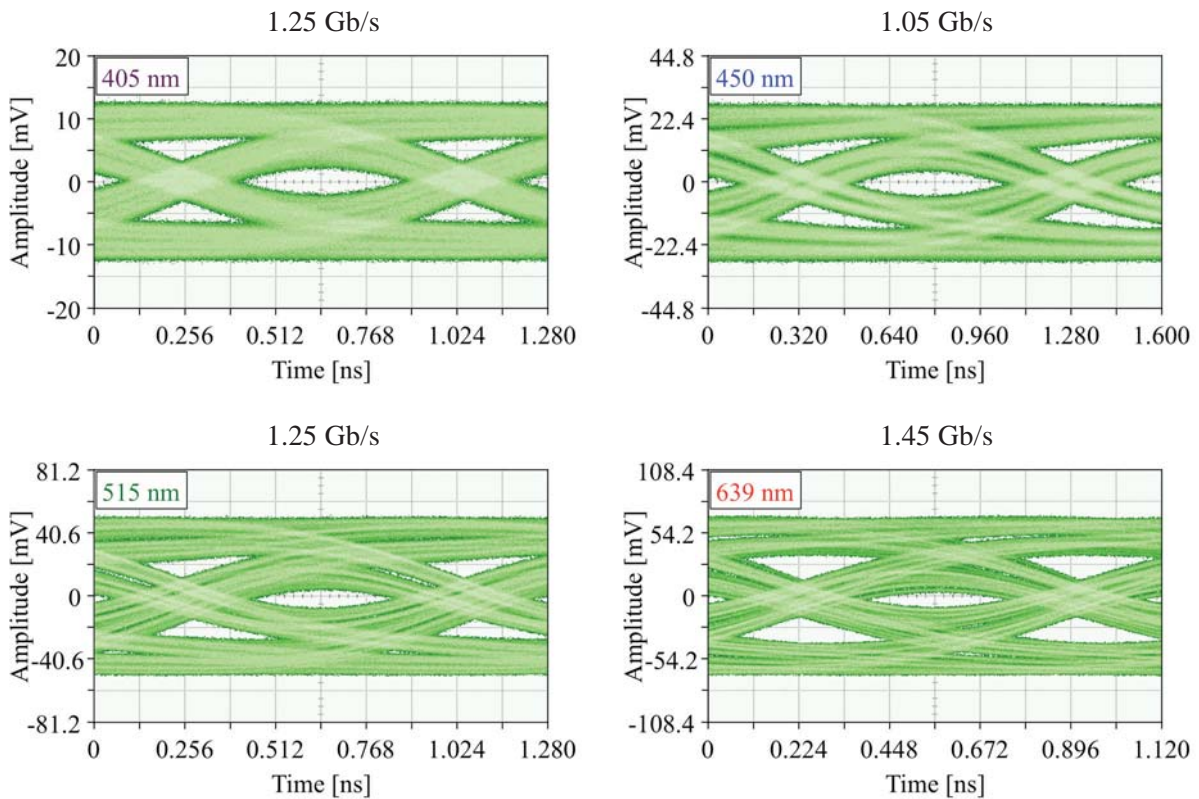


Fig. 5.4: Eye diagrams for 10 m SI-POF link at an aggregate bit rate of 5 Gb/s (note: the full time scale was automatically set by the oscilloscope and is smaller than two unit intervals of the signal).

It should be noted that in both measurements the parameters of the setup were not optimally adjusted. For example, the wavelength dependency of the receiver's saturation power was not taken into consideration. Instead, the received power in any of the channels was limited to -4 dBm, e.g. by introducing longitudinal launching offset for the laser diodes, thus impairing the system performance. Nevertheless, the functionality of the demultiplexer and of the assembled setup was tested through the measurements, and the optimization by direct soldering of the diodes to the SMA coax cables was validated.

5.2 WDM transmission employing NRZ modulation and FFE equalization

This subchapter shows the improved experimental setup and gives the measurement results of the simultaneous four-channel NRZ transmission over 50 m and 100 m SI-POF. To mitigate the effects of ISI, the FFE equalization was implemented at the receiver side. The results of the experiments were partially presented at the ITG Symposium on Photonic Networks (ITG Fachtagung Photonische Netze) 2014 [Jončić14a].

5.2.1 Experimental setup

The experimental setup is shown in Fig. 5.5. It comprised a four-channel Agilent M8190A arbitrary waveform generator (AWG), four butt-coupled edge-emitting laser diodes, four-legged multiplexing POF bundle, SI-POF link of two different lengths, interference-based POF demultiplexer, Graviton SPD-2 receiver and four-channel Agilent DSA91604A real-time oscilloscope with built-in software for digital signal processing. A photo of the general setup for investigating four-channel high-speed POF WDM transmission is shown in Fig. 5.6.

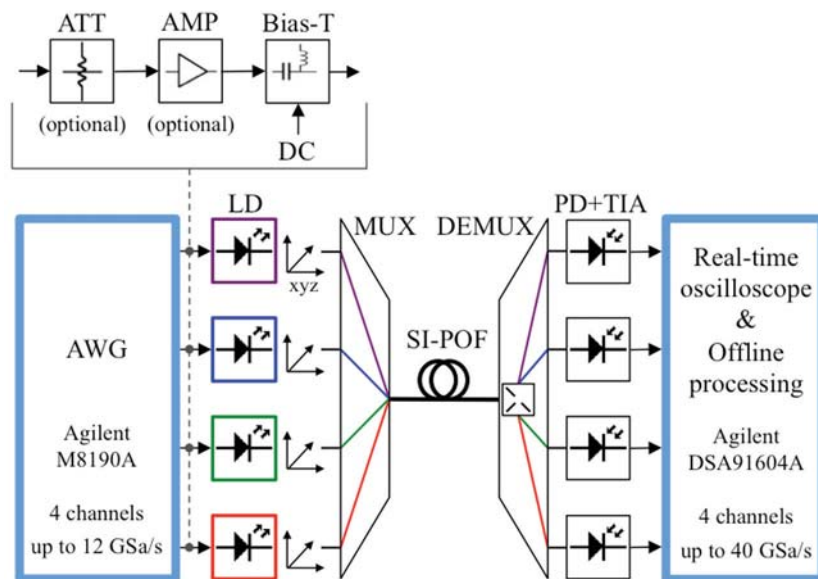


Fig. 5.5: Experimental setup for the measurements employing NRZ modulation and offline-processed FFE: ATT – attenuator; AMP – amplifier; DC – direct current.

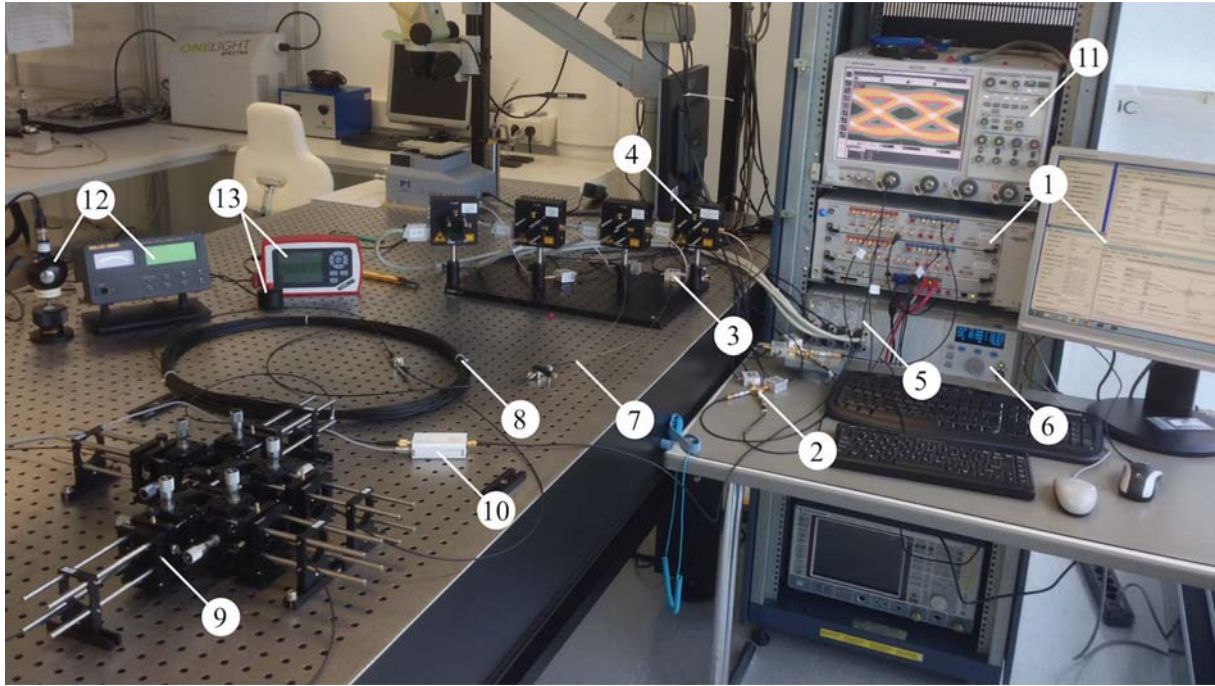


Fig. 5.6: Experimental setup for investigating four-channel high-speed POF WDM transmission: 1 – Agilent M8190A AWG; 2 – attenuator and MERA-556+ wideband amplifier; 3 – bias-tee; 4 – Thorlabs TCLDM temperature controlled laser diode mount; 5 – Thorlabs ITC8022 module; 6 – Thorlabs PRO8000 modular chassis; 7 – four-legged multiplexing POF bundle; 8 – SI-POF link; 9 – four-channel interference filter-based demultiplexer; 10 – Graviton SPD-2 receiver; 11 – Agilent DSA91604A real-time oscilloscope; 12 – Melles Griot universal optical power meter with 13 PDH 005 integrating sphere; 13 – Thorlabs PM100D power meter with S140C integrating sphere.

To multiplex the signals from four laser diodes onto the SI-POF link, a four-legged POF bundle was used. The basic idea leading to the development of such a bundle was to utilize the benefit of a large core diameter of SI-POF. As indicated in Fig. 5.7a, four fibers with $400\ \mu\text{m}$ cladding diameter, that are arranged in a formation with $970\ \mu\text{m}$ outer diameter, can be completely covered by $980\ \mu\text{m}$ core of SI-POF. The principle of operation of the POF bundle as a multiplexer is shown in Fig. 5.7b. At the input side, $400\ \mu\text{m}$ fibers are separated and guided to the spatially distributed laser diodes. On the opposite side, $400\ \mu\text{m}$ fibers are joined in a bundle with their end faces aligned in the same plane. A multiplexing interface is formed by positioning the fiber bundle against $1\ \text{mm}$ SI-POF.

For realization of the bundle an Asahi KASEI DB-400 PMMA SI-POF with $400\ \mu\text{m}$ cladding diameter and $\text{NA}=0.5$ was used. Four $60\ \text{cm}$ long fibers were terminated at the input side with $400\ \mu\text{m}$ FC connectors. The opposite ends of the fibers were joined together and glued inside $970\ \mu\text{m}$ FC connector to form the fiber bundle (Fig. 5.7c). As illustrated in Fig. 5.7d, an FC connector-mating sleeve was used to bring together and align the bundle and the input of the SI-POF link, thereby forming the multiplexing interface. An index-matching gel was applied between the connectors to reduce the losses.

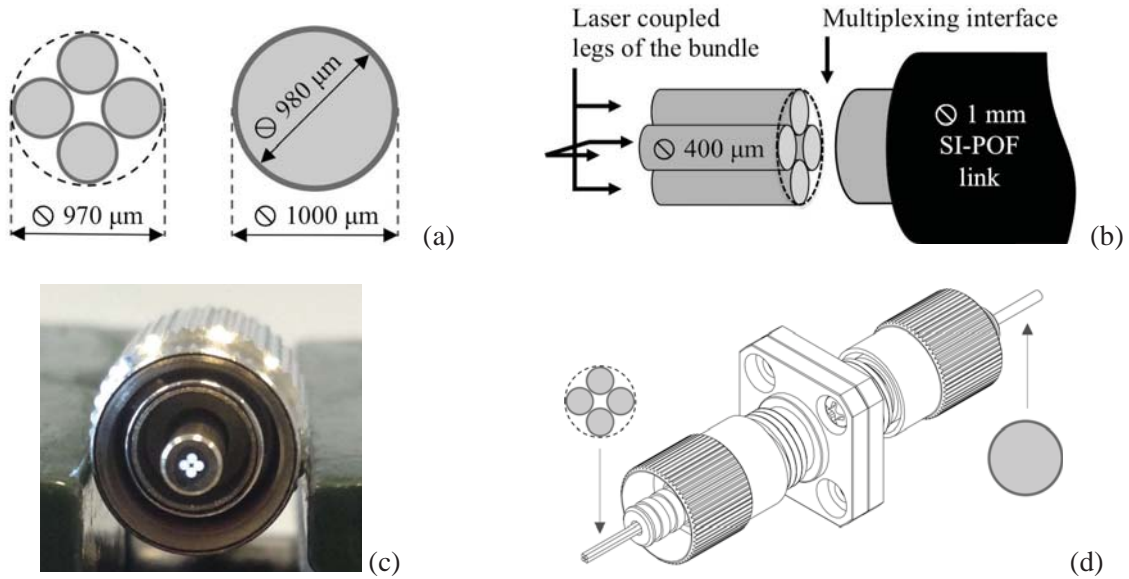


Fig. 5.7: Four-legged multiplexing POF bundle: (a) cross sections of four 400 μm cladding diameter fibers arranged within a circle with 970 μm diameter (left) and of 980/1000 μm SI-POF (right); (b) principle of operation of the POF bundle as a multiplexer; (c) four 400 μm fibers glued within 970 μm FC connector; (d) formation of a multiplexing interface with the POF bundle aligned against the SI-POF link using an FC connector mating sleeve.

The optical power loss at the transmitter side comprised the laser diode-to-400 μm fiber launching coupling loss, the attenuation of 60 cm long bundle leg, and the loss of the multiplexing interface. As shown in Table 5.5, for direct launching with 405 nm (DL-7146-101S), 450 nm, 520 nm and 656 nm laser diodes the total loss ranged between 3.3 dB and 5.5 dB. Even though the launching coupling loss was higher than for 1 mm POF (see Table 5.3 and Fig. 5.8), a significant improvement compared to the fused POF coupler was achieved due to the low loss (< 1 dB) of the multiplexing interface.

Table 5.5: Optical power loss at the transmitter side when using four-legged POF bundle.

Operating wavelength [nm]	405	450	520	639
Laser diode-to-400 μm fiber launching loss + attenuation of a bundle leg [dB]	4.06	2.63	2.82	4.76
Connector loss (with index matching gel) [dB]	0.87	0.98	0.52	0.77
Total loss [dB]	4.93	3.61	3.34	5.53

The described multiplexing solution was first shown in [Jončić13c]. Shortly before, the patent application for an optical POF multiplexer based on a multi-legged POF bundle, which referred to arbitrary channel counts and fiber diameters, was submitted to the German Patent and Trade Mark Office (DPMA) under number DE 10 2013 020 236.1. A similar approach was later adopted in [Kruglov14] and [Pinzon14] to realize the low loss seven-legged and three-legged multiplexers respectively. Because of the simplicity and effectiveness of the

approach, further investigation on multiplexing technique using multi-legged POF bundles is recommended.

The AWG simultaneously generated four independent NRZ data streams based on 2^7-1 PRBS with the maximum sampling rate. The received electrical signals were acquired by the real-time oscilloscope with 8-bit vertical resolution and oversampling. The digital receiver equalization was carried out in the offline mode. For that purpose the oscilloscope's built-in Serial Data Equalization software was used [Agilent09].

In order to determine how many FFE taps to use, a trial-and-error approach was applied. The number of taps was initially set to a low value (e.g. two), and the optimization procedure was run on the oscilloscope to determine the tap values. If the values of the higher taps were significant, the tap count was increased by one and the optimization algorithm was run again. If the values of the higher taps were close to zero, that meant that their contribution to the equalizer's output would be insignificant and that they were unnecessary. The trial-and-error approach was also applied to determine the optimal tap delay, i.e. if one or more taps per bit had to be used. To prevent the equalizer from amplifying the noise components at higher frequencies where the energy content of useful signal was low, the bandwidth of the oscilloscope was set to the value in GHz corresponding to one half of the data rate in Gb/s. A phase-locked loop was used to extract the clock from the equalized data.

The eye diagram of an equalized waveform was displayed on the oscilloscope's screen for further analysis. The oscilloscope's built-in software EZJIT Complete was used to estimate the corresponding Q-factor [Agilent13]. Thereby, only a small time window (2 % of the unit interval) in the middle of the equalized eye diagram was taken into consideration. The BER value was then calculated using Equation 2.15.

5.2.2 Measurement results and discussion

7.8 Gb/s transmission over 50 m SI-POF

The WDM channels based on 405 nm (DL-7146-101S), 450 nm, 515 nm and 639 nm laser diodes were employed in this transmission experiment. To maximize the modulating signal amplitude and thereby improve the SNR of the received signal, the optical output power of each laser diode was adjusted to its maximal possible value. For 405 nm, 450 nm and 515 nm devices the operating point was set to comply with the upper limit of the receiver's dynamic range. The 639 nm device was driven with the maximum recommended forward current. The respective used bias currents were 70 mA, 40 mA, 61 mA and 43 mA. The optical powers coupled into the SI-POF link and the received optical powers measured after the demultiplexer are given in Table 5.6. All diodes were driven in their linear lasing region, as indicated in Fig. 5.8 for a P-I curve of 405 nm device. The 1 V_{pp} output amplitude of the AWG was sufficient to modulate 450 nm, 515 nm and 639 nm laser diodes with the modulation index of approx. 0.9. The signal in 405 nm channel was additionally amplified to achieve the same modulation index, as indicated in Fig. 5.5. For the amplification, a MERA-

556+ wideband amplifier (20.5 dB gain at 0.1 GHz) was used in combination with 10 dB attenuator to avoid amplifier nonlinearities (18 dBm output power @ 1 dB compression point at 0.1 GHz).

Table 5.6: Optical power levels along 50 m SI-POF link (NRZ+FFE).

Operating wavelength [nm]	405	450	515	639
Fiber-coupled power [dBm]	11.54	7.63	5.17	8.06
Received power [dBm]	0.67	-0.51	-1.76	-6.40

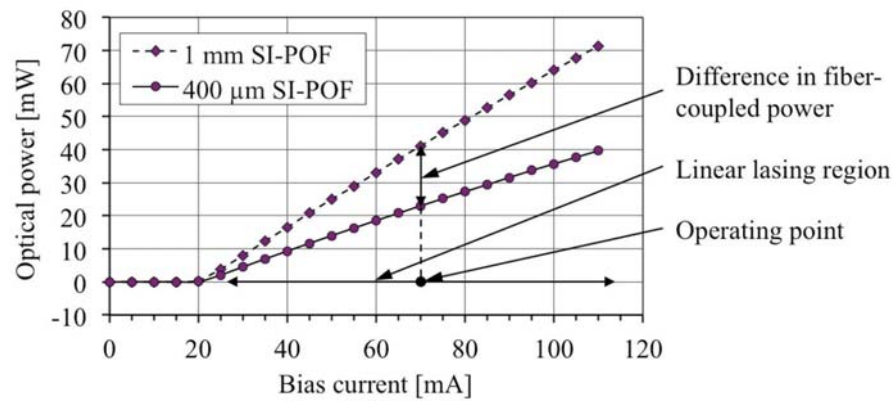


Fig. 5.8: Optical power coupled into 1 mm SI-POF and 400 μm SI-POF when direct launching with 405 nm (DL-7146-101S) laser diode.

The maximum transmission rates achieved in the individual channels were 1.7 Gb/s (405 nm channel), 1.9 Gb/s (450 nm channel), 2.2 Gb/s (515 nm channel) and 2 Gb/s (639 nm channel). Thereby, six FFE taps with the tap delay equal to one half of the corresponding bit period were used in each of the channels. The transmission parameters for the individual channels are listed in Table 5.7. The resulting eye diagrams are represented in Fig. 5.9. A total of 7.8 Gb/s were transmitted over 50 m SI-POF at the $\text{BER} < 10^{-5}$. After deduction of 3.2% redundant bits required for Reed-Solomon (255,247) FEC, a net bit rate of 7.56 Gb/s was obtained. Compared to the record capacity of a single-channel system over the same fiber length [Vinogradov11], an improvement of 1.67 Gb/s was achieved.

Table 5.7: Transmission parameters for 50 m SI-POF link at an aggregate bit rate of 7.8 Gb/s.

Operating wavelength [nm]	405	450	515	639
Bit rate [Gb/s]	1.7	1.9	2.2	2
Q-factor	5.06	4.67	4.96	4.76
BER	$2.10 \cdot 10^{-7}$	$1.51 \cdot 10^{-6}$	$3.52 \cdot 10^{-7}$	$9.68 \cdot 10^{-7}$

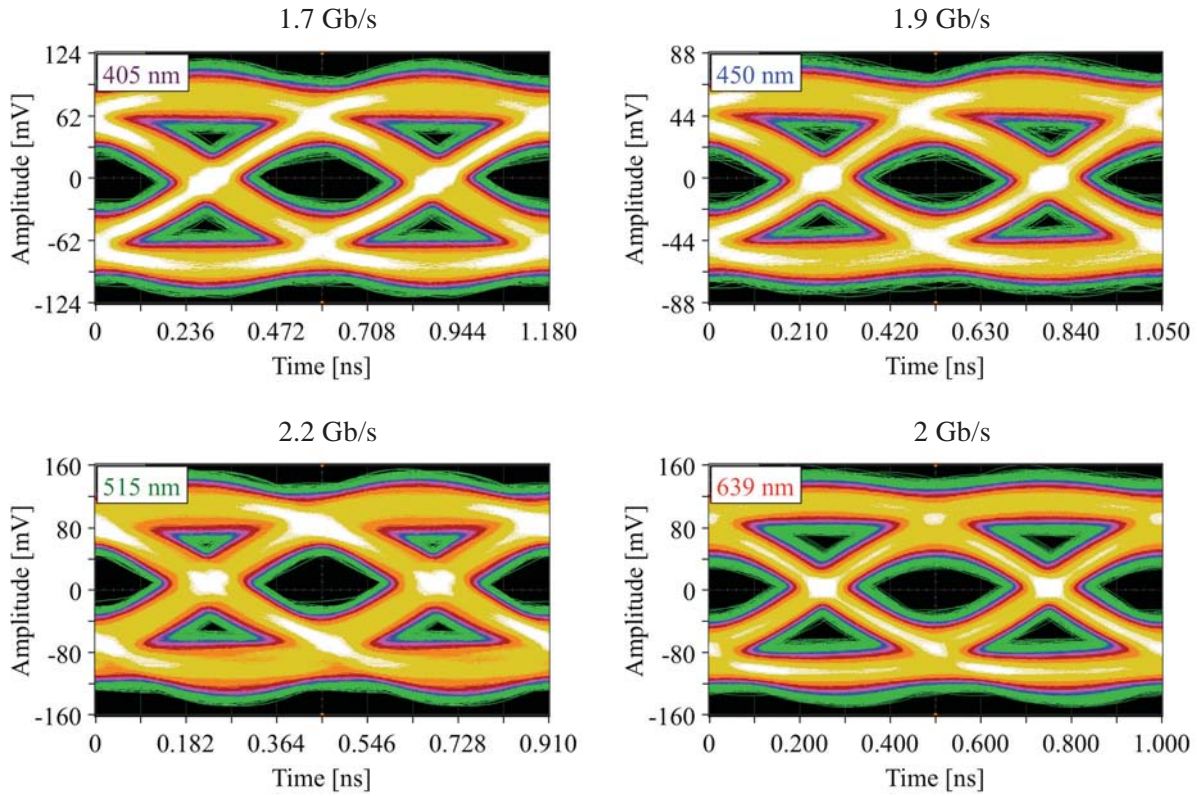


Fig. 5.9: Eye diagrams for 50 m SI-POF link at an aggregate bit rate of 7.8 Gb/s.

3.21 Gb/s transmission over 100 m SI-POF

In this experiment the same laser diodes like in the previous measurement were employed. The operating point of 405 nm device was adjusted to accompany the maximum allowed output amplitude of the MERA-556+ amplifier. The optical output power in 450 nm and 515 nm channels was limited by the saturation power of the Graviton SPD-2 receiver. The device in 639 nm channel was driven with the recommended bias current. Correspondingly, the utilized bias currents were 95 mA, 68 mA, 86 mA and 43 mA. The optical powers coupled into the SI-POF link and the received optical powers measured after the demultiplexer are shown in Table 5.8. The laser diodes were directly modulated in their linear lasing region with the modulation index of approx. 0.9. To reach high modulation index for the applied bias currents, the outputs of the AWG for 405 nm, 450 nm and 515 nm channels were additionally amplified in the same manner as in 50 m experiment.

The data rates achieved in the individual channels employing six FFE taps with the tap delay equal to one half of the corresponding bit period were 0.6 Gb/s (405 nm channel), 1 Gb/s (450 nm channel), 1.3 Gb/s (515 nm channel) and 0.31 Gb/s (639 nm channel). The

Table 5.8: Optical power levels along 100 m SI-POF link (NRZ+FFE).

Operating wavelength [nm]	405	450	515	639
Fiber-coupled power [dBm]	13.08	11.99	8.71	8.06
Received power [dBm]	-5.40	-0.76	-2.13	-18.74

transmission parameters and the resulting eye diagrams in the individual channels are shown in Table 5.9 and Fig. 5.10 respectively. An aggregate bit rate of 3.21 Gb/s was transmitted over 100 m SI-POF at the $\text{BER} < 10^{-4}$. Considering 3.2% overhead required for Reed-Solomon (255,247) FEC, an information bit rate of 3.11 Gb/s was achieved ($\text{BER} < 10^{-9}$). That was 0.82 Gb/s less than the record single-channel capacity over the same link length, which was achieved with an offline processed DFE implemented through a custom Matlab program [Vinogradov11].

Considering the long memory of SI-POF channel, a 3-bit memory of the equalizer associated with the current and two previous bits, could not optimally compensate for the ISI introduced by the channel [Zeola11]. As a consequence, the transmission rates in both experiments were impaired. However, for any further increase of the equalizer's memory (tap count) or data rate, the optimization algorithm could not calculate the tap values that would open the eye. Having the software implementation of the equalizer beyond the scope of this thesis, a recommendation for further work would be to investigate the equalizer's implementation, and

Table 5.9: Transmission parameters for 100 m SI-POF link at an aggregate bit rate of 3.21 Gb/s.

Operating wavelength [nm]	405	450	515	639
Bit rate [Gb/s]	0.6	1	1.3	0.31
Q-factor	4.19	4.53	4.22	4.21
BER	$1.39 \cdot 10^{-5}$	$2.95 \cdot 10^{-6}$	$1.22 \cdot 10^{-5}$	$1.28 \cdot 10^{-5}$

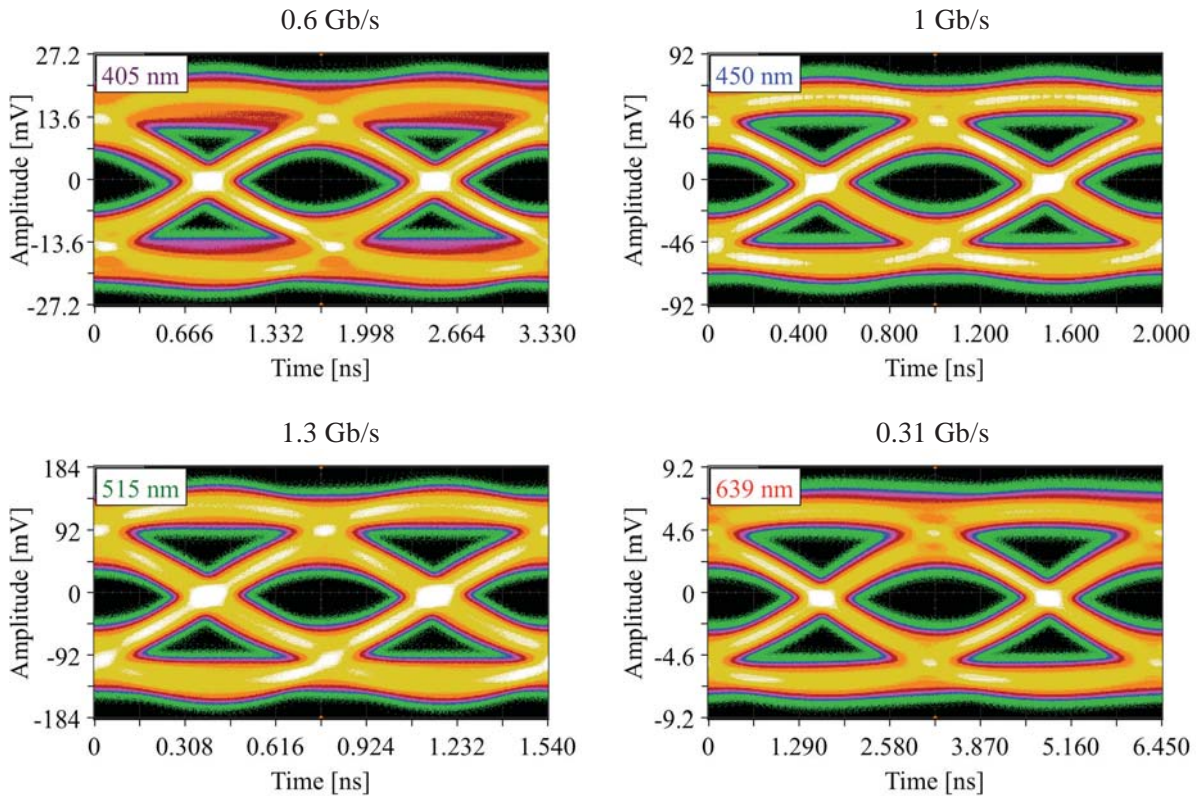


Fig. 5.10: Eye diagrams for 100 m SI-POF link at an aggregate bit rate of 3.21 Gb/s.

determine how the data rate can be maximized by using the Serial Data Equalization software. Furthermore, a more complex non-linear DFE equalization, which is typically employed in POF systems and gives better results than FFE, e.g. [Loquai13], should be implemented through the oscilloscope's equalization software for further data rate increase.

The performed experiments demonstrated that POF WDM with lower channel rates and simple transmission technique could provide aggregate bit rates comparable to those achieved with the single-wavelength systems that used more advanced transmission techniques (e.g. DMT or NRZ/pulse amplitude modulation (PAM) combined with DFE) but required more signal processing. Therefore, another important point for further work would be to investigate possible advantages (e.g. lower latency) of WDM transmission with lower channel rates over fast single-channel transmission.

5.3 WDM transmission employing DMT modulation

To maximize the spectral efficiency of the signals transmitted within four optical channels, the DMT modulation technique was applied [Lee09a]. As already described in subsection 2.3.2, the DMT is a multicarrier modulation scheme based on parallel transmission of a large number of low-speed subcarriers with QAM modulation. The record 14.77 Gb/s and 8.26 Gb/s data rates employing the offline-processed DMT modulation were achieved over 50 m and 100 m SI-POF, respectively, at the $\text{BER}=10^{-3}$. The results of 50 m experiment were published in IEEE Photonics Technology Letters in July 2014 [Jončić14b]. The results of the experiment over 100 m link were presented at the ICPOF 2014 [Jončić14c].

The WDM experiments employing the offline-processed DMT modulation were realized through the cooperation with Dr.-Ing. Roman Kruglov from the POF-AC. The digital signal processing (pre-computation, modulation and demodulation of the pilot and real DMT signals, implementation of the Chow's rate adaptive bit-loading algorithm, SNR estimation and BER calculation, plotting of the constellation diagrams) was performed by Dr. Kruglov using a custom Matlab program.

5.3.1 Experimental setup

The experimental setup for the measurements employing the offline-processed DMT modulation is shown in Fig. 5.11. It comprised the four-channel Agilent M8190A AWG, four butt-coupled edge-emitting laser diodes, four-legged multiplexing POF bundle, SI-POF link of two different lengths, interference-based POF demultiplexer, optical receivers, four-channel Agilent DSA91604A real-time oscilloscope and computer with a software for offline signal processing. The photo of the general experimental setup is already shown in Fig. 5.6.

The four-channel AWG with 12-bit vertical resolution was used to generate the DMT signals transmitted within four optical WDM channels. The signals were constructed on the basis of $2^{15}-1$ PRBS and included up to 256 subcarriers with constant subcarrier spacing. The

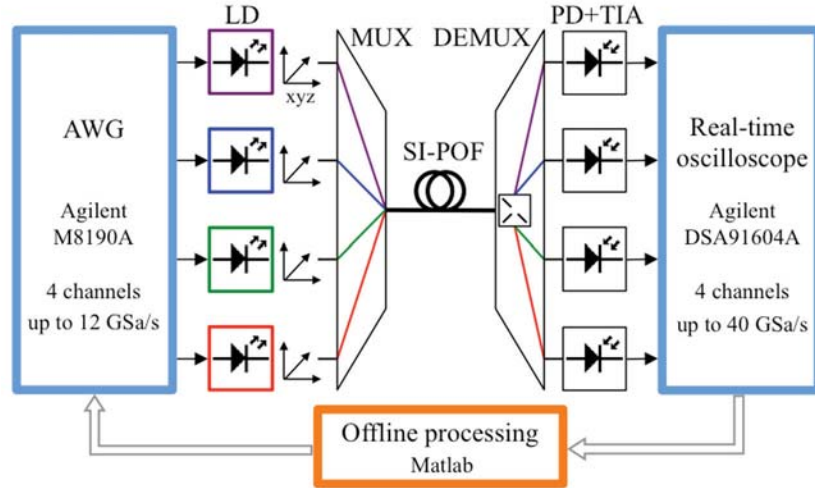


Fig. 5.11: Experimental setup for the measurements employing offline-processed DMT modulation.

sampling rate of the AWG was set to the value four times higher than the maximum frequency of the transmitted DMT signal, corresponding to the oversampling factor of 2. Oversampling was necessary for two reasons. First, to minimize amplitude distortions of the generated signals caused by $\sin(x)/x$ frequency response of the digital-to-analog converter of the AWG, which has the first null of the spectrum at the sampling frequency. Second, to facilitate digital filtering of the received baseband DMT signal from high-frequency spectral images aliased by the AWG's digital-to-analog converter.

To optimally transmit the DMT signal, which may have instantaneous peak occurring when the subcarriers add up constructively, its dynamic range had to be reduced [Lee09a]. Therefore, the value of the crest factor after clipping, defined as the ratio of the maximum allowed signal amplitude to the root-mean-square amplitude of the original signal, was limited to 3. To resist to the ISI, a cyclic prefix of 3.125% was added as a guard interval at the beginning of each DMT frame.

The received electrical waveforms were acquired by the real-time oscilloscope with 8-bit nominal resolution. To facilitate phase recovering and enhance the effective resolution of the oscilloscope, the DMT signals were captured with additional oversampling. The subsequent offline processing and BER counting were performed on the computer.

To estimate the quality of the WDM channels and allocate the number of bits per subcarrier, four DMT pilot signals with 256 subcarriers, each loaded with 16-QAM, were simultaneously transmitted over four channels. In 50 m and 100 m experiments the bandwidth occupied by the pilot signals was initially set to 1 GHz and 500 MHz respectively. To decorrelate the signals that modulated the laser diodes, an additional delay of 10 ns between the channels was introduced in the AWG. The received signals were demodulated and used to evaluate the SNR per subchannel. For the case the SNR in the highest subchannels was high enough to allow transmission of additional bits at even higher subcarrier frequencies (like in Fig. 5.12c), the bandwidth of the pilot signal was accordingly increased and the measurement was repeated.

The evaluated SNR per subchannel was used as input to the Chow's rate adaptive bit-loading algorithm that computed the appropriate bit-loading scheme and power allocation per subchannel [Chow95]. Based on the obtained bit and power allocations across the subcarriers, the real-valued samples of the DMT time signal were pre-computed offline. After that, the DMT samples were loaded into the memory of the AWG and repeatedly played in order to create a continuous-time DMT signal that directly modulated the intensity of the laser diode. The received DMT frames were captured by the oscilloscope for subsequent offline processing that comprised DMT demodulation, SNR evaluation and BER counting.

5.3.2 Measurement results and discussion

14.77 Gb/s transmission over 50 m SI-POF

For transmission over four different wavelengths 405 nm (DL-7146-101S), 450 nm, 515 nm and 639 nm laser diodes were employed. To achieve a better performance of the link, the operating point of 405 nm, 450 nm and 515 nm devices was adjusted to its possibly maximum value according to the dynamic range of the corresponding receiver. The operating bias current of 639 nm laser diode corresponded to the recommended value. Accordingly, the respective utilized bias currents were 80 mA, 50 mA, 60 mA and 40 mA. The laser diodes were operated in their linear lasing regions with the modulation index of approx. 0.9. The output amplitude of the AWG of up to 1 V_{pp} was sufficient to modulate the diodes in 515 nm and 639 nm channels. High modulation index in 405 nm and 450 nm channels was achieved by employing additional MERA-556+ wideband amplifiers (20.5 dB gain at 0.1 GHz) in combination with 10 dB attenuators to avoid amplifier nonlinearities (18 dBm output power @ 1 dB compression point at 0.1 GHz).

An optical receiver based on Ø 800 µm HAMAMATSU S5052 silicon PIN photodiode followed by a commercially available transimpedance amplifier [Vinogradov05] was provided by the POF-AC for this particular measurement. It was used in 405 nm and 450 nm spectral channels. The maximum optical power providing a proper signal at the receiver output was approx. 0 dBm at 650 nm. The Graviton SPD-2 receiver was used in 515 nm and 639 nm channels. The reason for using two receiver models was that in the shorter wavelength channels the [Vinogradov05] receiver supported higher data rates than the Graviton receiver because of its better responsivity and higher saturation power. The optical powers coupled into the SI-POF link and the received optical powers measured after the demultiplexer are given in Table 5.10.

Table 5.10: Optical power levels along 50 m SI-POF link (DMT).

Operating wavelength [nm]	405	450	515	639
Fiber-coupled power [dBm]	11.79	9.12	5.01	7.96
Received power [dBm]	0.82	1.00	-1.93	-7.04



The transmitted DMT pilot signals occupied the bandwidth of 1 GHz, implying 3.9 MHz subcarrier spacing. Accordingly, the sampling rate of the AWG was set to 4 GS/s. The received signals were acquired with the sampling rate of 20 GS/s, corresponding to 10 times oversampling. The SNR before bit-loading and the bit-loading schemes obtained on the basis of Chow's rate adaptive bit-loading algorithm for four WDM channels are shown in Fig. 5.12. The variation of the SNR between the spectral channels was caused by the difference in channel frequency response, attenuation of the optical link, slope efficiency of the laser diodes and responsivity of the receivers, which all depend on wavelength and/or used components. Since the frequency response of SI-POF can be considered constant over the wavelength channels, the frequency response variations between the channels were primarily caused by different responses of employed transmitters and receivers. The attenuation of the optical link comprised the wavelength-dependent fiber attenuation and IL of multiplexer and demultiplexer. The SNR degradation in the lowest subchannels of 405 nm and 450 nm channels was presumably caused by an increased low cutoff frequency of the transimpedance amplifier of the [Vinogradov05] receiver. In two other channels the SNR degradation in the lowest subchannels may have been caused by a number of other factors such as poor electrical contact between the mated connectors or poor soldering joints of the laser diodes. Too high modulation index or the saturation of receiver can be excluded on the grounds that in 100 m experiment, where even higher modulation index was used, such SNR degradation was not present.

After deduction of the DMT transmission overhead, the data rates transmitted in the individual WDM channels were 3.26 Gb/s (405 nm channel), 3.90 Gb/s (450 nm channel), 4.08 Gb/s (515 nm channel) and 3.53 Gb/s (639 nm channel). The total averaged BER in each channel was 10^{-3} allowing the FEC with 7% overhead. Therefore, an aggregate bit rate of 14.77 Gb/s achieved at the $\text{BER}=10^{-3}$ corresponded to 13.8 Gb/s information bits at the $\text{BER}<10^{-9}$. The realized system provided 2.3 times more capacity than the fastest 50 m single-wavelength system known from literature, which operated at 650 nm [Vinogradov11].

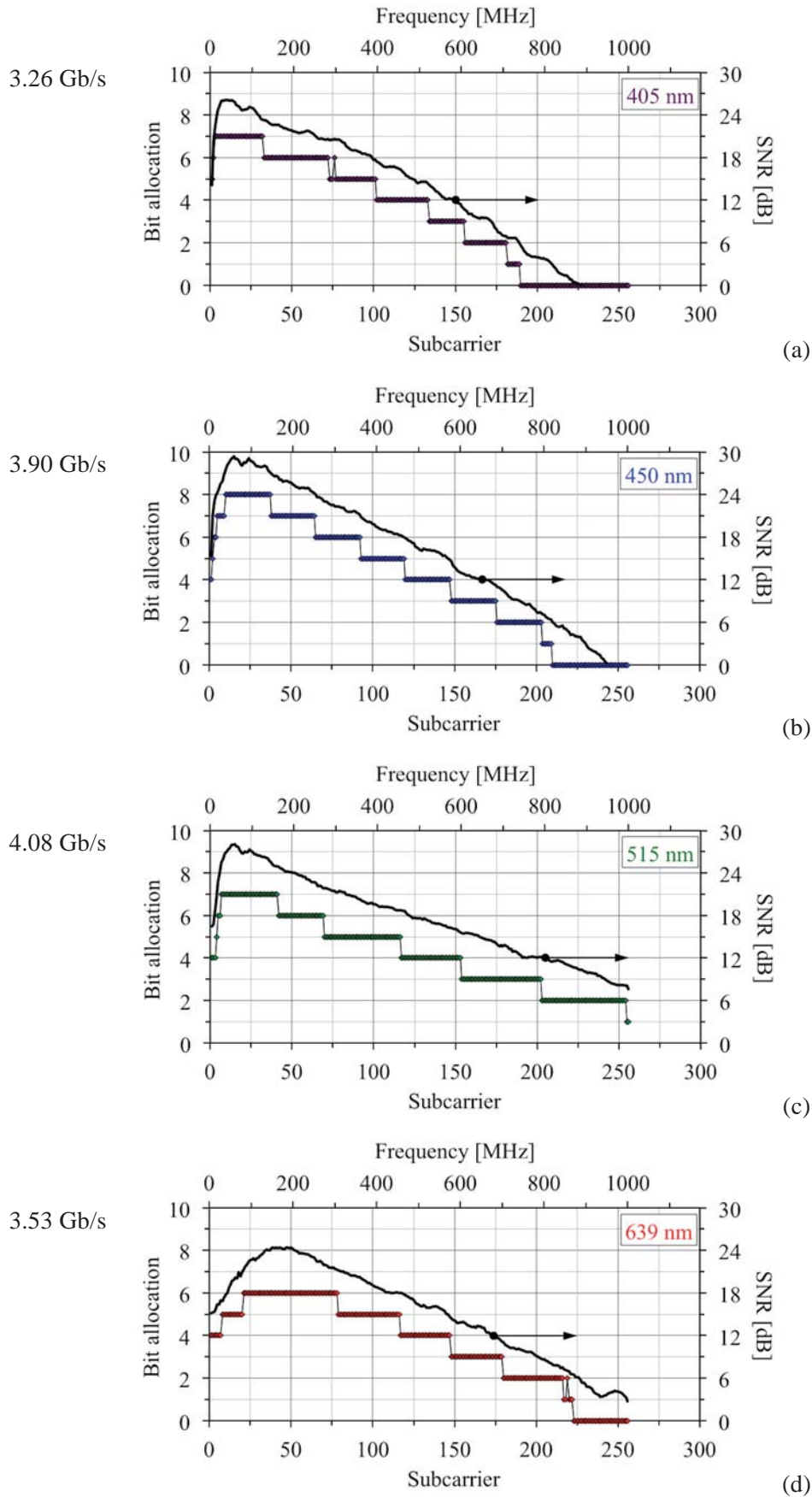


Fig. 5.12: Measured SNR per subcarrier before bit-loading (solid black curve) and bit-loading scheme obtained on the basis of Chow's rate adaptive bit-loading algorithm (curve with colored markers) for (a) 405 nm, (b) 450 nm, (c) 515 nm and (d) 639 nm channel in 50 m experiment.

As an illustration of quality of the received signals, two superimposed constellation diagrams obtained after DMT demodulation in the fastest 515 nm channel are shown in Fig. 5.13. The highest constellation corresponding to 128-QAM is represented in Fig. 5.13a. The 7th to 41st subcarrier, experiencing the best SNR, was modulated with 128-QAM. That implied a 7-bit allocation. A superimposed constellation diagram of the subcarrier group modulated with 4-QAM (203rd to 254th subcarrier, 2 bits assigned to each subcarrier) is shown in Fig. 5.13b.



Fig. 5.13: Superimposed received constellations in 515 nm channel for the subcarrier groups modulated with (a) 128-QAM (7th to 41st subcarrier) and (b) 4-QAM (203rd to 254th subcarrier).

8.26 Gb/s transmission over 100 m SI-POF

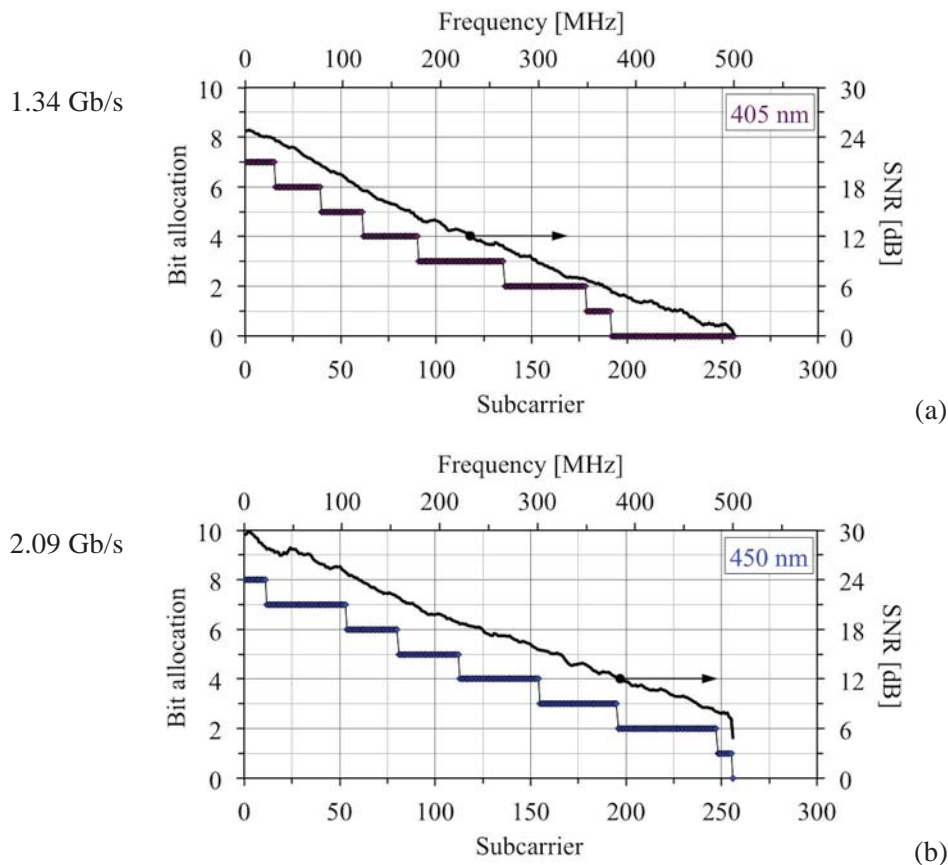
In this experiment the brand-new samples of the laser diodes operating at 405 nm (DL-7146-101S), 450 nm, 520 nm and 656 nm were employed as WDM transmitters. The Graviton SPD-2 receiver was used for detection. To achieve a better frequency response of 450 nm and 520 nm devices, their operating point was adjusted to a higher value [Kruglov12b], thereby exceeding the maximum optical power for a proper signal at the receiver output. To reduce the received power, a longitudinal offset of the outgoing fiber end face was introduced in the demultiplexer output port 2 and 3. In the corresponding channels the offset caused an additional attenuation of 0.8 dB and 1.2 dB, providing that the received optical power was below the receiver's saturation level of -0.32 dB and -1.65 dB respectively. The operating bias current of 656 nm laser diode corresponded to the recommended value. To accompany the maximum amplifier's output amplitude, the operating point of 405 nm device was set to 70 mA. The respective utilized bias currents were 70 mA, 50 mA, 60 mA and 65 mA. The laser diodes were directly modulated in their linear lasing region with the modulation index of approx. 0.95. High modulation index was achieved by amplifying the AWG's output signals with MERA-556+ wideband amplifiers combined with 6-10 dB attenuators to avoid amplifier nonlinearities. The optical powers coupled into the SI-POF link and the received optical powers measured after the demultiplexer are given in Table 5.11.

Table 5.11: Optical power levels along 100 m SI-POF link (DMT).

Operating wavelength [nm]	405	450	520	656
Fiber-coupled power [dBm]	12.85	11.80	9.09	9.90
Received power [dBm]	-4.40	-0.88	-1.83	-9.03
SI-POF link attenuation [dB]	12	7.5	5.8	15

The transmitted DMT pilot signals occupied the bandwidth of 500 MHz (405 nm, 450 nm and 656 nm channel) and 700 MHz (520 nm channel), implying 1.95 MHz and 2.73 MHz subcarrier spacing respectively. The corresponding sampling rates of the AWG were 2 GS/s and 2.8 GS/s. The received electrical waveforms were oversampled with 10 GS/s. The SNR before bit-loading and the bit-loading schemes obtained on the basis of Chow's rate adaptive bit-loading algorithm for four WDM channels are shown in Fig. 5.14. The maximum SNR of approx. 30 dB in both 50 m and 100 m measurements was not limited by the transmission system, but rather by the DMT signal itself due to the clipping noise [Lee09a].

After deduction of the DMT transmission overhead, the data rates transmitted in the individual channels were 1.34 Gb/s (405 nm channel), 2.09 Gb/s (450 nm channel), 2.84 Gb/s (520 nm channel) and 1.99 Gb/s (656 nm channel). The total averaged BER in each channel was calculated to be 10^{-3} , which was sufficient to achieve $\text{BER} < 10^{-9}$ after applying FEC with 7 % redundancy. Hence, an aggregate bit rate of 8.26 Gb/s realized at the $\text{BER} = 10^{-3}$ contained 7.72 Gb/s information bits. The system provided 2 times more transmission capacity than the fastest 100 m single-channel system known from literature, which operated at 514 nm [Vinogradov11].



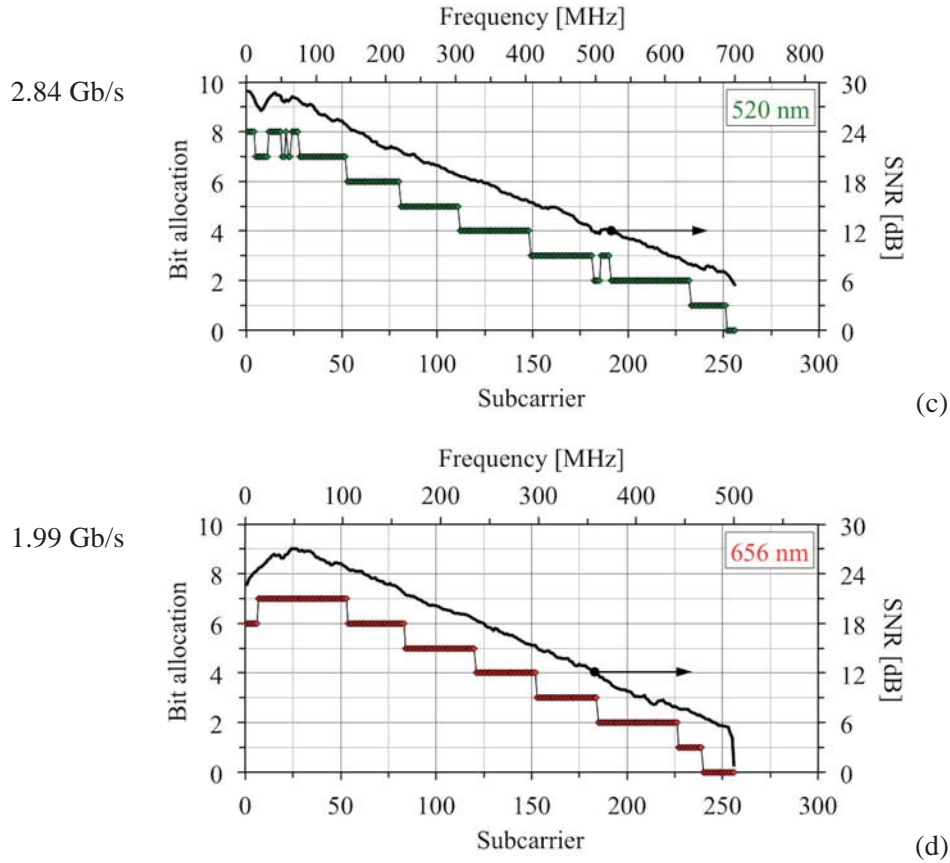


Fig. 5.14: Measured SNR per subcarrier before bit-loading (solid black curve) and bit-loading scheme obtained on the basis of Chow's rate adaptive bit-loading algorithm (curve with colored markers) for (a) 405 nm, (b) 450 nm, (c) 520 nm and (d) 656 nm channel in 100 m experiment.

The power allocation per subchannel for 520 nm channel, that was obtained on the basis of Chow's algorithm, is shown in Fig. 5.15. The saw-tooth-shaped power mask with approx. 3 dB peak-to-peak deviation is characteristic for the Chow's algorithm [Chow95] and has to be applied to the transmitted subchannels of a real DMT signal. Thereby, within the same subcarrier group the lower subchannels, typically experiencing better SNR before the bit loading, are allocated with less power than the higher subchannels experiencing worse SNR.

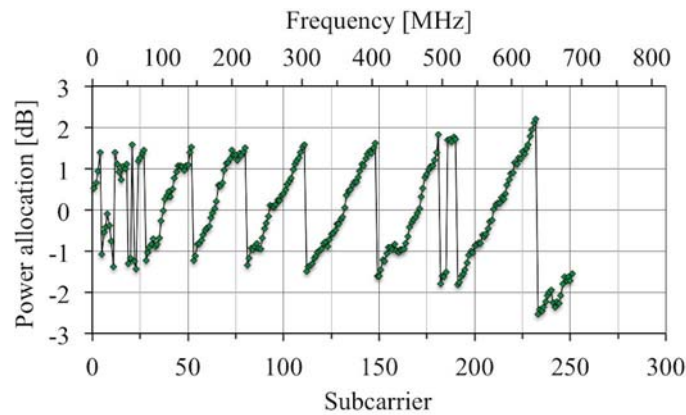


Fig. 5.15: Power allocation obtained on the basis of Chow's rate adaptive bit-loading algorithm for 520 nm channel.

The SNR per subchannel of the received DMT signal in 520 nm channel after applying the bit-loading algorithm is shown in Fig. 5.16a. A stepped SNR curve can clearly be recognized. Each step corresponds to the subcarrier group with the same constellation size. Due to the saw-tooth shaped power allocation, the received SNR after bit loading is almost constant within each subcarrier group, which should also result in the same BER performance.

The BER per subchannel for 520 nm channel is shown in Fig. 5.16b, resulting in the total averaged BER of 10^{-3} . That value was computed by averaging the BER per subchannel over all active subcarriers, which amounted 251 in the particular case. Thereby, each individual BER was weighted based on the number of bits assigned to that subcarrier. That explains how a lower-weighted BER (typically greater than 10^{-3}) of a larger number of higher subchannels was compensated by a higher-weighted BER (typically less than 10^{-3}) in a smaller number of lower subchannels to result in the total averaged value of 10^{-3} .

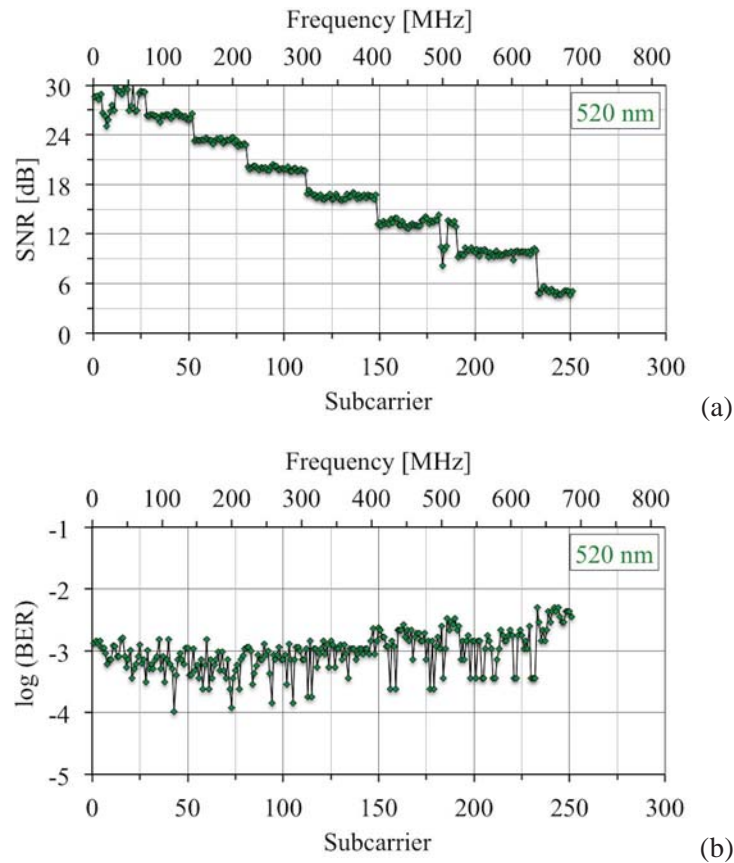


Fig. 5.16: Properties of the received real DMT signal in 520 nm channel: (a) SNR per subchannel after bit-loading; (b) BER values per subchannel resulting in the total averaged BER of 10^{-3} .

The superimposed constellation diagrams with clearly distinguishable signal points, obtained after DMT demodulation in the fastest 520 nm channel, are shown in Fig. 5.17 to indicate the quality of the received signal. Fig. 5.17a depicts the highest received constellation employing 256-QAM. Due to the insufficient SNR only 16 out of 27 lowest subcarriers were modulated with 256-QAM, implying that 8 bits were assigned to each of those subcarriers. Fig. 5.17b represents a superimposed constellation diagram of the subcarrier group modulated with

4-QAM (182nd to 185th and 191st to 232nd subcarrier). An averaged received SNR for the subcarrier groups modulated with 256-QAM and 4-QAM, obtained from the measurement data from Fig. 5.16a, equals 29.22 dB and 9.76 dB respectively.



Fig. 5.17: Superimposed received constellations in 520 nm channel for the subcarrier groups modulated with (a) 256-QAM (16 out of 27 lowest subcarriers) and (b) 4-QAM (182nd to 185th and 191st to 232nd subcarrier).

5.4 Discussion

Together with a three-channel and a six-channel WDM experiment from [Kruglov12a] and [Kruglov14] respectively, the performed measurements demonstrated not only the feasibility but also the potential of a high-speed POF WDM concept, offering more than two times higher transmission capacity compared to the single-wavelength systems.

Having the measurement results already discussed in the previous sections, this subchapter summarizes the recommendations for further research and outlines the possible capacity of POF WDM. The recommendations can be summarized as follows:

- Because of the simplicity and effectiveness of multiplexing based on the multi-legged POF bundles, a further investigation on that multiplexing technique is recommended.
- Another important point for further work would be to investigate whether POF WDM with simple transmission techniques and at the same aggregate data rate offers advantages over single-channel transmission that employs more advanced transmission techniques but requires more signal processing. In particular, there might be applications (e.g. where low latency is required) where parallel WDM transmission with lower data rates per channel may be more beneficial than fast single-channel transmission.
- Further optimization of both the demultiplexer to provide lower IL (see subchapter 3.6), and of the transmission system and DMT signal parameters is required to further increase the aggregate WDM data rates:
 - With a four-channel WDM system an aggregate data rate of 16.05 Gb/s at the $\text{BER}=10^{-3}$ could probably be achieved over 50 m SI-POF. That would correspond to 15 Gb/s error free transmission. An aggregate data rate of 9.35 Gb/s could presumably be reached over 100 m link, resulting in 9 Gb/s information bits.

- With the available transceiver components and a properly designed eight-channel interference filter-based demultiplexer with three-stage configuration, a possible aggregate data rate over 50 m SI-POF would be 32.1 Gb/s at the $\text{BER}=10^{-3}$. That would correspond to an information rate of 30 Gb/s (in average 3.75 Gb/s per WDM channel).

Supported by the technological advancements related to the capacity increase of a single channel, POF WDM might represent a networking solution offering both the advantage of a robust and easy-to-install transmission medium, and of a high-speed data communication. That might open up the possibilities for SI-POF technology to be used in the next generation broadband in-house networks and in high-speed very short reach optical interconnection networks (e.g. in data centers, and for inter-rack or inter-board interconnections).

6 Spectral grids in the visible spectrum for POF WDM applications

Besides developing low-IL cost-effective POF WDM components and fast POF WDM transmission systems, it is also important to allocate a unique set of WDM transmission channels in the visible spectrum to support WDM applications over SI-POF. This chapter investigates spectral grids for today's and future POF WDM systems. The results of the investigation were partially presented at the ITG Symposium on Photonic Networks (ITG Fachtagung Photonische Netze) 2013 [Jončić13a].

6.1 Requirements for spectral grid in the visible spectrum

To evaluate the applicability of a spectral grid to support visible spectrum WDM applications over SI-POF, the appropriate criteria were first established. Those criteria refer to:

1. Channel distribution with respect to the spectral attenuation of SI-POF;
2. Performances of different demultiplexing techniques;
3. Availability of laser diodes in the visible spectrum.

6.1.1 Channel distribution with respect to the spectral attenuation of SI-POF

Criterion: *A spectral grid should have channels at wavelengths (frequencies) or in wavelength (frequency) regions where the attenuation of SI-POF experiences absolute or relative minima.*

The typical spectral attenuation of SI-POF is shown in Fig. 6.1. The fiber supports operation in the visible spectrum (400-700 nm) where it also provides four attenuation windows. Those are blue, green, yellow and red windows with the attenuation minima at 476 nm, 522 nm, 568 nm and 650 nm respectively. In the red window the attenuation rapidly increases for wavelengths around 650 nm. In three other windows the slope of the attenuation curve is considerably less steep, and thus less sensitive to the spectral shift of transmitters caused by the manufacturing tolerances and temperature changes.

Therefore, the spectral grid should specify channels within the visible spectral range from 400 nm to 700 nm. The grid should define one channel at or very close to 650 nm. The grid should also specify channels in each of three other attenuation windows (blue, green and

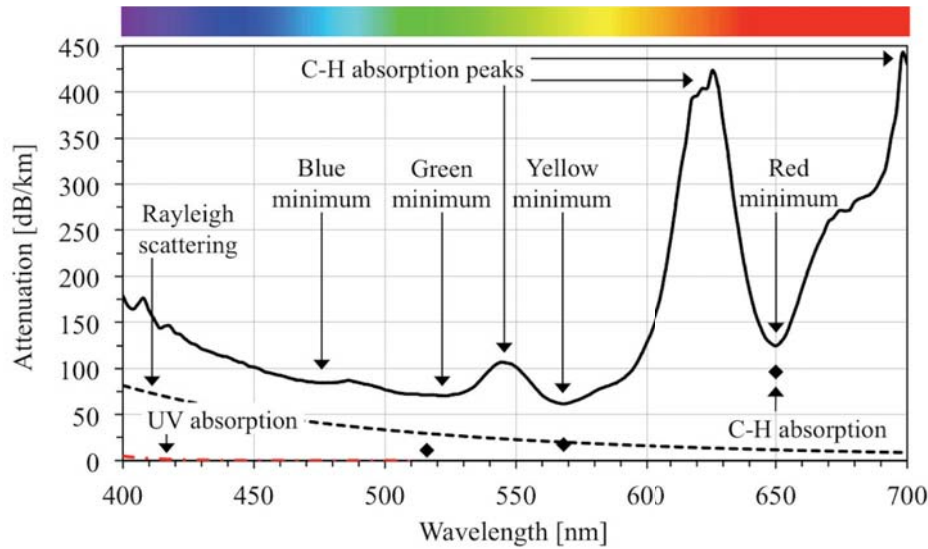


Fig. 6.1: Typical spectral attenuation of 1 mm PMMA SI-POF [Bunge11] with contributions of intrinsic loss mechanisms and with attenuation minima and maxima.

yellow). Having the channels at wavelengths where the attenuation experiences local maxima should be avoided.

6.1.2 Performances of different demultiplexing techniques

Criterion: A spectral grid should provide high channel density to ensure long-term compatibility and high transmission capacity, but also sufficient channel spacing to comply with the current and near-future demultiplexing solutions.

A major challenge in WDM for large-core SI-POF is to realize a demultiplexer. The main requirements for the demultiplexer are low IL, good IL uniformity (low IL uniformity value) and high channel isolation. The higher the channel count is, the more difficult it is to comply with those requirements. Different approaches for realization of the demultiplexer, including dispersion prisms [Lutz05], [Zhang05], interference filters [Junger02], [Appelt02], [Bartkiv03], [Kruglov12a], [Jončić13b], plane [Pinzon13], [Pinzon14], [Kruglov14] and concave diffraction gratings [Haupt10], [Bartkiv05], [Bartkiv10], [Ziemann11] were shown. Based on those solutions, Table 6.1 gives the comparison of the available demultiplexing techniques. The demultiplexers with prisms, interference filters, and plane diffraction gratings require additional focusing and collimating optics, leading to a bulky design and causing additional losses. The best results for SI-POF demultiplexer could most likely be achieved with a concave grating, which combines both the imaging and the wavelength-separating function and does not require any additional optics.

At the current development stage of SI-POF demultiplexers it would be realistic to separate up to eight channels in the visible spectrum with acceptable IL. For example, a three-stage configuration of the demultiplexer with interference filters could be employed. However, the spectral grid should provide even higher channel count to ensure compatibility with future

Table 6.1: Comparison of different demultiplexing techniques.

Demultiplexing technique	Channel count	Channel spacing	IL	Isolation	Size
Dispersion prisms	low	wide	high	medium	large
Interference filters	low to medium	narrow or wide	low to medium	high	medium to large
Plane gratings	low to medium	narrow or wide	medium to high	medium to high	medium to large
Concave gratings	potentially high	potentially narrow	potentially low	medium to high	small to medium

technological improvements. For the less demanding WDM applications requiring wider channel spacing, the channel plans using e.g. every second or fourth channel of the original grid could be adopted.

6.1.3 Availability of laser diodes in the visible spectrum

Criterion: *The channels of a spectral grid should be located at wavelengths where the laser diodes are available.*

The main requirement for a WDM system in the visible spectrum is to overcome low bandwidth of SI-POF. In order to maximize the data rates in the individual WDM channels, it would be necessary to employ high-power laser diodes as transmitters. Such diodes typically support operation with higher modulation amplitudes that should be used to compensate the losses occurring in the multiplexer and demultiplexer. Fig. 6.2 gives an overview of the commercial visible laser diodes from Sanyo, Osram, Nichia and Opnext with the optical output power greater than 10 mW (10 dBm). The following wavelengths are available:

- Violet lasers: 405nm, 415 nm and 422 nm;
- Blue lasers: 445 nm, 450 nm, 455 nm, 473 nm and 488 nm;
- Green lasers: 505 nm, 515 nm and 520 nm;
- Red lasers: 633-642 nm, 650 nm, 658-660 nm, 670 nm, 685 nm and 690 nm.

Currently, up to 9 laser diodes with at least 17 nm separation between the nominal lasing wavelengths could be employed at the same time.

The laser diodes operating in the yellow attenuation window, where the attenuation exhibits absolute minimum, would be ideal transmitters for SI-POF systems. Such devices are still not commercially available. However, a yellow laser diode with continuous-wave operation was demonstrated in [Tanaka13]. The fabricated diode had the lasing wavelength of 571 nm and the optical output power of 50 mW, which make it optimal for use in single- and multi-channel SI-POF systems.

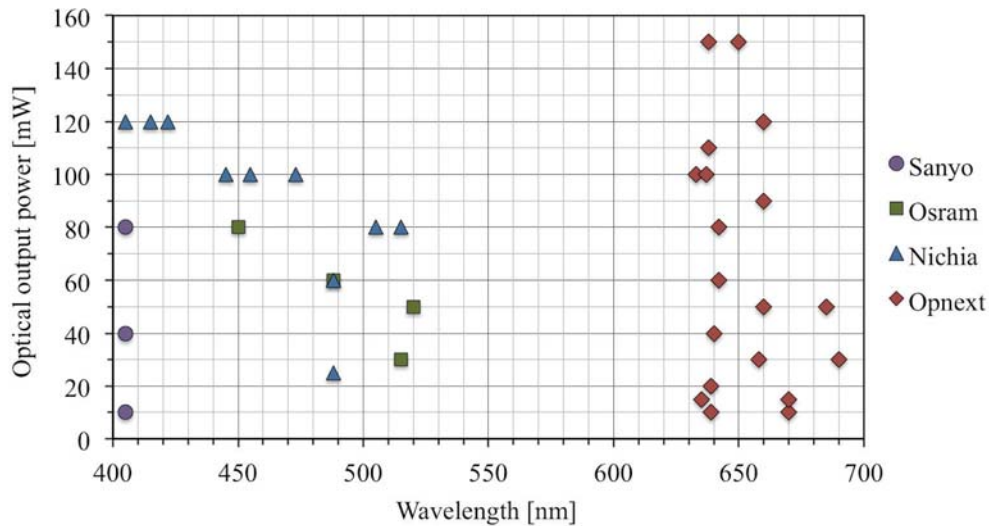


Fig. 6.2: Overview of the commercial visible laser diodes with the optical output power ≥ 10 mW (datasheet information).

6.2 Establishing and evaluating grids in the visible spectrum

Two ways for establishing spectral grids in the visible spectrum were used in this thesis:

1. Extend existing grid from infrared into the visible spectral range;
2. Define a new wavelength or frequency grid in the visible spectrum.

6.2.1 Extension of ITU-T G.694.1 DWDM grid into the visible spectrum

If ITU-T G.694.1 DWDM frequency grid with 100 GHz channel spacing would be extended into the visible spectrum, 3213 channels between 428.3 THz (700 nm) and 749.5 THz (400 nm) would be obtained, as shown in Fig. 6.3. In the wavelength domain the channel spacing would reduce from 0.163 nm for the channels in 700 nm region to 0.053 nm for the channels in 400 nm region. For the channel spacing of $100/n$ GHz, where $n=2, 4, 8$, the number of channels in the same spectral region would further increase to $3212 \cdot n + 1$.

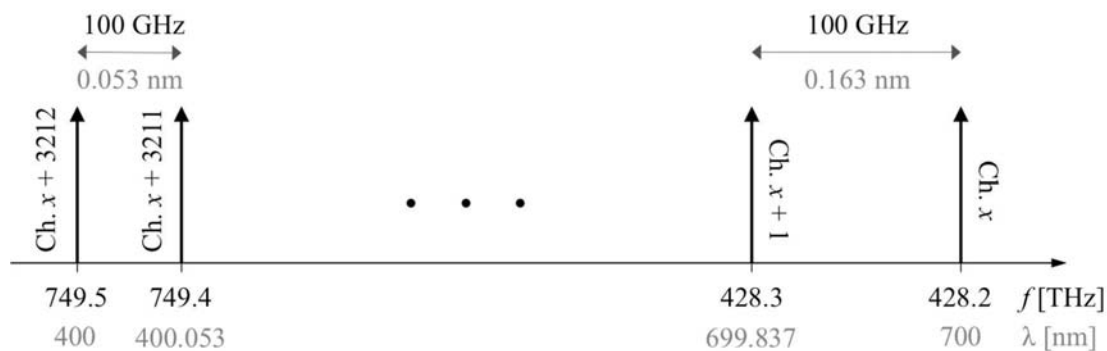


Fig. 6.3: Extension of ITU-T G.694.1 DWDM frequency grid into the visible spectrum.



According to [ITU12a], dense WDM systems have the frequency spacing between the adjacent channels less than or equal to 1000 GHz. In the wavelength domain the channel spacing of 1000 GHz corresponds to 0.53 nm and 1.63 nm for the wavelengths in 400 nm and 700 nm spectral regions respectively. Even the channel spacing of 8 nm (transition from dense to coarse WDM at 1550 nm) would be too demanding for demultiplexers in the visible spectrum. Furthermore, the demands for POF WDM systems, including channel count, data rates and control of laser wavelengths, are far more modest than for DWDM systems.

Therefore, it can be stated that dense WDM concept and the extension of DWDM grid into the visible spectrum are not suitable for WDM applications over SI-POF.

6.2.2 Extension of ITU-T G.694.2 CWDM grid into the visible spectrum

If ITU-T G.694.2 CWDM wavelength grid would be extended into the visible spectrum, 15 equidistant channels between 400 nm and 700 nm would be obtained, as shown in Fig. 6.4. The parameters of the grid including the nominal central wavelengths, corresponding frequencies and attenuation coefficients are listed in Table 6.2. The channel spacing of 20 nm makes good utilization of the available spectral range. In the red window the extension has a channel at 651 nm, which is very close to the attenuation minimum at 650 nm. The channel distribution also corresponds well to three other attenuation windows. The channels experiencing the highest attenuation are those at 611 nm, 631 nm, 671 nm and 691 nm. Those channels could be used for distances up to 20 m since they would experience approximately the same attenuation as 651 nm channel over 50 m, but lower intermodal dispersion. Good channel allocation, sufficient channel spacing, high channel count and good availability of the transmitters make the extension of CWDM grid very suitable to support WDM applications over SI-POF.

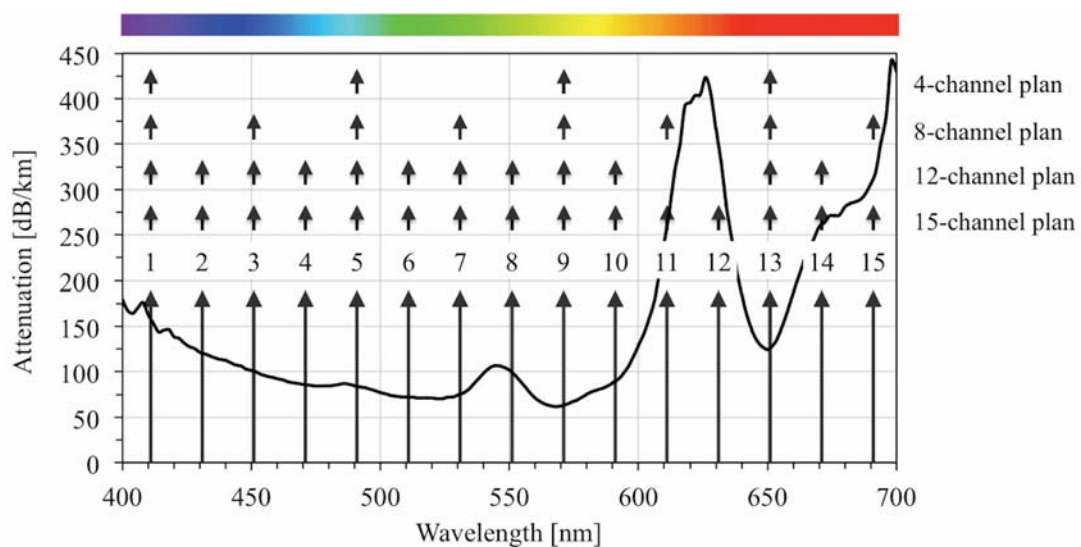


Fig. 6.4: Extension of CWDM wavelength grid into the visible spectrum and channel plans for 4-, 8-, 12- and 15-channel applications.

Table 6.2: Basic parameters of CWDM grid extension.

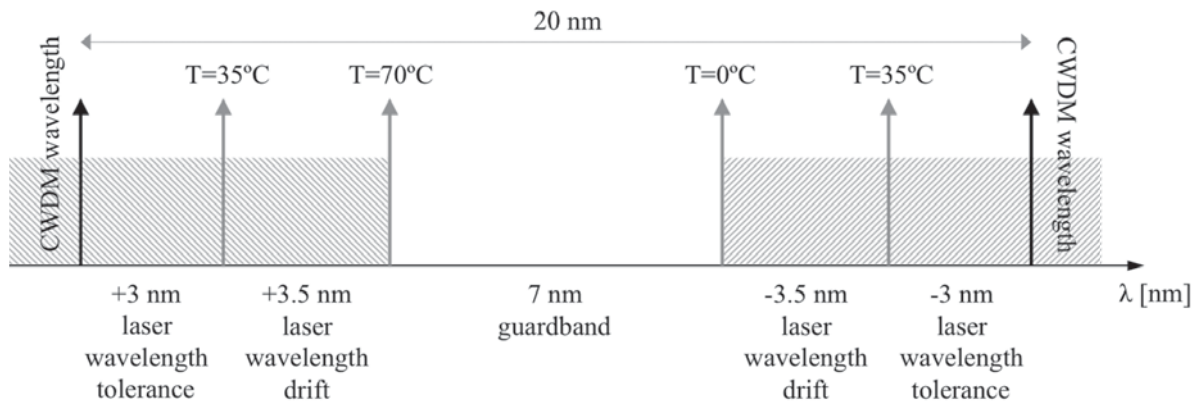
Chanel	Nominal central wavelength [nm]	Approximate nominal central frequency [THz]	Approximate attenuation coefficient [dB/km]
1	411	729	158
2	431	696	120
3	451	665	100
4	471	637	85
5	491	611	84
6	511	587	72
7	531	565	75
8	551	544	99
9	571	525	63
10	591	507	89
11	611	491	259
12	631	475	349
13	651	461	126
14	671	447	261
15	691	434	313

The long-term compatibility and high transmission capacity of the grid would be ensured by a high channel count. For the less demanding WDM applications with wider channel spacing, the channel plans could be adopted. Table 6.3 shows possible channel plans for the extension of CWDM grid into the visible spectrum. Suggested plans support WDM applications with 4, 8, 12 and 15 channels. For 4-channel applications with 80 nm channel spacing all demultiplexing techniques listed in Table 6.1 could be used. Interference filter- and grating-based demultiplexers would be suitable for the realization of 8-channel systems with 40 nm channel spacing. Only a properly designed concave grating-based demultiplexer would probably be able to provide, at a reasonable IL, high channel count and 20 nm channel spacing required in 12-channel applications. The channels with the highest attenuation, omitted in 12-channel plan, could be utilized in 15-channel applications but only up to certain transmission distance (e.g. 20 m). The proposed channel plans are also designated in Fig. 6.4.

The main requirement for POF WDM systems is cost-effectiveness. Like in CWDM systems in the infrared range, that could be achieved by allowing tolerances for laser wavelengths, and by using uncooled lasers and low-cost demultiplexers. Therefore, it would be reasonable to adopt the values for tolerances, temperature drifts and demultiplexer passbands already specified for CWDM systems, as shown in Fig. 6.5 (see also subchapter 2.5.1).

Table 6.3: Channel plans for CWDM grid extension.

Nominal central wavelength [nm]	4-channel applications	8-channel applications	12-channel applications	15-channel applications
411	*	*	*	*
431			*	*
451		*	*	*
471			*	*
491	*	*	*	*
511			*	*
531		*	*	*
551			*	*
571	*	*	*	*
591			*	*
611		*		*
631				*
651	*	*	*	*
671			*	*
691		*		*


Fig. 6.5: Allowed variation of CWDM laser wavelengths requiring demultiplexers with 13 nm passband channels (according to [ITU03]).

6.2.3 Newly defined frequency and wavelength grids

Having the values of 8 nm and 50 nm as the minimum and the maximum coarse WDM channel spacing, it is clear that POF WDM systems in the visible spectrum should belong to coarse WDM category. In this subchapter the newly defined coarse WDM grids will be presented and analyzed.

Frequency grids

A frequency grid anchored to 461.2 THz (650 nm) with 22.2 THz channel spacing is shown in Fig. 6.6 on the wavelength axis. The parameters of the grid are listed in Table 6.4. The grid has 15 channels between 749.8 THz (399.8 nm) and 439 THz (682.9 nm). The channels at

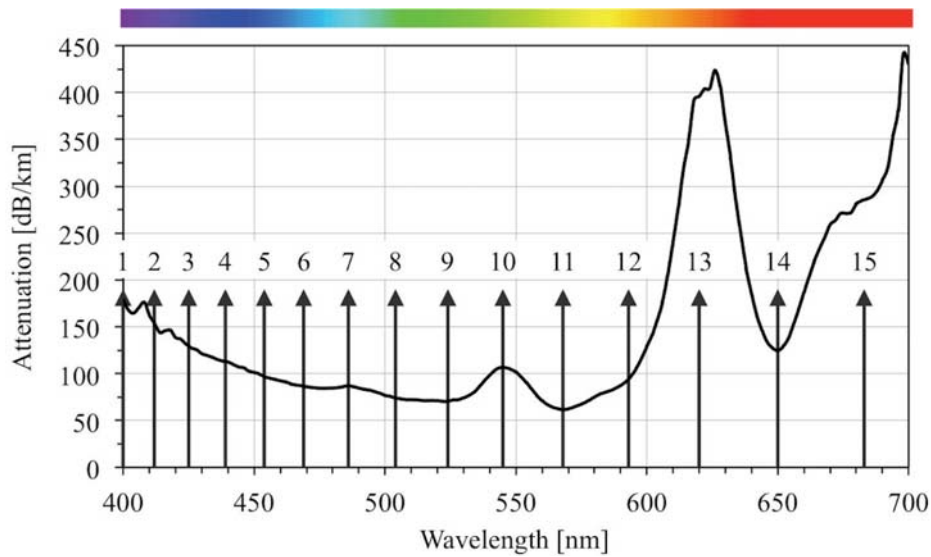


Fig. 6.6: Frequency grid anchored to 461.2 THz (650 nm) with 22.2 THz channel spacing and 15 channels in the visible spectrum.

Table 6.4: Basic parameters of the frequency grid anchored to 461.2 THz (650 nm) with 22.2 THz channel spacing and 15 channels in the visible spectrum.

Channel	Nominal central frequency [THz]	Approximate nominal central wavelength [nm]	Approximate attenuation coefficient [dB/km]
1	749.8	399.8	179
2	727.6	412.0	153
3	705.4	425.0	129
4	683.2	438.8	113
5	661	453.5	97
6	638.8	469.3	86
7	616.6	486.2	87
8	594.4	504.4	74
9	572.2	523.9	70
10	550	545.1	106
11	527.8	568.0	62
12	505.6	592.9	94
13	483.4	620.2	396
14	461.2	650.0	125
15	439	682.9	285

469.3 nm, 523.9 nm, 568 nm and 650 nm comply well with the attenuation minima of SI-POF. The nominal central frequencies (wavelengths) of the grid also comply well with the available lasing wavelengths in the visible spectrum. As can be noticed, a constant channel spacing in the frequency domain results in a variable channel spacing in the wavelength domain that increases from 12.2 nm in 400 nm region to 32.9 nm in 700 nm region. By concentrating most of the channels in the violet, blue and green wavelength regions, the number of channels experiencing high attenuation is reduced to two (channels 13 and 15). However, the narrower channel spacing in the short wavelength region would impose stricter requirements for filters and laser wavelength variation. Furthermore, the allowed wavelength drifts and filter parameters would have to be individually specified, at least for those channels with the channel spacing less than 20 nm.

Therefore, for WDM applications over SI-POF it is not suitable to have a frequency grid. Instead, it would be more convenient to have a wavelength grid with equidistant channel spacing.

Wavelength grids

The basic idea when considering new wavelength grids in the visible spectrum was to systematically establish and evaluate grids with equidistant channel spacing ranging from 8 nm to 50 nm. To comply with the nominal center wavelengths of commercial components (e.g. laser diodes or interference filters) that are typically specified as whole numbers, 1 nm increment of the channel spacing was adopted. Furthermore, only the grids with the whole-numbered nominal central wavelengths were subject to analysis.

To achieve that, the following procedure was applied. The separation (in nm) between the shortest and the longest channel of the grid was designated as D . If D was not a prime number it could be prime factorized i.e. decomposed into its constituent prime factors which when multiplied result in an original number. Depending on the prime factors obtained, one or more $a \cdot b$ products could be formed such that $D = a \cdot b$, where

- a stands for the number of channels decremented by one, and
- b stands for the channel spacing.

For a given D only some $a \cdot b$ products were of interest. For example, let D equal 294 nm. The prime factorization of this number results in $294 = 2 \cdot 3 \cdot 7^2$. The $a \cdot b$ products which were not of interest are $2 \cdot 147$, $3 \cdot 98$, $49 \cdot 6$, $98 \cdot 3$ and $147 \cdot 2$. The applicable $a \cdot b$ products were $6 \cdot 49$, $14 \cdot 21$ and $21 \cdot 14$. The product $14 \cdot 21$ refers to the grid with 15 ($14+1$) channels and 21 nm channel spacing. On the other hand, the commutative product $21 \cdot 14$ designates the grid with 22 ($21+1$) channels and 14 nm channel spacing.

Having the visible spectrum extending from 400 nm to 700 nm, the maximum value of D was 300 nm. In this example 300 could be written as a unique combination of the following prime factors $300 = 2^2 \cdot 3 \cdot 5^2$. The $a \cdot b$ products of interest were $10 \cdot 30$, $12 \cdot 25$, $15 \cdot 20$, $20 \cdot 15$, $25 \cdot 12$ and $30 \cdot 10$.

When the applicable $a \cdot b$ products were found i.e. when for a given D the possible channel counts and channel spacings were known, the optimal position of the grid on the wavelength axis had to be determined. First, the grid was centered around 550 nm midpoint of the visible spectrum. The grid was then shifted upward or downward in steps of 1 nm along the wavelength axis in order to find the best position according to the criteria for the minimum attenuation and the availability of the laser diodes. To keep all channels within 400-700 nm region and avoid making space for an additional channel (which then refers to $(a+1) \cdot b$ product and therefore another D), the upward and downward shift (in nm) were limited to:

- $\leq (300-D)/2$ if $(300-D) < b$, or
- $< (300-D)/2$ if $(300-D) \geq b$.

For example, let $D=280$ nm. When a grid with 15 channels ($a=14$) and 20 nm channel spacing ($b=20$ nm) is centered around 550 nm, the shortest and the longest wavelength of the grid are at 410 nm and 690 nm respectively. The allowed upward and downward shift for this grid would be less than 10 nm. A 10 nm downward shift would place the shortest and the longest channel at 400 nm and 680 nm respectively, therefore creating the space for an additional channel at 700 nm, which then corresponds to another D (with $a=15$ and $b=20$ nm).

The described approach was used to systematically study the wavelength grids with equidistant channel spacing ranging from 8 nm to 50 nm in increments of 1 nm, with both odd and even channel count. To perform that, the numbers from 215 to 300 were prime factorized and obtained $a \cdot b$ products were analyzed. In case of duplication, only the grid with a higher channel count was considered (e.g. $300=15 \cdot 20$ and $260=13 \cdot 20$; only $15 \cdot 20$ was considered, $13 \cdot 20$ was dismissed).

It was found that the following two grids with 20 nm channel spacing best satisfy the criteria set in subchapter 6.2:

- Grid with 15 channels distributed from 410 nm to 690 nm;
- Grid with 16 channels distributed from 400 nm to 700 nm.

The channel spacing of 20 nm was estimated to be realistic for POF WDM systems, providing both sufficient utilization of the available spectral range and enough tolerance for the low-cost components. The former grid, among others, places one channel directly at 650 nm. It deviates from CWDM grid extension by only 1 nm, thereby also confirming good performances of CWDM grid extension. The latter grid increases the channel count to 16, thereby exploiting the whole visible spectral range. It is shown in Fig. 6.7 and the basic parameters of the grid are listed in Table 6.5. The values for the laser wavelength tolerance (± 3 nm), temperature drift (7 nm) and guardband (7 nm) specified for CWDM systems should also be applied for these two grids.

For even more flexibility, the grids with wider channel spacing should be considered. For example, the grid with 25 nm channel spacing and 13 channels between 400 nm and 700 nm. The guardband between the adjacent channels would then be 8 nm, corresponding to one third of the minimum channel spacing according to [ITU03]. By adopting the standard values for

the laser wavelength tolerance and temperature drift, an additional tolerance of ± 2 nm for the nominal wavelength of the laser diode could be introduced. That would mean, for example, that the laser diodes with the nominal lasing wavelength from 448-452 nm range could be used in the channel centred at 450 nm.

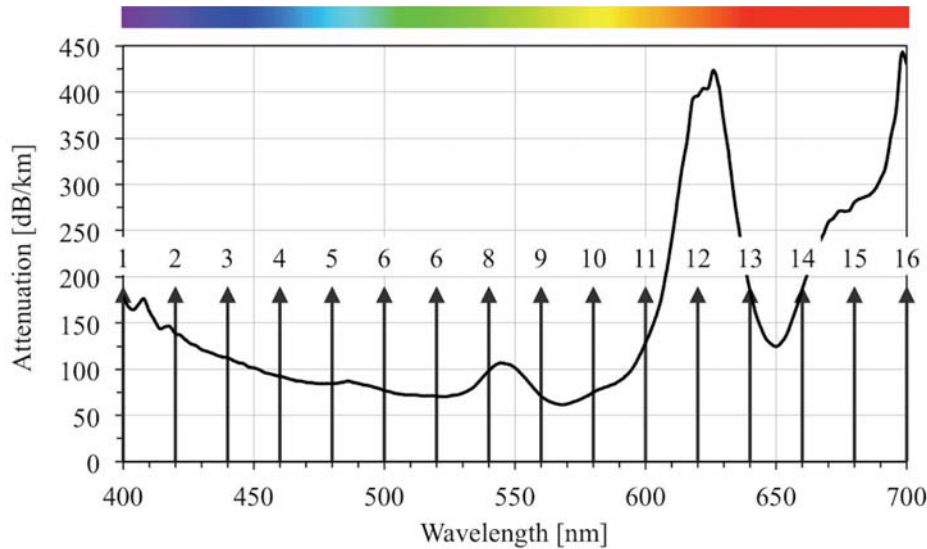


Fig. 6.7: Wavelength grid with 20 nm channel spacing and 16 channels in the visible spectrum.

Table 6.5: Basic parameters of the wavelength grid with 20 nm channel spacing and 16 channels in the visible spectrum.

Chanel	Nominal central wavelength [nm]	Approximate nominal central frequency [THz]	Approximate attenuation coefficient [dB/km]
1	400	749.5	179
2	420	713.8	138
3	440	681.3	112
4	460	651.7	92
5	480	624.6	85
6	500	599.6	77
7	520	576.5	71
8	540	555.2	98
9	560	535.3	71
10	580	516.9	75
11	600	499.7	129
12	620	483.5	396
13	640	468.4	185
14	660	454.2	187
15	680	440.9	281
16	700	428.3	430

6.3 Discussion

Having different channel allocations already analyzed in the previous sections, this subchapter summarizes the best spectral grids and gives the author's recommendations for further standardization-related activities.

Among all examined spectral grids, the following four wavelength grids stand out for their performance:

1. Extension of CWDM grid into the visible spectrum. The grid specifies 20 nm channel spacing and contains 15 channels from 411 nm to 691 nm;
2. Grid with 20 nm channel spacing and 15 channels from 410 nm to 690 nm;
3. Grid with 20 nm channel spacing and 16 channels from 400 nm to 700 nm;
4. Grid with 25 nm channel spacing and 13 channels from 400 nm to 700 nm.

These grids provide good potential for high-speed POF WDM applications and are proposed to be subject to further discussion and revision. The author's recommendation would be to adopt the extension of CWDM grid to support WDM applications over 1 mm PMMA SI-POF. The rationale for that would be not only the compliance of the grid with the set evaluation criteria, but also the compliance of the basic principles and requests for POF WDM systems in the visible spectrum with those for CWDM systems in the infrared range. Furthermore, by developing the G.hn family of standards (ITU-T Recommendations G.9960–G.9964), the ITU also laid the focus on in-home networking technologies that operate over three standard types of premises wiring (phone lines, power lines and coaxial cables). In 2012 the ITU added 1 mm PMMA SI-POF to G.hn as a fourth physical medium (ITU-T Recommendation G.9960, Annex F [ITU11]). By recognizing the potential of POF technology, the ITU opened up the possibilities for further POF-related standardization. Therefore, changing the existing CWDM standard by extending CWDM grid into the visible spectrum would be much simpler than developing a new standard for another grid.

As an alternative to the ITU, the European Telecommunications Standards Institute (ETSI), which provides ETSI TS 105 175-1 technical specification for 100 Mb/s and 1 Gb/s POF systems [ETSI15], could also offer good standardization possibilities.

The standardization of spectral channels is a necessary and important step that would stimulate further development of POF WDM technology and help towards bringing it into the market.

7 Summary and outlook

This thesis investigated the application of WDM in short-range optical communication over SI-POF. The focus of research was on:

- Demultiplexing techniques for SI-POF based on thin-film interference filters and a concave diffraction grating (chapters 3 and 4 respectively);
- Four-channel high-speed WDM transmission over SI-POF (chapter 5);
- Channel allocation for today's and future POF WDM systems (chapter 6).

Chapter 3 concentrated on the experimental realization of SI-POF demultiplexer employing thin-film interference filters. The principle of operation and the approach for experimental realization of the demultiplexer were first explained. The main characteristic of the developed demultiplexer setup was its precise adjustability. That allowed the maximization of the optical throughput in the individual channels. On the other hand, a complex and time-consuming alignment procedure was required.

In a step-by-step approach, the intermediate setups with two and three channels were first established. One of the most interesting results was realization of the two-channel demultiplexer with 10.6 nm and 9 nm passband channels centered at 640.3 nm and 661.2 nm. That is the first SI-POF demultiplexer for the red spectral window reported so far. It offered a narrow channel spacing of 20.9 nm supporting the spectral grid proposal from chapter 6. Furthermore, it complied well with 650 nm attenuation minima of SI- and GI-POF, and was suitable for use with 640 nm and 660 nm red laser diodes. The realized three-channel demultiplexers offered performances close to the best interference filter-based SI-POF demultiplexer reported so far. However, their IL was by approx. 0.5 dB/channel higher than expected, most likely because of the accumulated dust on the optical surfaces and coating damages due to improper handling. Even then, the IL required for the separation of up to three channels was less than 4 dB.

In addition, a serial and a two-stage configuration of the target setup with four channels were realized and mutually compared. An important result was that the two-stage configuration significantly outperformed the serial one in terms of IL and IL uniformity. The demultiplexer with two-stage configuration provided 9.4 nm, 9.3 nm, 41.6 nm and 47.6 nm passband channels centered at 404.9 nm, 450.1 nm, 528.3 nm and 646.4 nm. Its exceptional performances, including the IL of 3.19-5.66 dB, isolation greater than 30 dB and channel count of four, make it the best interference filter-based demultiplexer for SI-POF reported so far. As such, it was very suitable to support high-speed POF WDM transmission.

For the channel count up to four it was demonstrated that SI-POF demultiplexers employing interference filters offer the advantages of good wavelength selectivity, high channel isolation, low IL and flat-top spectral response. The costly, bulky and alignment sensitive setup would be difficult to implement in non-laboratory conditions. However, low IL and high isolation make these demultiplexers suitable for implementation in high-speed POF WDM transmission experiments and investigation on their data-carrying capacity. For those reasons, further optimization of the realized setup and extending the channel count gains in importance. For example, the use of achromatic or aspherized achromatic lenses in the input and the output demultiplexer ports represents an apparent solution for achieving color correction over a broad spectral range. Furthermore, the channel count could be increased up to eight by employing a three-stage configuration where each wavelength channel would encounter three dichroic mirrors. Thereby, the dimensions and the complexity of the demultiplexer setup could be reduced by designing a housing with slits for lenses, dichroic mirrors and interference filters.

Within the BMBF project VIP HOPE (Nov. 2010 – Feb. 2014) the parameters of the SI-POF demultiplexer based on a concave diffraction grating were optimized by means of an optical simulation software. The demultiplexer was designed to support operation with four laser-diode based channels at 405 nm, 450 nm, 520 nm and 650 nm in the second diffraction order. Moreover, four demultiplexer samples with the grating mechanically ruled on a PMMA substrate were produced. These are the first concave grating-based demultiplexers ever reported for SI-POF. Since the samples became available in the late project phase, their demultiplexing properties could not be examined during the project duration.

Chapter 4 addressed subsequent theoretical and experimental analysis of the VIP HOPE project demultiplexer (see previous paragraph). Comparing the theoretical diffraction angles with the previous simulation results revealed a considerable mismatch between the calculated and the simulated values. It was found that shortening of wavelengths when light enters PMMA was not taken into consideration when designing the demultiplexer. This meant that optimization of the grating parameters for detection in the second diffraction order was based on a false assumption that design vacuum wavelengths were incident on the grating. However, an important observation from chapter 4 was that the wavelength shortening in PMMA by a factor of approx. 1.5 and a ratio of the third and the second diffraction order of $3/2=1.5$ cancel each other in the grating equation. It was further shown that the demultiplexer could provide good detecting possibilities in the third order, but with a reduced operating wavelength range (427-620 nm instead of initially planned 400-700 nm). Having the violet and red channels unsuitable for use, the demultiplexer was expected to support two-channel operation in the third order using 450 nm and 520 nm laser diodes.

For characterizing the transmission properties of the samples, two measurement methods and the corresponding mounting setups were proposed and investigated. In both cases the curved focal surface of the demultiplexer had to be scanned with 1 mm output SI-POF. The basic difference between the methods was the orientation of the scanning output fiber with respect to the grating center. The initially developed more complex method preserved an ideal

orientation of the fiber axis to the grating center during the scan, introducing small longitudinal displacement between the actual and the ideal fiber position (e.g. 169 μm displacement at 20° diffraction angle). That had to ensure that the measurement results most closely correspond to the actual values (0.7 dB corresponding correction factor). On the other hand, high alignment sensitivity was inherent to the method, making any measurement attempt with the realized mounting setup unreliable. For that reason, the simplified measurement method was subsequently developed. In that method the output fiber was always perpendicular to the demultiplexer surface, with the fiber axis going through the center of the Rowland circle. That introduced angular displacement between the actual and the ideal fiber position (e.g. 20° displacement at 20° diffraction angle), resulting in more inaccuracy in the measurement results (2.8 dB corresponding correction factor). However, the method was less alignment-sensitive and therefore more suitable for practical realization. Having the initially developed method potentially more accurate, it would be recommendable to optimize the corresponding mounting setup for characterization of future demultiplexer samples. In the thesis, the experimental results were obtained with the simplified method.

For the first time, the transmission characteristics of one concave grating-based SI-POF demultiplexer were measured. Both the diffraction angle-dependent spectral response over a broad wavelength range (400-700 nm) and the diffraction angle-dependent transmittance at five lasing wavelengths (405 nm, 450 nm, 520 nm, 638 nm and 660 nm) were presented. A significant observation from chapter 4 was that the measured diffraction angles in both positive and negative orders corresponded well to the theoretical values. The existing angular deviations indicated that the ruling process introduced random variations of the groove spacing across the grating surface. Another observation was that the distribution of light intensity among the orders did not follow the expected diffraction efficiency, having more intensity concentrated in the first and the second than in the third order. That indicated that the groove depth and the groove shape were the production parameters much more difficult to control than the groove spacing. It was shown that in the best case the demultiplexer could support two-channel operation (520 nm and 660 nm) in the second order with IL of around 20 dB and channel isolation of 13 dB. Furthermore, it was estimated that the minimum IL of around 20 dB was composed of 6 dB scattering loss and 14 dB loss due to combined effects of low diffraction efficiency, high interorder scatter and high coupling loss in the image layer. Because of the poor grating structure resulting in high IL and low channel isolation, the produced demultiplexer samples did not fulfil the requirements to be used for high-speed POF WDM transmission experiments.

Further optimization of demultiplexer parameters and ruling process is required to realize a functional device capable of supporting POF WDM applications. The demultiplexer with current parameters can support operation with two laser diode-based channels in the third diffraction order. The blaze angle and the sagittal radius should be re-optimized for the operation with three channels in the second order. For the operation with a higher channel count, the dimensions of the demultiplexer (e.g. tangential radius, grating height and width) would have to be increased. Alternatively, the demultiplexer could be re-designed for use

with the smaller-diameter fibers. To obtain an accurately shaped sawtooth profile with the required groove spacing and groove depth, the parameters of the ruling process would have to be stabilized. If that would be achieved, a master grating could be directly ruled on a molding tool, and a demultiplexer with fixed entrances for the input and the output fibers could be cost-effectively produced through injection moulding. That could open up the possibilities for commercial implementation of POF WDM.

Chapter 5 presented four-channel POF WDM data transmission experiments, demonstrating the feasibility and potential of a high-speed POF WDM concept. For the separation of laser diode-based wavelength channels the four-channel demultiplexer with two-stage configuration was used. Several optimization steps with the intermediate results were shown before the target experimental setup and data transmission results were presented. One of the most important setup improvements was realization of the four-legged POF bundle to multiplex the signals coming from four different laser diodes. For direct launching the overall optical power loss at the transmitter side (launching coupling loss, bundle leg attenuation and loss of the multiplexing interface) was only 3.3-5.5 dB. Because of its simplicity and effectiveness, the suggested approach significantly outperformed any other multiplexing technique. The patent application for an optical POF multiplexer based on a multi-legged POF bundle, which referred to arbitrary channel counts and fiber diameters, was also submitted to the German Patent and Trade Mark Office (DPMA) under number DE 10 2013 020 236.1. Further investigation on using multi-legged POF bundles as multiplexers is recommended as an important point for the follow-up research.

By employing NRZ modulation and linear FFE equalization the aggregate data rates of 7.8 Gb/s and 3.21 Gb/s were demonstrated over 50 m and 100 m SI-POF respectively at the $BER < 10^{-4}$. The corresponding net bit rates were 7.56 Gb/s and 3.11 Gb/s. An interesting observation was that POF WDM with simple transmission technique and lower channel rates provided aggregate bit rates comparable to those achieved with the single-wavelength systems that used more advanced transmission techniques but required more signal processing. Therefore, another important point for further work would be to investigate whether POF WDM with simple transmission techniques and lower channel rates offers advantages over fast single-channel transmission (e.g. in applications where low latency is required).

The most important results in chapter 5 were achieved through the cooperation with Dr.-Ing. Roman Kruglov from the POF-AC. The 14.77 Gb/s data transmission based on the offline-processed DMT modulation was demonstrated over 50 m SI-POF at the $BER = 10^{-3}$. That is the second highest transmission capacity ever reported over 50 m SI-POF. For that purpose four laser diode-based channels at 405 nm, 450 nm, 515 nm and 639 nm were used. In addition, the similar setup was used to demonstrate record 8.26 Gb/s data rate over 100 m SI-POF at the $BER = 10^{-3}$. That is the only 100 m POF WDM experiment reported so far. The corresponding information rates were 13.8 Gb/s and 7.72 Gb/s, offering two times higher transmission capacity than the fastest single-wavelength systems.



To further increase the aggregate WDM data rates, the additional optimization of the demultiplexer to provide lower IL, and of the transmission system and DMT signal parameters is required. With a four-channel WDM system an aggregate data rate of 16.05 Gb/s at the $\text{BER}=10^{-3}$ could probably be achieved over 50 m SI-POF. That would correspond to 15 Gb/s error free transmission. An aggregate data rate of 9.35 Gb/s could presumably be reached over 100 m link, resulting in 9 Gb/s information bits. With the available transceiver components and a properly designed eight-channel interference filter-based demultiplexer employing three-stage configuration, a possible aggregate data rate over 50 m SI-POF would be 32.1 Gb/s at the $\text{BER}=10^{-3}$. That would correspond to the information rate of 30 Gb/s (in average 3.75 Gb/s per WDM channel).

Chapter 6 investigated spectral grids for the visible spectrum WDM applications over SI-POF. First, the criteria for evaluating the applicability of a grid for the intended application were defined. In addition, the newly defined frequency and wavelength grids as well as the extensions of existing grids from infrared into the visible spectral range were analyzed. It was estimated that 20 nm channel spacing is realistic for POF WDM systems, providing both sufficient utilization of the available spectral range and enough tolerance for the low-cost components. As an important result, the extension of ITU-T G.694.2 CWDM grid into the visible spectrum was suggested to support WDM applications over SI-POF. With 20 nm channel spacing and 15 channels in 400-700 nm region, the grid provides good potential for high-speed applications. Furthermore, by recently recognizing the potential of POF technology, the ITU opened up the possibilities for further POF-related standardization. Therefore, changing the existing CWDM standard by extending CWDM grid into the visible spectrum would be much simpler than developing a new standard for another grid. Further activities towards standardization of the spectral channels are recommended as a necessary and important step that would stimulate the development of POF WDM technology and help towards bringing it into the market.

For commercial implementation of POF WDM, a mass production of low-IL multiplexing and demultiplexing components in a cost effective way (e.g. injection molding) is required. Supported by the technological advancements related to the capacity increase of a single channel, POF WDM might represent a networking solution offering both the advantage of a robust and easy-to-install transmission medium, and of a high-speed data communication. That might open up the possibilities for SI-POF technology to be used in the next generation broadband in-house networks and in high-speed very short reach optical interconnection networks (e.g. in data centers, and for inter-rack or inter-board interconnections).

To conclude, this thesis investigated several aspects of WDM for short-range optical communication over SI-POF. The WDM components with low IL were realized, high-speed WDM transmission over SI-POF was demonstrated and channel allocation for POF WDM was proposed. The results from the thesis make a significant contribution to the investigation and development of WDM technology for large-core POFs, and set a good basis for the follow-up research.



References

- [Agilent09] Agilent Technologies, Inc. (2009). User's guide. *Agilent N5461A Infiniium Serial Data Equalization* [Online]. Available www.keysight.com.
- [Agilent13] Agilent Technologies, Inc. (2013). Data sheet. *EZJIT Complete Jitter and Vertical Noise Analysis Software for Infiniium Oscilloscopes* [Online]. Available www.keysight.com.
- [Appelt02] V. Appelt, J. Vinogradov, and O. Ziemann, "Simple FEXT compensation in LED based POF-WDM systems," in *11th International Conference on Plastic Optical Fibers*, pp. 127–129, 2002.
- [Atef12] M. Atef, R. Swoboda, and H. Zimmermann, "1.25 Gbit/s over 50 m step-index plastic optical fiber using fully integrated optical receiver with an integrated equalizer," *IEEE Journal of Lightwave Technology*, vol.30, no. 1, pp. 118-122, Jan. 2012.
- [Azadet99] K. Azadet and M. Yu. (1999). *Forward error correction (FEC) techniques for optical communications* [Online]. Available www.ieee802.org/3/10G_study/public/july99/azadet_1_0799.pdf.
- [Bartkiv03] L. V. Bartkiv, H. Poisel, and O. Ziemann, "A 3-channel POF-WDM system for transmission of VGA signals," in *12th International Conference on Plastic Optical Fibers*, pp. 264–270, 2003.
- [Bartkiv05] L. V. Bartkiv, Y. V. Bobitski, and H. Poisel, "Optical demultiplexer using a holographic concave grating for POF-WDM systems," in *Optica Applicata*, vol. XXXV, no. 1, 2005.
- [Bartkiv10] L. V. Bartkiv and Y. V. Bobitski, "Design and optimization of concave diffracton grating for WDM multi/demultiplexer," in *10th International Conference on Laser and Fiber-Optical Networks Modeling*, pp. 128-130, 2010.
- [Breyer10] F. Breyer, "Multilevel Transmission and Equalization for Polymer Optical Fiber Systems," Ph.D. dissertation, Fakultät für Elektrotechnik und Informationstechnik, Technische Universität München, Germany, 2010.
- [Bunge11] C.-A. Bunge, private communication – spectral attenuation of Asahi fiber specified for MOST, June 2011.



- [Bunge12] C.-A. Bunge, “Optische Busse im Bereich Automotive,” in *Innovationsforum: Automotive, Logistik und Fabrikautomation mit optischen Polymerfasern*, U. H. P. Fischer-Hirschert, Ed., Cuvillier Verlag Göttingen, 2012.
- [Cardiff11] B. Cardiff, M. F. Flanagan, F. Smyth, L. P. Barry, and A. D. Fagen, “On bit and power loading for OFDM over SI-POF,” *IEEE Journal of Lightwave Technology*, vol. 29, no. 10, pp. 1547–1554, May 2011.
- [Chow95] P. S. Chow, J. M. Cioffi, and J. A. C. Bingham, “A practical discrete multitone transceiver loading algorithm for data transmission over spectrally shaped channels,” *IEEE Transactions on Communications*, vol. 43, no. 2, pp. 773–775, Feb. 1995.
- [Cioffi91] J. M. Cioffi, “A multicarrier primer,” Stanford University/Amati T1E1 contribution, T1E1.4/91-157, 1991.
- [Diaz12] E. Diaz and M. Knobl, “Prototyping illumination systems with stock optical components,” *Photonik International*, pp. 24-27, 2012.
- [Dutta03] A. K. Dutta, N. K. Dutta, and M. Fujiwara, *WDM Technologies: Passive Optical Components*. Academic Press, 2003.
- [Edmund13] Edmund Optics Inc. (2013), Application note, *The benefits of color corrected optical lenses* [Online]. Available www.electrooptics.com.
- [Emslie88] C. Emslie, “Review polymer optical fibers,” *Journal of Materials Science*, vol. 23, pp. 2281-2293, 1988.
- [ETSI15] *Access, Terminals, Transmission and Multiplexing (ATTM); Plastic Optical Fibres; Part 1: Plastic Optical Fibre System Specifications for 100 Mbit/s and 1 Gbit/s; Sub-part 2: 1 Gbit/s and 100 Mbit/s physical layer for Plastic Optical Fibres*, ETSI Technical Specification 105 175-1-2 V1.1.1, Apr. 2015.
- [Fischer11] U. H. P. Fischer-Hirschert, M. Haupt, and M. Jončić, “Optical transmission systems using polymeric fibers,” in *Optoelectronics—Devices and Applications*, P. Predeep, Ed., InTech, 2011, ch. 22.
- [Gaudino11] R. Gaudino, final report of an EU project *POF-PLUS – Plastic Optical Fibre for Pervasive Low-cost Ultra-high Capacity Systems*, 2011.
- [Graviton06] Graviton Inc. (2006). User’s manual. *PD Series O/E Converter – 650 nm version – Model SPD-1 650, SPD-2 650* [Online]. Available www.graviton.co.jp.
- [Groh88] W. Groh, “Overtone absorption in macromolecules for polymer optical fibers,” *Die Makromolekulare Chemie*, vol. 189, no. 12, pp. 2861-2874, 1988.
- [Grzemba08] A. Grzemba, *MOST – The Automotive Multimedia Network*. Franzis Verlag, 2008.

- [Haupt10] M. Haupt, “Wellenlängenmultiplex im sichtbaren spektrum für optische polymerfaser-systeme,” Ph.D. dissertation, Fakultät für Elektrotechnik, Informationstechnik, Physik, Technische Universität Braunschweig, Braunschweig, Germany, 2010.
- [Haupt12] M. Haupt and U. H. P. Fischer, “Optical design of a low-loss demultiplexer for optical communication systems in the visible range,” in *SPIE 8550, Optical System Design 2012*, 85500J, 2012.
- [Haupt15] M. Haupt, private communication, Feb.-Mar. 2015.
- [Hecht05] E. Hecht, *Optik*. 4th ed., Oldenburg Verlag München Wien, 2005.
- [Herbert06] V. Herbert, *Wavelength Filters in Fibre Optics*. Springer, 2006.
- [HOPE14a] U. H. P. Fischer-Hirschert, M. Haupt, M. Jončić, S. Höll, and A. Zufelde, final report of a BMBF project *VIP HOPE - Research and Development of Key Components for High-Speed Communication via Polymer Optical Fibers (Forschung und Entwicklung von Schlüsselkomponenten für Hochgeschwindigkeits-Netze über optische Polymerfasern)*, 2014.
- [HOPE14b] U. H. P. Fischer-Hirschert, M. Haupt, M. Jončić, S. Höll, and A. Zufelde, internal result of a BMBF project *VIP HOPE - Research and Development of Key Components for High-Speed Communication via Polymer Optical Fibers (Forschung und Entwicklung von Schlüsselkomponenten für Hochgeschwindigkeits-Netze über optische Polymerfasern)* produced by S. Höll, 2014.
- [Höll13] S. Höll, M. Haupt, and U. H. P. Fischer, “Injection molding of a WDM system for POF communication,” in *63rd Electronic Components and Technology Conference (ECTC)*, pp. 2292-2297, 2013.
- [Höll14] S. Höll, M. Haupt, and U. H. P. Fischer, “New demultiplexer component for optical polymer fiber communication systems,” in *64th Electronic Components and Technology Conference (ECTC)*, pp. 1862-1869, 2014.
- [IEC09] *Optical Fibres – Part 2-40: Product specifications – Sectional specification for category A4 multimode fibers*, IEC Recommendation 60793-2-40, ed. 3.0, Apr. 2009.
- [ITU03] *Spectral Grids for WDM Applications: CWDM Wavelength Grid*, ITU-T Recommendation G.694.2, Dec. 2003.
- [ITU04] *Forward error corection for high bit-rate DWDM submarine systems*, ITU-T Recommendation G.975.1, Feb. 2004
- [ITU10] *Optical interfaces for coarse wavelength division multiplexing applications*, ITU-T Recommendation G.695, Oct. 2010.
- [ITU11] *Unified high-speed wireline-based home networking transceivers – System architecture and physical layer specification*, ITU-T Recommendation G.9960, Dec. 2011.

- [ITU12a] *Transmission characteristics of optical components and subsystems*, ITU-T Recommendation G.671, Feb. 2012.
- [ITU12b] *Spectral Grids for WDM Applications: DWDM Frequency Grid*, ITU-T Recommendation G.694.1, Feb. 2012.
- [Johnson12] K. L. Johnson, W. Hogan, M. M. Dummer, C. Steidl, and M. K. Hibbs-Brenner, “Advances in high-speed red VCSEL performance,” in *21st International Conference on Plastic Optical Fibers*, pp. 248–253, 2012.
- [Jončić13a] M. Jončić, M. Haupt, and U. H. P. Fischer-Hirschert, “Investigation on spectral grids for VIS WDM applications over SI-POF,” in *14. ITG-Fachtagung Photonische Netze*, 2013.
- [Jončić13b] M. Jončić, S. Höll, M. Haupt, R. Caspary, and U. H. P. Fischer-Hirschert, “Development status of a four-channel CWDM system for multi-Gbit/s data links over SI-POF,” in *22nd International Conference on Plastic Optical Fibers*, pp. 59–64, 2013.
- [Jončić13c] M. Jončić, M. Haupt, and U. H. P. Fischer-Hirschert, “Development status of a four-channel CWDM system for Multi-Gbit/s in-house data communication via SI-POF,” in *20. ITG-Fachtagung Kommunikationskabelnetze*, 2013.
- [Jončić14a] M. Jončić, M. Haupt, and U. H. P. Fischer-Hirschert, “Coarse WDM: A way to increase the transmission capacity of a 1-mm diameter step index polymer optical fiber,” in *15. ITG-Fachtagung Photonische Netze*, 2014.
- [Jončić14b] M. Jončić, R. Kruglov, M. Haupt, R. Caspary, J. Vinogradov, and U. H. P. Fischer-Hirschert, “Four-channel WDM transmission over 50-m SI-POF at 14.77 Gb/s using DMT modulation,” *IEEE Photonics Technology Letters*, vol. 26, no. 13, pp. 1328–1331, July 2014.
- [Jončić14c] M. Jončić, R. Kruglov, M. Haupt, R. Caspary, J. Vinogradov, U. H. P. Fischer-Hirschert, and O. Ziemann, “Four-channel WDM transmission via 1-mm SI-POF employing DMT modulation,” in *23rd International Conference on Plastic Optical Fibers*, 2014.
- [Jončić15] M. Jončić, M. Haupt, R. Caspary, U. H. P. Fischer-Hirschert, and W. Kowalsky, “Characterization of transmission properties of a mechanically ruled concave grating-based POF demultiplexer for future injection molding,” in *24th International Conference on Plastic Optical Fibers*, 2015.
- [Junger02] S. Junger, W. Tschekalinskij, and N. Weber, “POF WDM transmission system for multimedia data,” in *11th International Conference on Plastic Optical Fibers*, pp. 69–71, 2002.
- [Kaino97] T. Kaino, “Linear Optical Properties of Organic Solids,” in *Organic Molecular Solids: Properties and Applications*, W. Jones, Ed., CRC Press, 1997, ch. 7.

- [Kartalopoulos02] S. V. Kartalopoulos, *DWDM: Networks, Devices, and Technology*. Wiley-IEEE Press, 2002.
- [Keiser00] G. Keiser, *Optical fiber communications*. 3rd ed., McGraw-Hill, 2000.
- [Koike14] Y. Koike, *Fundamentals of plastic optical fibers*. Wiley, 2014.
- [Kruglov12a] R. Kruglov, J. Vinogradov, O. Ziemann, S. Loquai, and C.-A. Bunge, “10.7-Gb/s discrete multitone transmission over 50 m SI-POF based on WDM technology,” *IEEE Photonics Technology Letters*, vol. 24, no. 18, pp. 1632-1634, Sep. 2012.
- [Kruglov12b] R. Kruglov, J. Vinogradov, O. Ziemann, S. Loquai, J. Müller, U. Strauß, and C.-A. Bunge, “Eye-safe data transmission of 1.25 Gbit/s over 100-m SI-POF using green laser diode,” *IEEE Photonics Technology Letters*, vol. 24, no. 3, pp. 167-169, Feb. 2012.
- [Kruglov14] R. Kruglov, J. Vinogradov, S. Loquai, O. Ziemann, C.-A. Bunge, T. Hager, and U. Strauss, “21.4 Gb/s discrete multitone transmission over 50-m SI-POF employing 6-channel WDM,” in *OFC/NFOEC*, Paper Th2A.2, Mar. 2014.
- [Lee09a] S. C. J. Lee, “Discrete Multitone Modulation for Short-Range Optical Communication,” Ph.D. dissertation, Department of Electrical Engineering, Eindhoven University of Technology, Netherlands, 2009.
- [Lee09b] S. C. J. Lee, F. Breyer, S. Randel, R. Gaudino, G. Bosco, A. Bluschke, M. Matthews, P. Rietzsch, R. Steglich, H. P. A. v. d. Boom, and A. M. J. Koonen, “Discrete multitone modulation for maximizing transmission rate in step-index plastic optical fibers,” *IEEE Journal of Lightwave Technology*, vol. 27, no. 11, pp. 1503–1513, June 2009.
- [Lekishvili02] N. Lekishvili, L. Nadareishvili, G. Zaikov, and L. Khananashvili, *Polymers and Polymeric Materials for Fiber and Gradient Optics*. Brill Academic Publishers, 2002.
- [Lightel14] LIGHTEL. (2014). Product specification. 4, 8, and 16 Channel Extended Band CWDM Mux/Demux [Online]. Available www.lightel.com.
- [Loewen97] E. G. Loewen and E. Popov, *Diffraction Gratings and Applications*. Marcel Dekker Inc., 1997.
- [Loquai10] S. Loquai, R. Kruglov, O. Ziemann, J. Vinogradov, and C.-A. Bunge, “10 Gbit/s over 25 m plastic optical fiber as a way for extremely low-cost optical interconnection,” in *OFC/NFOEC*, Paper OWA6, Mar. 2010.
- [Loquai13] S. Loquai, R. Kruglov, B. Schmauss, C.-A. Bunge, F. Winkler, O. Ziemann, E. Hartl, and T. Kupfer, “Comparison of modulation schemes for 10.7 Gb/s transmission over large-core 1 mm PMMA polymer optical fiber,” *IEEE Journal of Lightwave Technology*, vol. 31, no. 13, pp. 2170–2176, July 2013.



- [Loquai14] S. Loquai, “Large-area Photoreceivers for Bit Rates beyond 10 Gb/s over 1 mm Polymer Optical Fiber,” Ph.D. dissertation, Technische Fakultät, Universität Erlangen-Nürnberg, Germany, 2014.
- [Lutz05] D. Lutz, M. Haupt, and U.H.P. Fischer, “Prism-spectrometer as demultiplexer for WDM over POF,” in *14th International Conference on Plastic Optical Fibers*, pp. 25-29, 2005.
- [Macleod10] H. A. Macleod, *Thin Film Optical Filters*. 4th ed., CRC Press, 2010.
- [Mukherjee06] B. Mukherjee, *Optical WDM Networks*. Springer, 2006.
- [Opielka83] D. Opielka, and D. Rittich, “Transmission loss caused by an angular misalignment between two multimode fibers with arbitrary profile exponents,” *Applied Optics*, vol. 22, no. 7, pp. 991-994, 1983.
- [Palmer05] C. Palmer and E. Loewen, *Diffraction Grating Handbook*. 6th ed., Newport Corporation, 2005.
- [Pinzon13] P. J. Pinzon, K. Hegartty, C. Vazquez, and I. Perez, “Diffraction grating-based demultiplexers for SI-POF networks,” in *22nd International Conference on Plastic Optical Fibers*, pp. 36-41, 2013.
- [Pinzon14] P. J. Pinzon, C. Vasquez, I. Perez, and P. C. Lallana, “Design and analysis of a WDM system for multi-Gbit/s transmission over 50 m of SI-POF,” in *23rd International Conference on Plastic Optical Fibers*, 2014.
- [Proakis08] S. Proakis, *Digital Communications*. 5th ed., McGraw-Hill, 2008.
- [Qian11] D. Qian, M.-F. Huang, E. Ip, Y.-K. Huang, Y. Shao, J. Hu, and T. Wang, “101.7-Tb/s (370×294-Gb/s) PDM-128QAM-OFDM transmission over 3×55-km SSMF using pilot-based phase noise mitigation,” in *OFC/NFOEC*, Paper PDPB5, Mar. 2011.
- [Ramaswami09] R. Ramaswami, K. Sivarajan, and G. Sasaki, *Optical networks, a practical perspective*. 3rd ed., Morgan Kaufmann Publishers, 2009.
- [Sundermeyer09] J. Sundermeyer, J. Tan, and C. Zerna, “Integrated analogue adaptive equalizer for gigabit transmission over standard step index plastic optical fibre (SI-POF),” in *22nd Annual Meeting of the IEEE Photonics Society*, pp. 195-196, 2009.
- [Szczurowski13] M. Szczurowski. (2013). *Optical constants of (C₅O₂H₈)_n (Poly (methyl methacrylate), PMMA)* [Online]. Available www.refractiveindex.info.
- [Tanaka13] S. Tanaka, J. Kasai, S. Fujisaki, S. Tsuji, R. Akimoto, T. Hasama, and H. Ishikawa, “Progress of Be-based II-VI green to yellow laser diodes,” in *2013 Conference on Lasers and Electro-Optics Pacific Rim (CLEO-PR)*, Paper MH2-2, June 2013.

- [Thiele04] H.-J. Thiele, P. J. Winzer, J. H. Sinsky, L. W. Stulz, L. E. Nelson, and F. Fidler, “160-Gb/s CWDM capacity upgrade using 2.5-Gb/s rated uncooled directly modulated lasers,” *IEEE Photonics Technology Letters*, vol. 16, no. 10, pp. 2389-2391, Oct. 2004.
- [Thiele07] H.-J. Thiele and M. Nebeling, *Coarse wavelength division multiplexing: technologies and applications*. CRC Press Taylor and Francis Group, 2007.
- [Tschekalinskij10] W. Tschekalinskij, S. Junger, and N. Weber, “Optical multiplexer and demultiplexer for optical fibers with a large numerical aperture,” European Patent EP 1 532 477 B1, 2010.
- [Vinogradov05] J. Vinogradov, E. Bluoss, O. Ziemann, C. Sapper, and W. Eischer, “22 dBm receiver sensitivity for Gbit/s data communication on SI-POF and glass fiber,” in *14th International Conference on Plastic Optical Fibers*, pp. 255–259, 2005.
- [Vinogradov08] J. Vinogradov, O. Ziemann, O. Lednicky, J. Gottschalk, M. Zceh, and S. Tchoupkoua, “Optimal equalizers for SI-POF and Gpbs,” in *17th International Conference on Plastic Optical Fibers*, 2008.
- [Vinogradov11] J. Vinogradov, R. Kruglov, S. Loquai, and O. Ziemann, “Multi gigabit transmission with blue, green and red laser diodes,” in *20th International Conference on Plastic Optical Fibers*, pp. 467–470, 2011.
- [Voigt14] Y. Voigt, “Digital pre- and post-equalizers for in-car transmission over plastic optical fibers,” Ph.D. dissertation, Fakultät für Informatik, Elektrotechnik und Informationstechnik, Universität Stuttgart, Germany, 2014.
- [Werzinger13] S. Werzinger, C.-A. Bunge, S. Loquai, and O. Ziemann, “An analytical connector loss model for step-index polymer optical fiber links,” *IEEE Journal of Lightwave Technology*, vol. 31, no. 16, pp. 2769-2776, Aug. 2013.
- [Zeola11] D. Zeolla, A. Antonino, G. Bosco, and R. Gaudino, “DFE versus MLSE electronic equalization for Gigabit/s SI-POF transmission systems,” *IEEE Photonics Technology Letters*, vol. 23, no. 8, pp. 510-512, Apr. 2011.
- [Zhang05] Y. Zhang, H. Ma, T. Zhang, Z. Wang, D. Wang, R. Zheng, H. Yang, and H. Ming, “Study on coarse wavelength division multiplexing using polymer optical fiber transmission window,” in *SPIE 5644, Optoelectronic Devices and Integration*, 2005.
- [Zhou12] X. Zhou and L.E. Nelson, “400G WDM transmission on the 50 GHz grid for future optical networks,” *IEEE Journal of Lightwave Technology*, vol. 30, no. 24, pp. 3779-3792, Dec. 2012.
- [Ziemann08] O. Ziemann, J. Krauser, P. E. Zamzow, and W. Daum, *POF Handbook – Optical Short Range Transmission Systems*. 2nd ed., Springer Verlag Berlin Heidelberg, 2008.



[Ziemann11] O. Ziemann, and L. Bartkiv, “POF-WDM, the truth,” in *20th International Conference on Plastic Optical Fibers*, pp. 525-530, 2013.

[Zubia01] J. Zubia and J. Arrue, “Plastic optical fibers: An introduction to their technological processes and applications,” *Optical Fiber Technology*, vol. 7, no. 2, pp. 101-140, Apr. 2001.



List of abbreviations

ADSL	Asymmetric digital subscriber line
AOI	Angle of incidence
AWG	Arbitrary waveform generator
BER	Bit error rate
BERT	Bit error rate tester
BMBF	German Federal Ministry of Education and Research
BW	3 dB passband bandwidth
CD	Compact disc
CD-ROM	Compact disc read-only memory
CDR	Clock and data recovery
CP	Cyclic prefix
CWDM	Coarse wavelength division multiplexing
DC	Direct current
DEMUX	Demultiplexer
DFFE	Decision-feedback equalization
DMT	Discrete multitone
DPMA	German Patent and Trade Mark Office
DSL	Digital subscriber line
DUT	Demultiplexer under test
DVB – S/T	Terrestrial/satellite digital video broadcast
DVD	Digital video disc
DWDM	Dense wavelength division multiplexing
ETSI	European Telecommunications Standards Institute
FEC	Forward error correction
FFE	Feed-forward equalization
FFT	Fast Fourier transform
FT	Flat top
FTTB	Fiber-to-the-building
GI	Graded-index
GI-POF	Graded-index polymer optical fiber
GPS	Global positioning system
HFC	Hybrid fiber-coax
HTTP	Hypertext transfer protocol
ICPOF	International Conference on Plastic Optical Fibers



IEC	International Electrotechnical Commission
IFFT	Inverse fast Fourier transform
IHF	Institut für Hochfrequenztechnik der Technischen Universität Braunschweig
IL	Insertion loss
IM/DD	Intensity modulation and direct detection
ISI	Inter-symbol interference
ITG	Information Technology Society of Germany
ITU	International Telecommunication Union
ITU-T	Telecommunication Standardization Sector of the ITU
LD	Laser diode
LED	Light-emitting diode
MOST	Media oriented system transport
MUX	Multiplexer
NA	Numerical aperture
NRZ	Non-return-to-zero
OFDM	Orthogonal frequency division multiplexing
OSA	Optical spectrum analyzer
PAM	Pulse amplitude modulation
PD	Photodiode
PF POF	Perfluorinated polymer optical fiber
PIN	Positive-intrinsic-negative (diode)
PMMA	Polymethyl methacrylate
POF	Polymer optical fiber
POF-AC	Polymer Optical Fiber Application Center
PRBS	Pseudo-random binary sequence
QAM	Quadrature amplitude modulation
SI	Step-index
SI-POF	Step-index polymer optical fiber
SNR	Signal-to-noise ratio
TEC	Temperature control
TIA	Transimpedance amplifier
TS	Transition slope
TV	Television
UV	Ultraviolet
VCSEL	Vertical cavity surface emitting laser
VDSL	Very high-speed digital subscriber line
VoD	Video on demand
VoIP	Voice over internet protocol
WDM	Wavelength division multiplexing
WLAN	Wireless local area network

List of publications

Journals

1. M. Jončić, R. Kruglov, M. Haupt, R. Caspary, J. Vinogradov, and U. H. P. Fischer-Hirchert, “Four-channel WDM transmission over 50-m SI-POF at 14.77 Gb/s using DMT modulation,” *IEEE Photonics Technology Letters*, vol. 26, no. 13, pp. 1328-1331, July 2014.

International conferences

2. M. Jončić, M. Haupt, R. Caspary, U. H. P. Fischer-Hirchert, and W. Kowalsky, “Characterization of transmission properties of a mechanically ruled concave grating-based POF demultiplexer for future injection molding,” in *24th International Conference on Plastic Optical Fibers*, Nürnberg (Germany), Sept. 2015.
3. R. Caspary, M. Jončić, M. Haupt, U. H. P. Fischer-Hirchert, R. Kruglov, J. Vinogradov, H.-H. Johannes, and W. Kowalsky, “High speed WDM transmission on standard polymer optical fibers,” in *17th International Conference on Transparent Optical Networks (ICTON 2015)*, Budapest (Hungary), July 2015.
4. U. H. P. Fischer-Hirchert, S. Höll, M. Haupt, and M. Jončić, “Polymeric demultiplexer component for wavelength division multiplex communication systems using polymer fibers,” in *SPIE 9368, Optical Interconnects XV*, 93680Q, San Francisco, CA (USA), Apr. 2015.
5. M. Jončić, R. Kruglov, M. Haupt, R. Caspary, J. Vinogradov, U. H. P. Fischer, and O. Ziemann, “Four-channel WDM transmission via 1-mm SI-POF employing DMT modulation,” in *23rd International Conference on Plastic Optical Fibers*, Yokohama (Japan), Oct. 2014.
6. M. Jončić, M. Haupt, and U. H. P. Fischer-Hirchert, “Investigation on coarse WDM components and systems for four-channel Multi-Gb/s short-range transmission over 1-mm diameter step-index polymer optical fiber,” in *World Telecommunications Congress 2014*, Berlin (Germany), June 2014.
7. M. Jončić, M. Haupt, and U. H. P. Fischer-Hirchert, “Coarse WDM: A way to increase the transmission capacity of a 1-mm diameter step index polymer optical fiber,” in *15. ITG-Fachtagung Photonische Netze*, Leipzig (Germany), May 2014.



8. M. Jončić, M. Haupt, and U. H. P. Fischer-Hirchert, “Four-channel CWDM system design for multi-Gbit/s data communication via SI-POF,” in *SPIE 9007, Broadband Access Communication Technologies VIII*, 90070J, San Francisco, CA (USA), Dec. 2013.
9. M. Jončić, M. Haupt, and U. H. P. Fischer-Hirchert, “Development status of a four-channel CWDM system for Multi-Gbit/s in-house data communication via SI-POF,” in *20. ITG-Fachtagung Kommunikationskabelnetze*, Köln (Germany), Dec. 2013.
10. M. Jončić, S. Höll, M. Haupt, R. Caspary, and U. H. P. Fischer-Hirchert, “Development status of a four-channel CWDM system for Multi-Gbit/s data links over SI-POF,” in *22nd International Conference on Plastic Optical Fibers*, pp. 59-64, Buzios, RJ (Brazil) Sept. 2013.
11. M. Jončić, M. Haupt, R. Caspary, and U. H. P. Fischer-Hirchert, “Development of a four-channel CWDM transmission system for Multi-Gbit/s VIS-WDM applications over SI-POF,” in *2013 International Students and Young Scientists Workshop “Photonics and Microsystems”*, Dresden (Germany), July 2013.
12. M. Jončić, M. Haupt, and U. H. P. Fischer-Hirchert, “Investigation on spectral grids for VIS WDM applications over SI-POF,” in *14. ITG-Fachtagung Photonische Netze*, Leipzig (Germany), May 2013.
13. M. Jončić, M. Haupt, and U. H. P. Fischer-Hirchert, “Standardization proposal for spectral grid for VIS WDM applications over SI-POF,” in *21st International Conference on Plastic Optical Fibers*, pp. 351-355, Atlanta, GA (USA), Sept. 2012.
14. R. Caspary, M. Jončić, M. Haupt, and U. H. P. Fischer-Hirchert, “Characterization of laser modules for four-channel high-speed WDM systems over POFs,” in *21st International Conference on Plastic Optical Fibers*, pp. 242-247, Atlanta, GA (USA), Sept. 2012.
15. M. Jončić, M. Haupt, and U. H. P. Fischer-Hirchert, “WDM over POF – Spectral grids for VIS WDM applications over SI-POF,” in *2012 International Students and Young Scientists Workshop “Photonics and Microsystems”*, Szklarska Poreba (Poland), July 2012.
16. M. Jončić, M. Haupt, and U. H. P. Fischer-Hirchert, “WDM over SI-POF – a general concept,” in *13. Nachwuchswissenschaftlerkonferenz*, pp. 369-372, Görlitz (Germany), Apr. 2012.
17. M. Jončić, M. Haupt, and U. H. P. Fischer-Hirchert, “Spectral grids for VIS WDM applications over SI-POF,” in *20th International Conference on Plastic Optical Fibers*, pp. 63-68, Bilbao (Spain), Sept. 2011.



Book chapters

18. U. H. P. Fischer-Hirchert, M. Haupt, and M. Jončić, “Optical transmission systems using polymeric fibers,” in *Optoelectronics – Devices and Applications*, P. Predeep, Ed., 2011, ch. 22.





